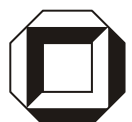


Dissertationsreihe am Institut für Hydromechanik
der Universität Karlsruhe (TH)
Heft 2004/1

Influence of Dead-Water Zones on
the Dispersive Mass Transport
in Rivers

Volker Weitbrecht



Impressum

Universitätsverlag Karlsruhe
c/o Universitätsbibliothek
Straße am Forum 2
D-76131 Karlsruhe

www.uvka.de

© Universitätsverlag Karlsruhe 2004
Print on Demand
Druck: Digital Print Group Erlangen

ISSN 1439-4111
ISBN 3-937300-07-4

Influence of Dead-Water Zones on the Dispersive Mass Transport in Rivers

Zur Erlangung des akademischen Grades eines
DOKTOR-INGENIEURS
von der Fakultät für Bauingenieur-, Geo- und Umweltwissenschaften
der Universität Fridericiana zu Karlsruhe (TH)

genehmigte
DISSERTATION

von
Dipl.-Ing. Volker Weitbrecht
aus Stuttgart

Tag der mündlichen Prüfung: 6. Februar 2004

Hauptreferent: Prof. Gerhard H. Jirka, Ph.D.
Korreferent: Prof. Dr.-Ing. Bernhard Westrich

Karlsruhe 2004

Erklärung

Hiermit versichere ich, die vorliegende Arbeit selbständig verfasst und keine weiteren als die angegebenen Hilfsmittel und Quellen benutzt zu haben.

Karlsruhe, den 16. November 2003

Volker Weitbrecht

Influence of Dead-Water Zones on the Dispersive Mass Transport in Rivers

Abstract

The dispersive mass transport in rivers has been investigated to improve the predictability of transport scenarios in case of accidental pollutant spills. In particular, the influence of dead-water zones, as they are given by groin fields, on the transport characteristics in the main stream has been analyzed.

A literature review of detailed map material from the rivers Rhine, Waal and Elbe has been performed, in order to plan representative laboratory experiments. Typical aspect ratios of the groin fields as well as typical inclination angles have been summarized. Based on these results, experiments have been performed in a laboratory flume equipped with schematized groins. Within these experiments the aspect ratio, the inclination angles as well as the groin field volume has been varied.

Due to the fact that the flow is very shallow and, therefore, quasi two-dimensional, the flow velocities have been determined at the water surface, using a Surface Particle-Image-Velocimetry-System that has been developed for that purpose. Additional measurements, using a two-dimensional Laser-Doppler-Velocimeter, have been performed for resolving the velocity distribution over the water depth. With the help of these measurements it was possible to determine the typical recirculating flows in the groin fields as well as the coherent, horizontal eddies in the mixing layer between dead-water zone and main stream, that are governing the mass exchange. The high spatial and temporal resolution of the surface PIV measurements made it possible to estimate also the mass exchange between groin field and main stream.

With the help of Planar-Concentration-Analysis, which is a method for determining depth-averaged planar concentration fields, it could be shown that the mass exchange between groin field and main stream increases with increasing length of the groin field. For these measurements a tracer injection device has been developed, that consists of a movable multi-port injection-box and vacuum-pressure-unit, which is able to produce instantaneously, homogeneous and reproducible concentration fields.

Finally a Lagrangian-Particle-Tracking-Method was developed to transfer the results, obtained locally at single groin fields, into the overall transport characteristics in the far-field of pollutant spill scenario for a river system consisting of a series of groin fields. Through the implementation of a transient-adhesion-boundary, it was possible to parameterize the influence of groin fields on the longitudinal dispersion, the transport velocity and the skewness of the concentration distribution in the case of a pollutant spill.

Einfluß von Totwasserzonen auf den dispersiven Massentransport in Flüssen

Kurzfassung

In der vorliegenden Arbeit wurde der dispersive Massentransport in Flüssen untersucht, um die Vorhersage des Stofftransportes bei Schadstoffunfällen zu verbessern. Dabei wurden speziell die Einflüsse von Totwasserzonen, wie sie im Fall von Bühnenfeldern gegeben sind, auf die Transportcharakteristik im Hauptstrom analysiert.

Zur Vorbereitung der Laborversuche wurden ausführliche Untersuchungen von Kartenmaterial an Rhein, Waal und Elbe durchgeführt. Typische Breiten-Längenverhältnisse, sowie typische Neigungswinkel der Bühnen gegen die Strömungsrichtung wurden dabei zusammengestellt. Aufbauend auf diese Ergebnisse wurden Versuche in einer mit schematisierten Bühnen ausgestatteten Laborrinne durchgeführt, bei denen das Längen-Breitenverhältnis des Bühnenfelds, der Neigungswinkel der Bühnen sowie das Bühnenfeldvolumen variiert wurde.

Auf Grund der ausgeprägten Zweidimensionalität der Strömung wurden die Fließgeschwindigkeiten an der Wasseroberfläche in den Bühnenfeldern sowie in der Hauptströmung mit einem speziell dafür entwickelten Oberflächen Particle-Image-Velocimetry System untersucht. Zusätzliche Messungen mit einem Zwei-Komponenten Laser-Doppler-Anemometer wurden durchgeführt, um Geschwindigkeitsverteilungen über die Wassertiefe zu untersuchen. Mit Hilfe dieser Messungen konnten die typischen Rezirkulationssysteme in den Bühnenfeldern sowie die für den Massenaustausch wichtigen kohärenten horizontalen Wirbelstrukturen in der Mischschicht analysiert werden. Die hohe räumliche und zeitliche Auflösung des 'Oberflächen PIV Systems' erlaubte es Rückschlüsse auf den Massenaustausch zwischen Bühnenfeld und Hauptstrom zu ziehen.

Mit Hilfe von „Planar-Concentration-Analysis“, einer Methode zur Bestimmung von planaren tiefengemittelten Konzentrationsfeldern, konnte gezeigt werden, dass der Massenaustausch zwischen Bühnenfeld und Hauptstrom mit zunehmender Länge des Bühnenfeldes zunimmt. Ein für diesen Zweck entwickeltes Tracerzugabesystem, bestehend aus einem beweglichen Injektionstank und einer Druck/Vakuum-Tankeinheit zur Erzeugung instantaner, homogener Konzentrationsfelder, garantierte dabei reproduzierbare Ergebnisse.

Die Übertragung der lokalen Ergebnisse an einzelnen Bühnenfeldern auf den Stofftransport im Fernfeld eines Transportszenarios wurde mit Hilfe einer Lagrangian-Particle-Tracking-Methode durchgeführt. Durch die Einführung einer zeitabhängigen Haftbedingung als Randbedingung konnte der Einfluss von Bühnenfeldern auf Dispersion, Transportgeschwindigkeit und Schiefe der Konzentrationsverteilung einer Schadstoffwolke simuliert werden.

Vorwort

Die vorliegende Arbeit entstand während meiner Tätigkeit als wissenschaftlicher Angestellter am Institut für Hydromechanik der Universität Karlsruhe.

Bedanken möchte ich mich besonders bei Herrn Prof. G.H. Jirka für die stetige, fachkundige und wissenschaftliche Betreuung. Sein Vertrauen und die damit verbundenen vielfältigen Möglichkeiten waren für das Entstehen dieser Arbeit sehr förderlich. Herrn Prof. B. Westrich danke ich für die Übernahme des Korreferats.

Bei Herrn Dr. A. Richter und Frau Dr. C. Lang möchte ich mich für die wertvollen Hinweise zur Umsetzung der experimentellen Arbeiten, sowie für die Bewältigung der verwaltungstechnischen Aufgaben des Forschungsprojekts bedanken.

Dank gilt allen Kollegen und Mitarbeitern des Instituts für Hydromechanik für die stets gute und konstruktive Zusammenarbeit. Stellvertretend für alle gilt mein Dank besonders Herrn G. Kühn für die Unterstützung des Projektes vor allem bei der Entwicklung des Oberflächen PIV Systems sowie der Tracerzugabeeinheit.

Für wertvolle fachliche Diskussionen außerhalb der Institutsgrenzen möchte ich mich vor allem bei Frau Dr. N. von Götz, Herrn Dr. K. Nübel, Herrn Prof. S. Socolofsky, Herrn dr.ir. A. van Mazijk und Herrn dr.ir. W. Uijttewaal bedanken.

Außerdem möchte ich mich bei sämtlichen studentischen Hilfskräften bedanken, die an diesem Forschungsprojekt mitgearbeitet haben. Besonders möchte ich dabei Frau M. Kurzke erwähnen, die mir eine große Hilfe bei der Auswertung der Konzentrationsmessungen war.

Finanziell gefördert, und damit erst möglich gemacht, wurde das Projekt durch das Bundesministerium für Bildung und Forschung (Projektnummer 02 WT 9934/9).

Karlsruhe, März 2004

Contents

1. Introduction	1
1.1 Background	2
1.2 Outline	5
2. Characterization of Dead-Water Zones in Rivers	8
2.1 General characteristics of groins	9
2.2 Typical groin field geometries	11
2.3 Qualitative description of flow patterns in groin fields	16
2.4 Qualitative description of transport processes due to groin fields	19
3. Transport Processes: Theoretical Background	21
3.1 Basic processes	21
3.1.1 Diffusion	22
3.1.2 Advection-diffusion	24
3.2 Longitudinal dispersion	26
3.2.1 Taylor's approach	27
3.2.2 Application of Taylor's approach	31
3.3 Mass transport in rivers	33
3.3.1 The advective zone	33
3.3.2 Dispersion coefficients in rivers	35
3.4 Alternatives to the advection diffusion equation	36
3.4.1 Dead-zone-model	37
3.4.2 Lagrangian-Particle-Tracking-Method	42
4. Experimental Studies	44
4.1 Laboratory facilities	44
4.2 Measurement techniques: velocity	45
4.2.1 Surface Particle-Image-Velocimetry (PIV)	46
4.2.2 Elements of the PIV system	47
4.2.3 Accuracy of the PIV system	52
4.2.4 PIV measuring and -evaluation settings	56
4.2.5 Laser-Doppler-Velocimetry (LDV)	57
4.3 Measurement technique: Planar-Concentration-Analysis (PCA)	60
4.3.1 Elements of the PCA system	60
4.3.2 Calibration and evaluation of concentration fields	63

4.4	Experimental program	66
5.	Experimental Results	72
5.1	Measured flow velocities	72
5.1.1	Reference case ($W/L = 0.4$, $\alpha = 90^\circ$)	72
5.1.2	Influence of the groin field aspect ratio W/L	80
5.1.3	Influence of the inclination angle	83
5.1.4	Submerged groins	85
5.1.5	Influence of groin length	86
5.1.6	Influence of groin field volume	87
5.1.7	Exchange rates determined with surface PIV	89
5.2	Measured concentration fields and exchange values	92
5.3	Analysis of exchange coefficients	94
5.3.1	Comparison between k_{PIV} and k_{PCA}	94
5.3.2	Influence of the geometry on the exchange coefficient	95
5.3.3	Normalization of the exchange coefficient k	97
6.	Lagrangian-Particle-Tracking	101
6.1	Introduction	101
6.2	Method	102
6.3	Verification of the model formulation	106
6.3.1	Qualitative comparison of the particle behavior	106
6.3.2	Quantitative verification	107
6.4	Application	113
6.4.1	Open channel flow without groin fields	114
6.4.2	Channel flow with groin fields	116
6.4.3	Influence of groin fields of different exchange behavior	119
6.4.4	Combined effect of dead-water zones and channel width	121
6.5	Summary	122
7.	Conclusions and Recommendations	124
	References	127

List of Figures

1.1	Schematic sketch of an accidental spill with the corresponding concentration curve far downstream of the accidental inflow	1
2.1	Sketch of idealized dead-water zones at the bottom of a flow field adapted from Valentine & Wood (1979)	8
2.2	Schematic sketch to define the terminology used in the present study	9
2.3	Top view and cross-sectional view of a groin from the river Elbe, taken from Neger (1932)	9
2.4	Aerial photograph of groin fields in the River Rhine close to Emmerich showing the density of the shipping traffic	10
2.5	Schematic sketch of a prototype groin combining the positive effects of different inclination angles	11
2.6	Simplified classification of sedimentation patterns in groin fields taken from (Sukhodolov, Uijtewaal & Engelhardt 2002)	12
2.7	Areal photograph of the River Elbe taken at km 490, with low discharge conditions, where the different groin classes, defined in figure 2.6, are denoted; authorized by Wasser- und Schifffahrtsdirektion Ost, Berlin	13
2.8	Probability distribution of the occurrence of groin field geometries in the River Elbe (Hinkel 1999)	13
2.9	Groin fields in the River Rhine at km 302-304	14
2.10	Probability of occurring W/L aspect ratios within the River Rhine km 288-376	15
2.11	Probability of occurring W/L aspect ratios within the River Waal km 857-859	15
2.12	Groin fields in the River Waal at km 881-882	15
2.13	Velocity measurements using intermittent photography of floating candles, exposure time = 1s, with a main flow direction from left to right, taken from Rehbock (1926)	16
2.14	Influence of the aspect ratio W/L on the gyre configuration in a dead-water zone taken from Lehmann (1999)	17
2.15	Schematic sketch of the flow patterns in groin fields for very small aspect ratio W/L	18
2.16	Schematic sketch of groin fields with different inclination angles and their influence on the development of the two gyre system	18
2.17	Characterization of the flow in the mixing layer; i) Mean velocity profile across a groin field and the mixing layer, ii) Schematic sketch of large coherent motions that emerge at the groin heads and grow during their travel downstream	19
3.1	Characteristic regions of different diffusivity and the expected distribution of the diffusivity in transverse direction	23
3.2	Control volume illustrating the mass flux J due to advection u in x-direction	25
3.3	Transport of a tracer cloud in a homogeneous flow field $q = (u, 0, 0)$ due to advection and diffusion, where the tracer cloud is visualized at three different time steps	26
3.4	Top view on a river to visualize the stretching of a tracer cloud due to dispersion; i) initial homogeneous tracer injection; ii) tracer cloud gets deformed corresponding to the velocity distribution; iii) turbulent diffusion leads to a homogenization of the tracer cloud in transverse direction of the river	27
3.5	Schematic sketch of the Reynolds-Decomposition in vertical shear flow	28
3.6	Laminar velocity distribution	31
3.7	Visualization of the three different stages of mixing in a natural river and definition of the advective length L_x ; A) active mixing due to momentum and buoyancy forces in the near-field, B) turbulent diffusion in transverse direction in the mid-field, C) tracer is distributed over the river cross-section in the far-field; adapted from Fischer, List, Koh, Imberger & Brooks (1979)	34
3.8	Schematic sketch of a typical longitudinal concentration profile compared to the Gaussian concentration profile according to Taylor's 1-dimensional solution	37
3.9	Schematic top view on a river where the two regions main channel and dead-zone are illustrated. In order to derive the associated equations by performing a mass balance, the corresponding mass fluxes in the 1-dimensional case are shown	38
3.10	Schematic side view of a river where the two regions: main channel and dead-zone are illustrated	39

3.11	a) visualization of the initial conditions in the case of a instantaneous volume source in the dead-zone leading to the unit impulse response showed in b) with the exponential concentration decay in the dead-water zone due to exchange processes	40
3.12	a) evolution of the skewness in dependence of the distance from the source; b) skewness in dependence of the ratio between cross-sectional area of the dead-zone and the main stream expressed by β ; exponential concentration decrease in the dead-water zone due to exchange processes; taken from Schmid (1995) . .	41
4.1	Schematic top view of the laboratory flume	45
4.2	Correlation plane with correlation peak	47
4.3	Schematic sketch of the different components of a typical PIV system	48
4.4	Schematic top and side view of the particle dispenser	50
4.5	Raw pictures of the measurement field where the Polypropylene particles on the water surface are visible.	51
4.6	Artificial particle clouds with different particle size and density	52
4.7	Digital image of a particle in a cell of 6 x 6 pixels	53
4.8	Evaluation of the position of the center of mass of a particle; i) particle is larger than 1.5 pixels, leading to a position accuracy in the order of sub-pixel units; ii) Particle is smaller than one pixel, leading to an accuracy in the order of one pixel.	53
4.9	Illustration of peak locking effects, associated with insufficient particle image size, by showing a histogram of PIV displacements	54
4.10	Rotation of interrogation areas in order to analyze the influence of velocity shear on the PIV results . .	54
4.11	Rotation of interrogation areas in order to analyze the influence of velocity shear on the PIV results . .	55
4.12	Rotating disk tests: i) Measurements of the velocity distribution; ii) Deviation from calculated velocity	56
4.13	Result of surface PIV measurements where the instantaneous flow is visualized at two different time steps with a Δt of 2 seconds. Example with $W/L = 0.33$	57
4.14	Schematic visualization of the vector processing procedurs.	58
4.15	Schematic sketch of the different components of the 2-dimensional LDV-system taken from (TSI 1996)	59
4.16	Schematic sketch of the laser beams that cross the water surface: i) in the case of horizontal water surface ; ii) in the presence of surface waves with a moving measurements -volume; iii) surface waves suppressed by a quartz-glass-plate on the water surface	60
4.17	Schematic sketch of the movable Multi-Port-Injection-Device (MPID)	61
4.18	Photo of the control panel i) and the movable Multi-Port-Injection-Device ii)	61
4.19	Top view on the measurement area showing the concentration field; i) 6.5 seconds after the start of the injection; ii) 16.5 seconds after the start of the injection	62
4.20	Schematic representation of intensity-dependent concentrations	63
4.21	Measured intensity-concentration dependence, and fitted curve from equation 4.4.	64
4.22	Calibration procedure with four different concentrations in the inner frame. i) 0 mg/l; ii) 1.0 mg/l; iii) 4.2 mg/l; iv) 10.6 mg/l	65
4.23	PCA, i) gray-scale picture with the measurement area and the reference frame to take into account changing illumination conditions during the experiment; ii) gray-scale picture with the final size of the concentration matrix (app. 100 elements)	66
4.24	Schematic top view of the different aspect ratios and the different inclination angles; the indicated numbers correspond to the different cases described in table 4.2	70
4.25	Schematic side view of the different experimental setups; the indicated numbers correspond to the different cases described in table 4.2	71
5.1	Mean flow characteristics; i) Streamline plot of the reference case; ii) Velocity profile of the u-component averaged over the length L of the groin field normalized with the maximum velocity at the water surface U_s . In addition, an approximation of the velocity profile with a hyperbolic tangent function is plotted. The horizontal dividing line indicates the position of the groin heads.	73
5.2	Normalized velocity profiles of the u-component at $x = 0.25L$, $0.5L$ and $0.75L$ (figure 5.1, i).	73
5.3	Comparison of the flow profile in the case of groin fields and in the case of a regular wall flow where the wall consists of glass. In the case of groin field flow $y/h = 0$ indicates the groin head, in the case without groins $y/h = 0$ indicates the channel wall.	74
5.4	i) Intensity of the velocity fluctuations in x-direction (light colors indicate higher intensities), \times indicates the position s of vertical velocity profiles as given in figure 5.7 and 5.8; ii) RMS-velocity profiles P1, P2 and P3 at $x = 0.25L$, $0.5L$ and $0.75L$, normalized with the mean shear velocity u_* in the main stream. In addition the result of the LDV measurement taken at $x = 0.5L$ is plotted.	75
5.5	i) Intensity of the velocity fluctuations in y-direction (light colors indicate higher intensities); ii) RMS-velocity profiles P1, P2 and P3 at $x = 0.25L$, $0.5L$ and $0.75L$, normalized with the mean shear velocity u_* in the main stream. In addition the result of the LDV measurement taken at $x = 0.5L$ is plotted. . .	75

VI List of Figures

5.6	Turbulence intensity, measured with PIV in undisturbed channel flow compared with the LDV measurements and a Gaussian fit for v'/u_* . For the PIV measurements $y/h = 0$ indicates the position of the groin field head in the case of the LDV measurements, in the case of the PIV measurements, $y/h = 0$ indicates the channel wall. The box region indicates the undisturbed flow in the main channel where both measurements are comparable with the reference values taken from Nezu & Nakagawa (1993) given in table 5.1.	76
5.7	Vertical velocity profiles of the u-component in the main channel and in the mixing layer, normalized with the mean velocity in the main channel $U = Q/A_S$. The position of the measurements are indicated in figure 5.4.	77
5.8	Vertical velocity profiles of the v-component in the main channel and in the mixing layer, normalized with the mean velocity in the main channel $U = Q/A_S$. The position of the measurements are indicated in figure 5.4.	78
5.9	Time averaged velocities in transverse direction along the connection line between two groin heads. ...	79
5.10	Visualization of the coherent flow structures that emerge at the groin head and grow during their travel through the mixing layer. Δt between two pictures is 1s.	79
5.11	Visualization of the coherent flow structures with the help of the vorticity and the instantaneous velocity deviation from the mean velocity. Δt between two pictures is 1s. Light color indicates clockwise rotation and dark color anticlockwise rotation.	80
5.12	Schematic sketch of the series No. 1-8 from table 4.2 with changing W/L aspect ratio.	81
5.13	Mean flow properties in groin field flows with different W/L aspect ratios, where the three different possibilities of 1- and 2- gyre systems are visible.	81
5.14	Comparison of the mean velocity profiles for the different W/L aspect ratios corresponding to the cases No. 1-8 from table 4.2. Hereby the velocities are averaged in space over the length L of the groin fields, and normalized with the maximum velocity at the water surface U_s	82
5.15	Comparison of the normalized RMS-velocities v' for the different W/L aspect ratios corresponding to the cases No. 1-8 (table 4.2).	83
5.16	Schematic sketch of the series No. 10-13 with forward and backward inclined groins (table 4.2).	84
5.17	Mean flow properties in groin field flows with different inclination angle α ; i) backward inclined groins with $\alpha = 64^\circ$; ii) forward inclined groins where α is 116°	84
5.18	Transverse turbulent intensity v'/u_* , where dark regions indicate low values and bright regions indicate the maximum values. In the left figure (i) the maximum value is 1.7 and in the right figure (ii) it is 1.5.	85
5.19	Mean flow properties at the water surface in case of submerged groins, series No. 9, where the water depth in the main stream is 18% larger than the height of the groins.	86
5.20	i),ii) and iii), show the mean flow pattern at the water surface in case of short groins, series No. 14-16; iv),v) and vi) show the turbulence intensity v'/u_*	87
5.21	Instantaneous velocity fields in the case of short groins with an aspect ratio $W/L = 0.17$. Time interval between two velocity fields is 2 seconds.	88
5.22	Schematic side view in streamwise direction of the experiments No. 17 and 18 where the dead-zone volume is reduced by 50% compared to the reference case.	88
5.23	Mean flow pattern in the case of reduced groin field volume; i) Series No. 17 with sloping depth in the groin field, such that the water depth at the interface between dead-zone and main channel is the same in the main channel and zero at the channel wall; ii) Series No. 18, where the water depth in the groin field is only half the water depth in the main channel.	89
5.24	Top view on the groin field of experiment No. 17 and 18, showing the Reynolds Number based on the local surface flow velocity and the local water depth; i) Series No. 17 with sloping depth in the groin field; ii) Series No. 18, where the water depth in the groin field is only half the water depth in the main channel.	89
5.25	Cross-sectional of a river with dead-zone and a top view on a groin field with a schematic visualization of the instantaneous velocities at the groin field boundary.	91
5.26	Dimensionless exchange coefficient k_{PIV} against the aspect ratio W/L	91
5.27	Measured concentration averaged over the total volume of the groin field and fitted exponential decay function; i) Experiment No. 1 with an aspect ratio $W/L = 0.35$, with a mean residence time T_D of 100 s; ii) Experiment No. 6 with an aspect ratio $W/L = 1.11$, with a mean residence time T_D of 140 s.	92
5.28	Dimensionless exchange coefficient k_{PCA} against the aspect ratio W/L	94
5.29	Comparison of the k-values determined with surface PIV (filled symbols, \bullet) and the PCA technique (open symbols, \circ); i) Regular cases No. 1-8; ii) Groins that are inclined with and against the flow, No. 10-13; iii) Short groins, No. 14-16; iv) Reduced groin field volume, No. 17,18.	95
5.30	Definition of the effective length of the groin field.	98
5.31	Exchange coefficients k averaged from PCA and PIV measurements, in relation to the parameter developed in equation 5.13.	98
5.32	Visualization of i) very elongated ($L \gg W$) and ii) very narrow groin fields ($W \gg L$).	99

5.33	Exchange coefficients k averaged from PCA and PIV measurements, in relation to the hydraulic radius R_D/h_S (equation 5.16) of the dead-zone.	100
6.1	Particle velocity in a 2-dimensional flow field with mean velocity in x-direction and turbulent velocities in y-direction	102
6.2	Schematic visualization of a particle approach to a reflective boundary within one time step	104
6.3	Schematic visualization of a particle approach to a transient adhesion boundary at: i) time = t_i and ii) time = $it_i + T_D$, where T_D is the mean residence time.	105
6.4	LPTM simulation for parabolic velocity profile with constant transverse diffusivity; i) 8000 particles after 5, 40 and 100 time steps, under the influence of a parabolic velocity distribution and constant diffusion in transverse direction. Initially the particles are distributed homogeneously over the channel width; ii) Distribution of the particles in longitudinal direction; iii) Time series of the longitudinal dispersion coefficient and skewness evaluated at each time step.	107
6.5	LPTM simulation for Case 1 with linear velocity shear and constant transverse diffusion coefficient, showing the particle position and the particle distribution in longitudinal direction.	109
6.6	Evolution of the dispersion coefficient in the case of laminar flow between plates (Couette problem) for the Cases 1-3 from table 6.1.	110
6.7	Lagrangian particle tracking simulation of the Elder's case with unbounded shear flow and a parabolic distribution of the diffusivity over the water depth; i) showing the particle positions at a certain time step; ii) showing the particle density cross-sectionally averaged in longitudinal direction.	112
6.8	Visualization of the influence of the noise drift component in the Elder's case; i) LPTM simulation where the noise drift correction is neglected, leading to high particle concentrations close the water surface and the channel bottom; ii) LPTM simulation including the noise drift correction, leading to a homogeneous particle distribution.	113
6.9	Evolution of the longitudinal dispersion coefficient D_L and the skewness G_t during the LPTM simulation. D_L is smoothed with a sliding average filter of increasing window size.	114
6.10	Lagrangian particle tracking simulation of pure open channel flow with constant diffusivity over the channel width; i) showing the particle positions at a certain time step; ii) showing the particle density cross-sectionally averaged in longitudinal direction.	115
6.11	Evolution of the longitudinal dispersion coefficient $D_L/(u_*h)10^{-2}$ and the skewness G_t during the LPTM simulation.	115
6.12	Lagrangian particle tracking simulation of the channel flow under the influence of groin fields; i) showing the particle positions at a certain time step; ii) showing the particle density cross-sectionally averaged in longitudinal direction.	117
6.13	Evolution of Dispersion coefficient $D_L 10^{-4}$ normalized with u_* and the water depth h and the evolution of the skewness. D_L is smoothed with a sliding average filter of increasing window size. ($W/B = 0.5$)	118
6.14	Evolution of transport velocity c of a tracer cloud normalized with mean velocity of the main channel.	119
6.15	Particle density distribution in river cross-section as a function of the distance x/B	119
6.16	Normalized transport velocity c/U as a function of the shape factor R_D/h_S	120
6.17	Influence on channel width on the longitudinal Dispersion coefficient, in comparison with a real river situation.	122

List of Tables

3.1	Theoretical length of the advective zone, before well mixed conditions are established. D_y is determined by equation 3.5 and u_* is estimated to be to be 10% of the mean velocity; $L_{x,S}$ represents the case where the mass has been released in the center of the river and in the case of $L_{x,B}$ the mass has been released at the river bank; $L_{x,D}$ represents the case presented by Valentine & Wood (1979) including the effect of dead-zones	34
4.1	Properties of the different tracer material and their applicability to water surface measurementst	50
4.2	Experimental settings, describing the positions, width and length and inclination angles of the groins fields.	69
5.1	Comparison of measured turbulence intensities in the undisturbed channel flow with reference values taken from Nezu & Nakagawa (1993)	77
5.2	Measured exchange values k using the direct PCA method by analyzing the concentration fields. Series 1-3 are the three different time experiments that have been measured for every geometrical condition and the mean value represents the average of run 1-3.	93
6.1	Parameter values of a sensitivity study for a LPTM simulation for laminar Couette shear flow	108
6.2	Parameter values for the Elder simulation	112
6.3	Parameter values for the pure channel flow simulation, taken from the measurements	114
6.4	Results of LPTM simulations compared with the evaluation of Fischer's triple integral given in equation 3.57.	117
6.5	Results of LPTM simulations with different exchange coefficients corresponding to varying R_D/h from figure 5.33 corresponding to a channel width $B/h = 43$, compared with the case of pure channel flow ($k = \infty$).	120
6.6	Flow situation, similar to the flow in the river Rhine close to Karlsruhe at km 390 with groins only on one side of the river, representing the the data point 'Natural conditions' in figure 6.17.	121

List of Symbols

A	area	m^2
B	width of the river main channel	m
c	transport velocity	m/s
C	mean concentration	kg/m^3
C_{orr}	cross correlation term	Int^2
D	turbulent diffusion coefficient	m^2/s
D_L	longitudinal dispersion coefficient	m^2/s
E	exchange velocity	m/s
G_t	skewness parameter	
g	acceleration due to gravity	m^2/s
h	water depth	m
I	slope of the energy grade line	
Int	measured light intensity	<i>counts</i>
J	mass flux	kg/s
k	exchange coefficient	
L	length of the groin field	m
L_x	length of the advective zone	m
K	exchange coefficient	$1/s$
M	mass	kg
Q	flow rate	m^3/s
q	mass flux per unit area	$kg/(m^2s)$
T_D	mean residence time of tracer in the dead-zone	s
t	time	s
U	mean velocity in the main channel	m/s
U_s	flow velocity in the main channel at the water surface	m/s
u, v, w	local velocity component in x,y,z-direction	m/s
u_*	shear velocity, defined as \sqrt{ghI}	m/s
u'	longitudinal component of the Root-Mean-Square-Velocity	m/s
R_D	hydraulic radius of the groin field	m
S	shape factor of the groins	
W	width of the groin field	m
α	inclination angle of the groin against the river bank	$^\circ$
δ	boundary layer width	
σ	standard deviation of a certain quantity	

Subscripts

D	certain quantity in the dead-zone
E	certain quantity at the exchange interface
S	certain quantity in the main stream
x	longitudinal or main component of quantity
y	lateral component of quantity (here also called transverse)
z	vertical component of quantity

1. Introduction

In the present study, mass transport phenomena in rivers have been investigated in order to improve the ability to predict pollutant concentrations after accidental spills (Fig. 1.1). The range of parameters affecting the transport characteristics is large. An important process that is still poorly understood is the effect of dead-water zones.

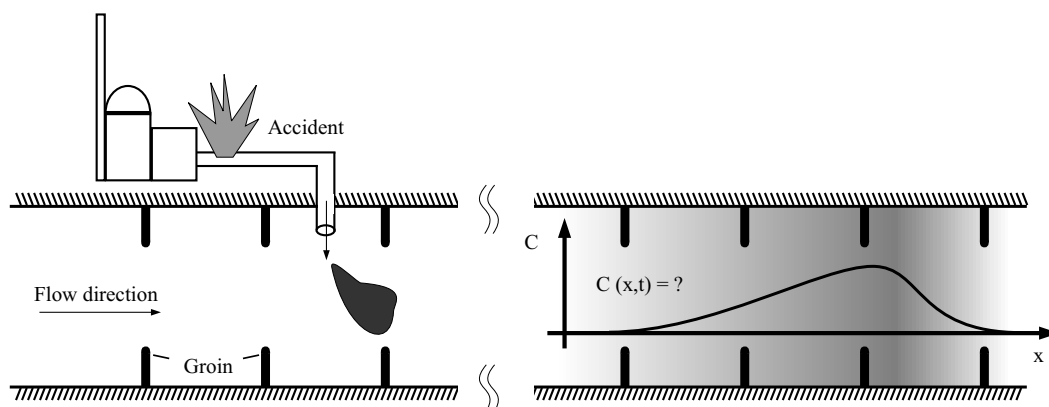


Figure 1.1. Schematic sketch of an accidental spill with the corresponding concentration curve far downstream of the accidental inflow

Dead-water zones are regions that are separated from the main channel, such, that the net flux in this region in the main stream direction is zero. An open contact area between main channel and dead-water zone enables mass and momentum exchange that leads to the typical recirculation movement of the water body. Dead-water zones can be formed by groin fields, side arms, harbors or any other irregularity in the river morphology which separates a certain part of the water body from the main stream. Exchange processes between dead-water zones and the main channel have a significant influence on the mass transport in rivers.

An important type of dead-water zones in rivers are groin fields. Groins have been constructed in many rivers to improve the shipping conditions and also to stabilize the thalweg position. In the present study, the main focus is to investigate the influence of a series of groin fields with different geometrical configurations on the mass transport characteristics. The discussion is mostly focused on groins that are non-submerged.

Dead-water zones cause an increase of longitudinal dispersion which means stronger lengthening of a released pollutant cloud in the main stream direction. This is due to two different effects. First, dead-water zones are the reason for a more distinct mean flow profile in the main stream which increases the effect of shear. Second, due to exchange

processes, mass gets temporarily stored in a dead-water zone and does not follow the mean flow velocity in the main stream any more. This second effect which amplifies the stretching is also the reason for a reduced transport velocity of the whole tracer mass, compared to the mean velocity in the main channel. An accurate prediction of travel time, maximum concentration and spreading of a pollutant cloud in rivers therefore requires an explicit consideration of the mechanism of these exchange processes.

1.1 Background

Accidental pollutant spills in rivers can influence the water quality over very large distances, up to several hundred kilometers. Therefore, the calculation of mass transport in such a large domain is mainly restricted to 1-dimensional approaches, which means that we have to deal with a problem of longitudinal dispersion. Longitudinal dispersion means that we look at the cross-sectionally averaged stretching of a tracer cloud, that is caused by the vertical and horizontal mean velocity distribution as well as by turbulent diffusion (section 3.2). Taylor (1954) was the first author who showed analytically and experimentally, that longitudinal dispersion is determined by the time-averaged velocity profile and turbulent diffusion in transverse direction. His theoretical and experimental work was restricted to turbulent pipe flows (for more details, see section 3.2.1). The theoretical work of Taylor has been proved by Aris (1959), using a method of moments to solve the Advection-Diffusion-Equation (ADE), where the concentration distribution is not described by the actual concentrations but by the moments of the distribution. Compared to Taylor's approach Aris' analysis is not restricted to all the simplifications (section 3.2.1). An extension for 2-dimensional unbounded shear flow has been performed by Elder (1959), where the velocity distribution in the vertical direction has been taken into account. Comparison with field data showed that Elder's approach strongly underestimates the stretching rate in real streams. Fischer (1967) showed that the depth-averaged transverse velocity distribution has much larger influence on the stretching rate than the vertical distribution. In his work an analytical method is derived to determine the longitudinal dispersion coefficient if the mean flow field in main stream direction is known as well as the transverse turbulent diffusion. In Fischer et al. (1979) he presented an approximation of his analytical solution where he adapted Taylor's results to typical geometries and flow distributions. He stated that the result is accurate within a factor of four. The explicit effect of dead-water zones on stretching rate and transport velocity is not included in this work. In different studies (Seo & Cheong 1998, Deng, Singh & Bengtsson 2001, Deng, Bengtsson, Singh & Adrian 2002) it has been tried to improve Fischer's 1-dimensional approach with the inclusion of extra parameters like channel shape or sinuosity. The resulting constants of proportionality are then optimized with many existing field data and appropriate fitting routines.

One problem in all of these approaches is that the shape of the concentration distribution is Gaussian with zero skewness. In most of the cases that have been measured in rivers, the concentration distribution contains a certain skewness, with a short rising

limb and a long falling tail. In the case of a pollutant spill a Gaussian type model can underestimate the concentrations when the maximum peak has passed. It has also been observed, that the transport velocity of the tracer cloud is smaller than the mean flow velocity in the main channel, which is of great importance in the prediction of pollutant transport scenarios.

To address this problem Hays, Krenkel & Schnelle (1966) developed the so-called dead-zone model, where the flow is divided into a main flow region and a stagnant region each described by a partial differential equation. He showed that these two coupled partial differential equations (section 3.4.1), which cannot be solved analytically, approximate the natural behavior of longitudinal concentration distributions much better than the original ADE. One problem of the dead-zone model are the two additional model parameters, which are the exchange coefficient and the cross-sectional fraction of the dead-zone. Hays et al. (1966) stated that it seems to be impossible to predict these model parameters with the help of geometrical or bulk hydraulic parameters. In the work of Thackston & Schnelle (1970) the dead-zone parameters are predicted with the help of field data. In his results the exchange coefficient that described the intensity of the mass exchange between dead-water zone and main stream is taken to be constant $k = 0.05$ and the cross-sectional fraction of the dead-zone volume which determines the transport velocity is a function of the friction factor. This approach seems to be valid for natural dead-zones like pools in the river bed. The affects of groin fields, however, cannot be predicted by this approach. Valentine & Wood (1979) performed laboratory experiments to determine the exchange coefficient with dead-zones at the channel bottom. The results showed that the mean exchange coefficient is 0.02 ± 0.01 with no clear dependency on the dead-zone geometry. With this result and numerical simulations to determine the moments of the concentration distribution they showed that the mass in the two zones of the dead-zone model is proportional to the zone volume, and that the transport velocity in both zones is equal. In the work of Nordin & Sabol (1974) field data from tracer tests are presented that are used by Nordin & Troutman (1980) to predict the dead-zone parameters using an analytical evaluation of the moments of the concentration distribution. They showed that even with the application of the dead-zone model it is not easy to describe the skewness because also in the dead-zone model, too, the skewness tends to zero.

An extension of the dead-zone model was given by Denton (1990), who included a parabolic vertical velocity distribution in the vertical direction in the main stream. With the method of moments, he showed, the relation between the fraction of the dead-zone volume to the 1-dimensional longitudinal dispersion coefficient. His results are in good agreement with the experimental data given by Valentine & Wood (1979).

Up to this point all considerations have been made about conservative tracer material. Reactive tracer material assuming reaction kinetics of first order have been introduced into the dead-zone model by Schmid (1995). He determined analytically the different moments of the dead-zone model for an initial slug release under the influence of a first order decaying tracer. He showed that the influence of the tracer decay on the stretching rate and the skewness is almost negligible. A comparison (Schmid 1995) between numerical results of the dead-zone model and approximations with self similarity functions

(truncated Edgeworth series expansion, (Chatwin 1980) or Pearson Type III distribution (Holley & Jirka 1986)) showed, that Pearson Type III distribution represents the results of the dead-zone model best. In a recent paper of Seo & Cheong (2001) a large data collection is presented with the aim to estimate the dead-zone parameters for different flow characteristics.

Because none of these studies can predict the relation between dead-zone geometry at the channel bank and the exchange parameter, different studies have been performed in the laboratory to measure this parameter. Most of the studies have been performed for single dead-water zones, like harbor facilities or cooling ponds (Westrich 1978, Booij 1989, Kimura & Hosoda 1997, Altai & Chu 1997). However, in the work of Uijttewaal, Lehmann & van Mazijk (2001) it could be shown that the exchange in a series of dead-zones varies significantly between the first dead-zone and a dead-zone further downstream after the mixing layer is fully developed, which means that the results mentioned above do not represent the behavior of groin fields very well. In an experiment of Westrich (1978) concentration measurements to determine the residence time have been performed with fluorescent dye and a multi-port sample probe. The influence on the exchange process of different opening sections, water depth and bottom roughness have been investigated in this study. In order to achieve a homogeneous concentration field in the dead-zone as initial condition in the dead-zone, the opening section between the dead-water zone and the main stream has been closed before each experiment. The initial period in Westrich's experiments is therefore strongly influenced by the spin-up process in the dead-zone. This problem has been avoided in the experiments of Altai & Chu (1997), using an upstream source in the main channel along the wall on the side of the dead-zone. After a period of time when the concentration in the dead-zone had reached a steady state, the dye supply was stopped and the experiment started. In this experiment depth-averaged planar concentration measurements were performed, using Planar-Concentration-Analysis (PCA), a technique that has been further developed by Kurzke, Weitbrecht & Jirka (2002) and von Carmer, Rummel & Jirka (2003) von Carmer et al. (2003).

In the study of Altai & Chu (1997) two square basins of different size have been used to analyze the influence of the water depth and the main stream velocity. The exchange values given in this study lie in the range given by Valentine & Wood (1979), with no clear relation to the flow velocity and the water depth. Chen & Ikeda (1997) presented experiments in a single groin field with varying aspect ratio (width to length of the dead-zone) from 1 to 0.1. Besides surface wave measurements they presented 2-dimensional point velocity measurements, that have been performed at many points to give an overall impression about the mean flow field. The mean velocities at the interface between dead-water zone and main stream have been used to determine the dimensionless mass exchange coefficient. Because of an unusual way of normalizing, the exchange data in this study are hard to compare with other results. Lehmann (1999) performed experiments in a series of groin fields where two different aspect ratios have been analyzed. In this study, surface Particle-Tracking-Velocimetry (PTV) measurements and depth averaged concentration measurements (PCA) have been used to analyze the exchange behavior between main channel and groin field. The tracer has been injected manually into the groin

field without separating it from the mean flow. Therefore, no reproducible homogeneous concentration distribution could be achieved as initial condition for the experiment. The results, summarized in Uijttewaal et al. (2001), show that the exchange value is not strongly influenced by the shape of the groins and it is independent of the main stream velocity. The determined exchange values lie in the range given by Valentine & Wood (1979). Also in that study no clear relation between groin field geometry and exchange coefficient could be given.

An application of this knowledge is given by the 1-dimensional "Rhine-Alarm-Model" that is used online for the management of accidental pollutant releases (Spreafico & van Mazijk 1993, van Mazijk 2002). The Rhine-Alarm-Model was developed by the "International Commission for the Hydrology of the River Rhine" (CHR) and the "International Commission for the Protection of the Rhine" (ICPR) after the accidental Sandoz spill in 1986, where a large amount of toxic chemicals (among others dioxines) was released into the river Rhine. For this kind of predictive model, much effort and expense must be spent on calibration by means of extensive in-situ tracer measurements. The Rhine-Alarm-Model uses a one-dimensional analytical approximation for the travel time and concentration curve given by Chatwin (1980) and Nordin & Troutman (1980). In this model the dispersion coefficient and a lag coefficient have to be calibrated with tracer tests. The model works well for cases of hydrological situations that are similar to the calibration conditions. However, variations in discharge, and thus, changes in water surface levels lead to increased errors if the same calibrated parameters are used for different hydrological situations. Insufficient knowledge about the relation between river morphology and transport processes are the reason for these uncertainties. Hence, predictive methods that are appropriate for variable flows and therefore variable morphological conditions are needed.

1.2 Outline

The present study can be divided into four major parts:

- 1) A survey of existing groin fields in rivers has been performed. With the help of detailed maps of parts of the river Elbe, Rhine/Waal and Danube, the most typical morphological conditions in groin-regulated parts of these rivers have been determined.
- 2) The theoretical background of turbulent mass transport in rivers has been described.
- 3) Laboratory experiments have been performed, where the flow and transport characteristics in typical groin fields have been measured with detailed PIV and PCA measurements.
- 4) A Lagrangian-Particle-Tracking-Method has been developed to transfer the results obtained with the experiments at a single dead-water zone into transport characteristics in the far-field of the tracer release point.

The laboratory experiments (chapter 4) were conducted in a 20 m long and 1.80 m wide tilting flume, where one side of the flume is intended to represent the channel mid-section and the other side the river bank including the groin fields. In order to determine the influence of varying geometrical conditions, experiments have been performed where the aspect ratio W/L (width/length) of the the dead-water zone was altered as well as the inclination angle between groins and the main stream direction (section 4.4). A survey of natural rivers that has been conducted in order to specify typical geometrical conditions of dead-water zones showed huge varieties (section 2.2). The experiments represent typical groin field conditions as they have been found in the Rivers Rhine and Elbe in Germany as well as the River Waal in the Netherlands.

In the present study PIV measurements were performed to analyze in detail the flow dynamics in the dead-zone as well as in the mixing layer between the groin fields and the main stream (section 4.2.1). The resulting instantaneous velocity fields with high spatial resolution are leading to mean flow values as well as turbulent flow characteristics. Experiments by Uijttewaal et al. (2001) showed that the mass transport between dead-zone and main stream is dominated by large horizontal coherent structures that are generated at the groin head. These structures are advected within the mixing layer and transfer tracer mass from dead-zone to main stream and vice versa. The evaluation of vorticity fields enables us to visualize these structures and to observe their behavior in the mixing layer. Furthermore, the velocity measurements have been used to get information about the exchange processes by integrating the transverse velocity components along the streamline which separates the dead-water zone and the main stream (section 5.1.7).

In addition to the PIV measurements, dye experiments have been conducted for the purpose of analyzing the depth-integrated mass exchange using PCA (section 5.2). The idea is to inject tracer homogeneously distributed instantaneously into one groin field, and to observe the spatial averaged decay of concentration in this area. The mass injection has been realized with the aid of a Multi-Port-Injection-Device (MPID) (section 4.3.1) that acts as a plane source. To process the obtained picture frames, a program has been developed to perform gray scale analysis taking into account the typical laboratory uncertainties such as varying illumination conditions or changing background concentrations (section 4.3).

The overall goal of these investigations was to determine the influence of dead-water zones on transport processes in the far-field of a mass release in terms of 1-D transport parameters like dispersion coefficients or transport velocities. Therefore, it is necessary to transfer the results obtained in a single dead-water zone into a system of many dead-water zones. To solve this problem a Lagrangian-Particle-Tracking-Method (LPTM) has been developed using the properties of a random walk model (chapter 6). In this approach the two governing processes which cause dispersion, namely shear advection and transverse diffusion, are acting on a virtual cloud of many particles. The evaluation of the statistical behavior of the particle cloud during the simulation finally gives us the information about the integral transport characteristics in a river.

In addition to predicting the longitudinal dispersion coefficient it is hence possible to make a prediction about the transport velocity, which is noticeably smaller in the presence

of groin fields than the mean flow velocity in the main channel of a river. The required flow data, like mean flow profile or the turbulent diffusive motion in transverse direction, are obtained from the laboratory experiments. Thus, predictions for the transport parameters can be made for different geometrical configurations of dead-water zones, which is currently one of the uncertainties in existing alarm models.

2. Characterization of Dead-Water Zones in Rivers

Mass transport of dissolved matter in rivers is strongly related to the given flow characteristics like mean flow velocity, velocity distribution, secondary currents and turbulence intensities. These parameters are mainly determined by the river morphology and the discharge conditions. Most natural rivers are characterized by a strong diversity of morphological conditions. Changing river width, curvature, bed form, bed material and vegetation are the reason for this diversity, which has strong effects on the transport mechanisms. In rivers which are regulated by man-made constructions, such as dikes, groins, stabilized bed and so forth, the morphological diversity is often less pronounced. In these rivers the flow velocities are more homogeneous, which means that the mass transport is expected to be less dispersive.

One important process, which has influence on the dispersive mass transport, is given by exchange processes between dead-water zones and the fast flowing water body in the main channel (Valentine & Wood 1979). Dead-water zones can be described as a geometrical irregularity, within which the mean flow velocity in main stream direction is zero. Due to momentum exchange over an open contact area with the main channel, the mean flow patterns in the dead-water zone are governed by recirculating gyres.

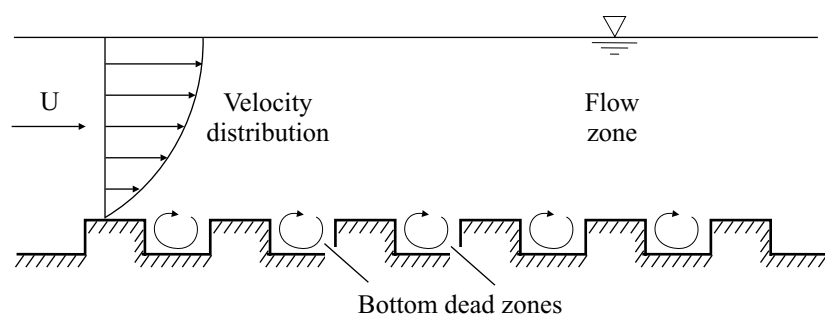


Figure 2.1. Sketch of idealized dead-water zones at the bottom of a flow field adapted from Valentine & Wood (1979)

In natural rivers, dead-water zones can be formed by sand or gravel banks, side arms or any other irregularity in the morphology that leads to recirculating flows in a separate part of the water body. Valentine & Wood (1979) treated even small pockets at the river bed as dead-water zones.

In rivers which are strongly regulated by man-made constructions, groin fields are the most important sort of dead-water zones. Groin fields can cover large parts of the river, which means that the storage capacity of these areas is comparatively big. In the following

sections an overview is given about typical groins in different rivers, about how the flow field in the presence of groin fields is characterized, and about how these flows act on the transport processes in a river.

2.1 General characteristics of groins

In figure 2.2 the most important terms are defined, which are used in the present study to describe groins and the associated flow and mixing phenomena.

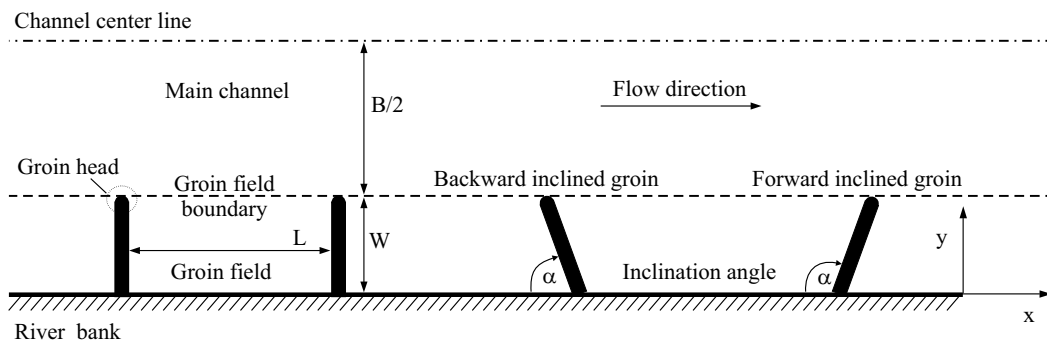


Figure 2.2. Schematic sketch to define the terminology used in the present study

Figure 2.3 shows a drawing of a typical groin structure as was built in the river Elbe around 1890. Layers of faggots fixed with layers of heavy materials represent the core of such a groin. The groin head is protected with a layer of paving stones. The standard groin has a slightly inclined crest (about 1:150) and side slopes from 1:1 up to 1:3.5.

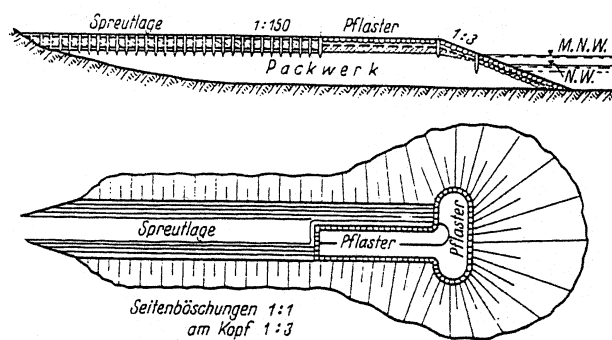


Figure 2.3. Top view and cross-sectional view of a groin from the river Elbe, taken from Neger (1932)

Groins are constructions that extend out from the bank of a river or from the shore line into the water. In the present work only river groins are considered. River groins are mainly used for the following purposes:

- a) To prevent bank erosion and protect structures along the bank
- b) To cut off side channels in order to have a single main channel with sufficient water depth
- c) To concentrate a braided river into a single channel
- d) To constrict a channel in order to increase the water depth in the main channel which is necessary for shipping purposes in low water periods
- e) To stabilize the main channel at a certain position in order to realign a river reach

The point of increasing the water depth in the main channel is leading to certain controversies. If a river serves as a waterway (figure 2.4), it is desirable to have efficient shipping conditions during the whole year. Therefore, groins are built to increase the water level in low water periods. On the other hand, the construction of groins should not increase the water level in high water periods so that the embankments are not endangered. The compromise is mostly found such that the crown elevation of the groins is planned to have the same level as the water level during mean discharge conditions. This means that during periods with high water discharge these groins are fully submerged.



Figure 2.4. Aerial photograph of groin fields in the River Rhine close to Emmerich showing the density of the shipping traffic

The construction of groins leads to increased flow velocities and therefore to increased erosion processes in the main channel of the river. This is the reason why the planned crown elevation does not always correspond to the final water surface elevation which means that the crown elevation varies from reach to reach.

Groins are aligned either at an angle or perpendicular to the flow. Experience showed that backward inclined groins, e. g. groins that are inclined slightly against the flow direction, are more effective than forward inclined groins with an inclination angle larger than 90° (Riepe 1930). In the River Elbe the first groins were built around 1500 with the purpose of gaining farmland. In that case very long forward inclined groins were chosen to support sedimentation within the groin fields. However, due to bank protection problems this kind of groins no longer exists. In cases of high water discharge groins act like a weir. If the groins are inclined in downstream direction, the overflowing water is directed to the river bank and can provoke damages (Lange & Lecher 1989). In recent investigations the positive effects of forward and backward inclined groins are combined by using groins with a kink (figure 2.5). In the work of Hentschel & Anlauf (2002) prototypes kink-groins were built in the River Elbe. They showed, that an improved ecological situation is achieved in terms of bio-diversity, while other parameters, like bank protection and water depth, are not effected with these kind of groins.

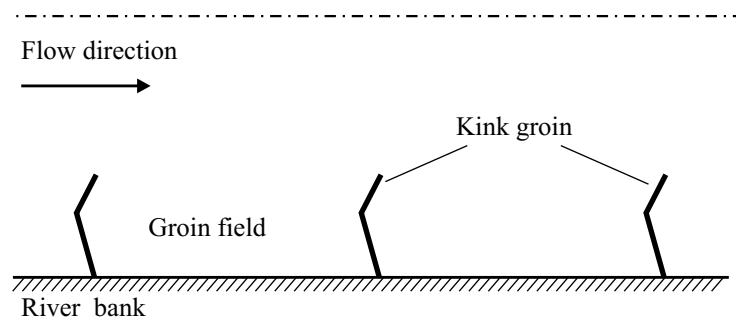


Figure 2.5. Schematic sketch of a prototype groin combining the positive effects of different inclination angles

The length of a groin depends on its location, the amount of channel constriction desired, and the spacing of groins in a system. In the river Rhine the length of a groin varies between 30 and 100 meters. The first groins in the river Elbe had a length up to 300 meters where at the present stage only the groin heads are visible.

The spacing L between groins is a function of the location of the next groin downstream in a system. In typical groin regulated rivers after Petersen (1986) the ratio between groin length W and spacing L is between 0.6 and 0.17. The aspect ratio W/L determines the overall flow patterns in a groin field which determines the mass exchange between groin field and main channel. Therefore, W/L is one of the central parameters in the present study. The influence of varying W/L on the typical flow patterns in groin fields is shown in section 5.1.2.

2.2 Typical groin field geometries

In this section results of a literature review are presented that has been performed to determine typical groin field geometries as they occur in nature. These results are the basis for the laboratory experiments described in section 4.4.

The morphology of a groin field is not only determined by the length, width, and shape of the groin, but also by the development of the groin field bottom which is in a constant process of deposition and erosion. This process starts immediately after the construction of the groins and can reach a certain equilibrium in periods where no exceptional hydrological events occur. The development of scours at the groin heads and on the other hand the development of sand banks in the center region of a groin field are typical processes that determine the morphological evolution of the system.

In recent studies (Hinkel 1999, Hannappel & Pierho 1996), aerial photography was used as a method to figure out typical classes of deposition and vegetation patterns. Sukhodolov et al. (2002) worked out a simplified version of Hinkel's classification that contains seven classes of deposition patterns where the differences in vegetation are neglected (figure 2.6). In (figure 2.7) a typical aerial photograph of the River Elbe at km 490 is given, showing the different classes of deposition pattern. Although this classification contains a strong diversity in the deposition patterns, it is still a simplification that covers only a certain range of different conditions.








Class	Definition	Pattern
1	Weak deposition	
2	Upstream triangle shaped deposition	
3	Downstream triangle-shaped deposition	
4	Upstream wave-shaped deposition	
5	Downstream wave-shaped deposition	
6	Uniform partial deposition	
7	Uniform complete deposition	

Figure 2.6. Simplified classification of sedimentation patterns in groin fields taken from (Sukhodolov et al. 2002)

In the work of Hinkel (1999), 2000 groin fields within a river section of 200 km length were analyzed. It turned out that the most important deposition pattern is represented by Class 6 (figure 2.8), where deposition in the groin field occurs partially, but uniformly. Groin fields with almost no deposition, which are represented by class 1, occur with a 10% probability.

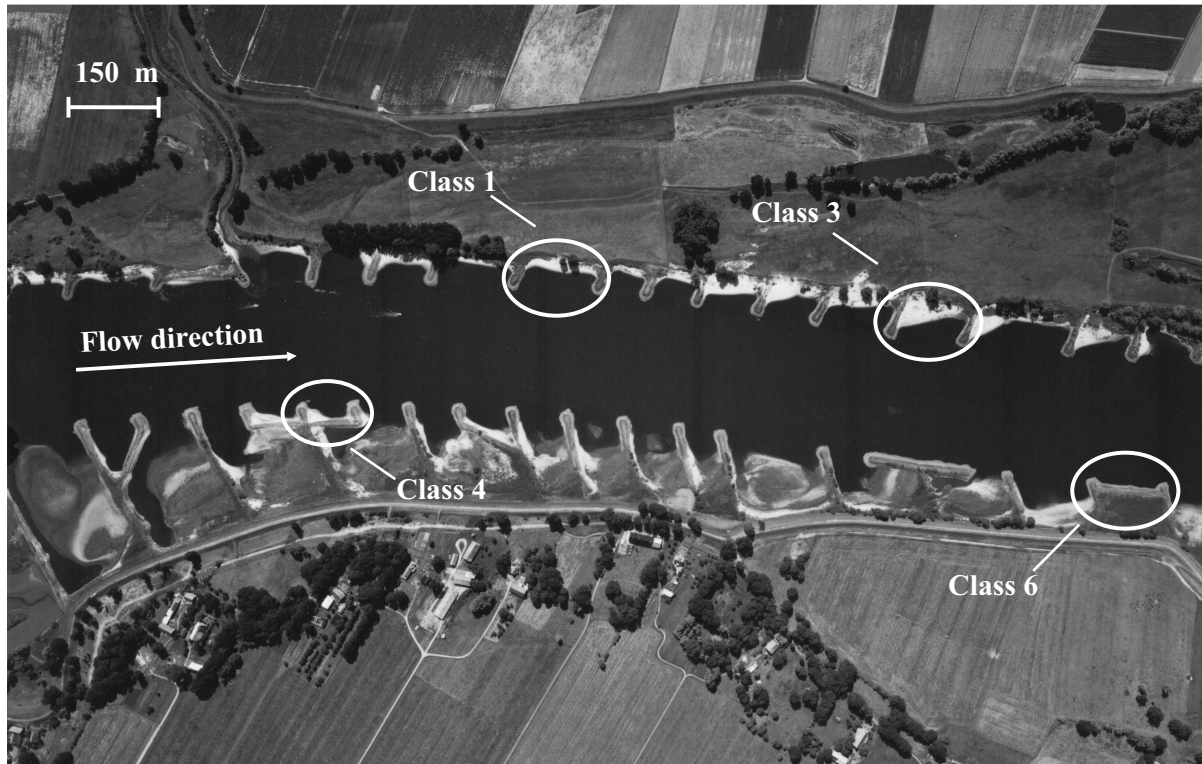


Figure 2.7. Aerial photograph of the River Elbe taken at km 490, with low discharge conditions, where the different groin classes, defined in figure 2.6, are denoted; authorized by Wasser- und Schifffahrtsdirektion Ost, Berlin

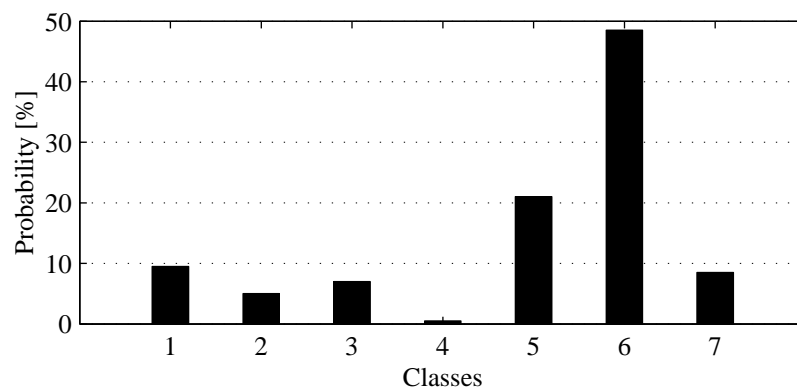


Figure 2.8. Probability distribution of the occurrence of groin field geometries in the River Elbe (Hinkel 1999)

From the hydrodynamical point of view it can be stated, that class 6 is a subclass of class 1 with a smaller W/L ratio. That means, that the expected flow patterns class 1 and 6 should be the same, if we assume the same width to length ratio. The experiments presented in section 4.4 cover the classes 1 and 6 which represent over 60% of the existing groin fields in the river Elbe.

With this result it can be stated that the aspect ratio W/L is an important parameter to characterize the morphology of a groin field as well as the flow conditions in such an area. Therefore, it appears that also mass exchange should be influenced by this parameter.

In order to determine typical aspect ratios that occur in the nature, map material from different parts of the rivers, Elbe, Rhine and Waal have been analyzed.

In figure 2.9 a typical part of a topographical map is shown, which was used to analyze the geometrical conditions in the groin fields. For analysis of the groin fields in the River Rhine from river-km 288-376, the map for "industry and navigation" with a scale of 1:15000 was used. More than 1400 groin fields were found in this section of the Rhine. The mean spacing between the groins was determined to be 120 meters and the average length of the groins is 65 meters. This leads to a mean aspect ratio W/L of 0.53.

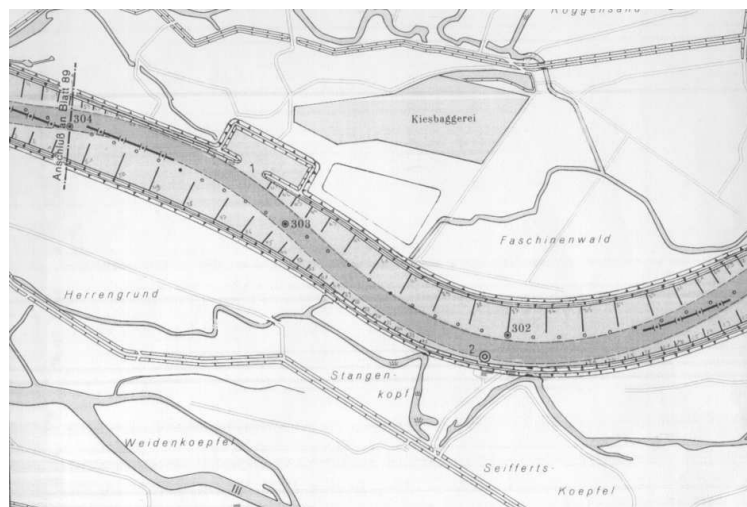


Figure 2.9. Groin fields in the River Rhine at km 302-304

The distribution of the occurring aspect ratios within this river section is shown in figure 2.10. It can be seen that the distribution of W/L between values of 0.1 and 1 is relatively homogeneous, which can be explained with figure 2.9. The groin length is changing from groin to groin and differs from side to side. That means, if there are long groins on the left bank, the groins on the right bank are very short or even nonexistent. This arrangement of alternating groins leads to a main channel that meanders between left and right river bank (if the groins are not fully submerged).

If we compare the results from the River Rhine to the typical groin field configuration in the River Waal, which is a side branch of the Rhine in the Netherlands, we see that mean spacing between the groins is 200 meters. This is a much higher value than observed in the River Rhine. Because the mean length of groins is almost the same as in the Rhine, the mean aspect ratio W/L in the Waal is determined to be 0.34 which is much smaller compared to the Rhine. Another difference can be derived from the probability distribution of the aspect ratio in the investigated river section (figure 2.11). It can be seen that the distribution has a peak which means that the groin field configuration in the Waal is more regular. The groin field length does not change from groin to groin as in the case of the River Rhine but remains more or less constant which can be seen in figure 2.12.

In the work of (Hinkel 1999) about groin fields in the Elbe the groin length was not analyzed because of uncertainties in defining the origin of a groin out of aerial photographs

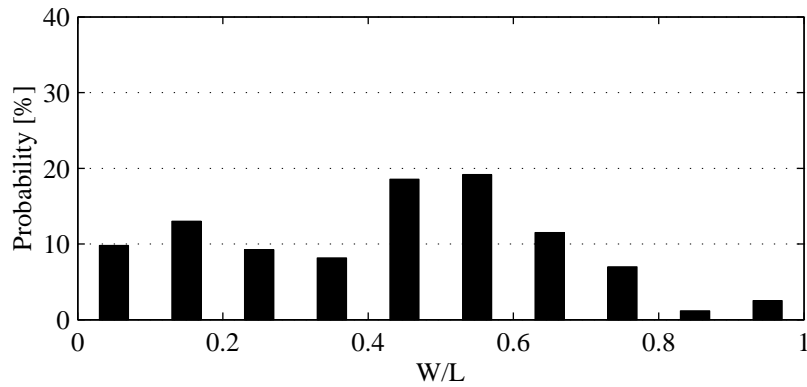


Figure 2.10. Probability of occurring W/L aspect ratios within the River Rhine km 288-376

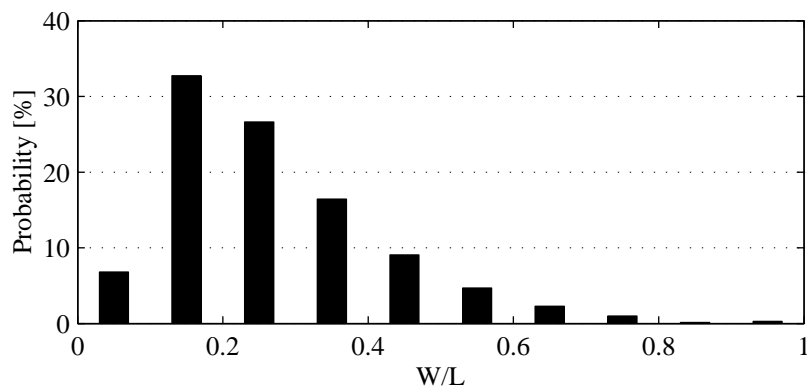


Figure 2.11. Probability of occurring W/L aspect ratios within the River Waal km 857-859

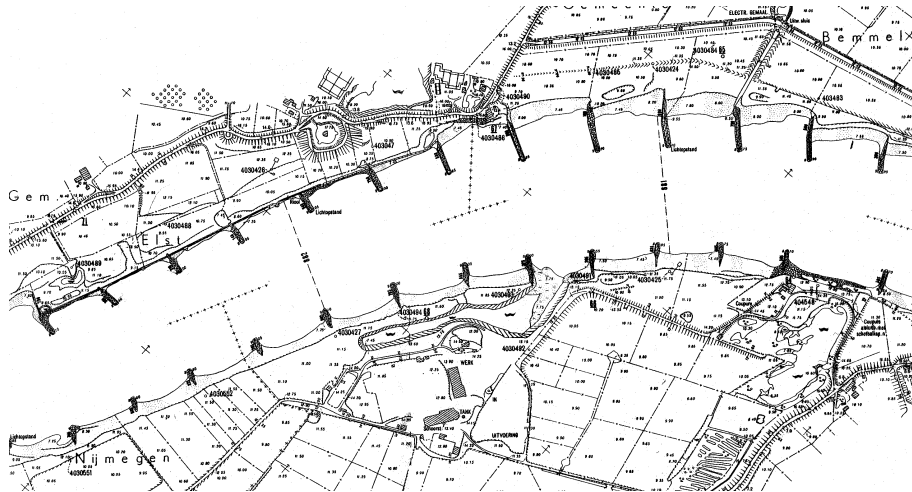


Figure 2.12. Groin fields in the River Waal at km 881-882

(figure 2.7). In order to determine a typical W/L ratio, topographical maps were used from a short section of the River Elbe (km 359-373), containing 120 groins. The mean aspect ratio within this section has been determined to be 0.8. Another interesting parameter in this case is the inclination angle of the groins with respect to the flow direction. In the cases of Rhine and Waal the groins are almost perpendicular to the flow direction. In the

River Elbe the situation is somewhat different. Here the groins are inclined against the flow direction with an angle that deviates about 25° from the regular case, (figure 2.7) which leads to significant changes in the flow patterns (section 5.1.2).

2.3 Qualitative description of flow patterns in groin fields

The flow in dead-water zones is mostly characterized by recirculating flows, with a mean flow velocity in the main stream direction which is zero. One or several rotating gyres can form the flow patterns in such an area, depending on the water depth and the shape of the dead-water zone. In groin field flows we have to distinguish two cases. In periods of high discharges the groins are submerged so that they act like small weirs with strong vertical turbulent motion behind the groins. In that case the mean flow velocity in the groin field is not zero because of the water that flows over the groins. Therefore, we look only at the non-submerged case where the water level is equal or less than the groin crest.

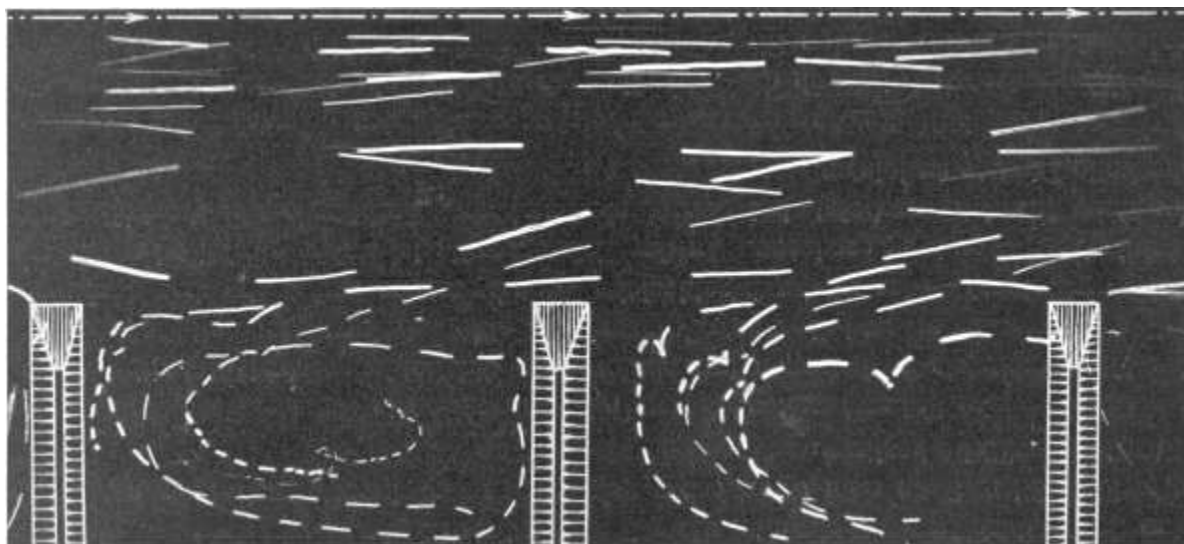


Figure 2.13. Velocity measurements using intermittent photography of floating candles, exposure time = 1s, with a main flow direction from left to right, taken from Rehbock (1926)

In groin fields where the water level is less than groin height, the flow is determined in most cases by a system of one or two rotating gyres described first by Rehbock (1926). In Rehbock's experiment floating candles were used to visualize the flow patterns (figure 2.13). In figure 2.13, the white lines correspond to an exposure time of one second. Comparing the line length in the groin field with the result in the main stream it can be stated as a rough estimate, that the flow velocity in the primary gyre is about one fourth to one fifth of the flow velocity in main stream.

The parameter which is responsible for the evolution of a one or two gyre system is the aspect ratio W/L . With measurements performed in dead-water zones formed by harbors, Booij (1989) showed that for $0.5 < W/L < 1.5$ a single rotating gyre is

established in the dead-water zone that covers almost the complete area of the dead-water zone (figure 2.14, ii). This gyre can be deformed until its length is twice the width. If the aspect ratio of a groin field is smaller than 0.5, a second gyre starts to develop in the upstream corner of the groin field (figure 2.14, iii). This secondary gyre has no contact area with the main stream which means that it is driven by momentum exchange with the primary gyre. The flow velocities are therefore much smaller in this area. For W/L values larger than 1.5 which is not typical for groin fields but for harbors, a two gyre system evolves, where the secondary gyre is located behind the primary gyre in transverse direction to the main stream (figure 2.14, i).

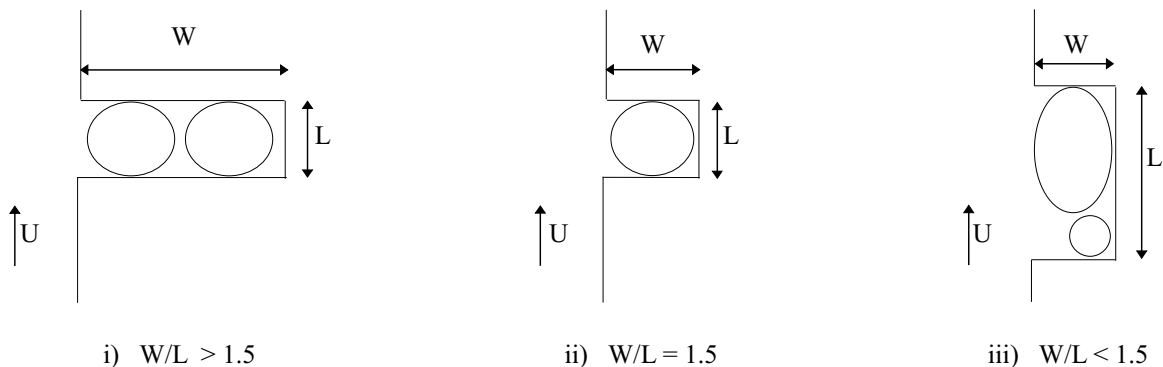


Figure 2.14. Influence of the aspect ratio W/L on the gyre configuration in a dead-water zone taken from Lehmann (1999)

In order to optimize the spacing between two groins different parameters have to be taken into account. If the groin fields are very narrow $W/L > 1.5$ the momentum exchange with the secondary gyre close to the river bank is very weak. This means that there is almost no movement in the water body which rises many problems in terms of water quality. The second problem arises from an economical point of view. The larger the aspect ratio, the larger the number of groins needed and the higher the costs. For bank protection purposes, however, a high W/L ratio would have a positive effect.

On the other hand, we can think of very long distances between the groins with a small W/L ratio. In the most extreme case the downstream groin does not feel the influence of the upstream groin, which means that the flow penetrates into the groin field and touches the channel bank (figure 2.15). In that case the mean flow velocity in the main channel is changing in longitudinal direction due to a changing constriction factor. At the position of a groin the flow velocity would be much higher than in the region where the flow touches the river bank. It is clear that this situation is not desirable because of insufficient bank protection and because of more difficult navigation. If we decrease the spacing between two groins the situation gets more and more stable towards a two gyre system. But it has to be noticed that even if the mean flow pattern in the groin fields show a stable two gyre situation, the instantaneous flow field shows a different behavior. In such cases it happens that these gyres are moving in lateral and longitudinal position, which can lead to alternating flow velocities in the main stream (section 5.1.5). These

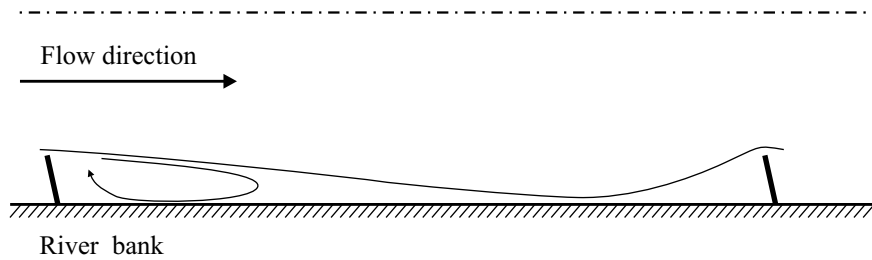


Figure 2.15. Schematic sketch of the flow patterns in groin fields for very small aspect ratio W/L .

additional transverse flow velocities have to be avoided by decreasing the spacing until a stable situation is achieved.

The flow patterns in the groin field are also influenced by the inclination angle α between the groin fields and the main stream direction (figure 2.16). Forward inclined groins with inclination angles larger than 90° increase the size of the secondary gyre in the upstream corner of the groin field. Backward inclined groins with α smaller than 90° have an opposite effect. The secondary gyre is smaller which means, that the area with very low flow velocities covers a smaller part of the groin field.

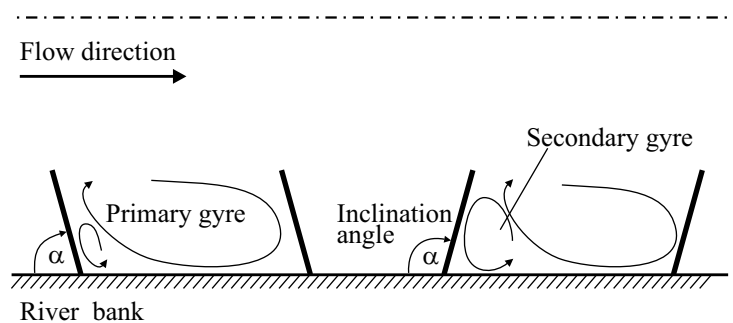


Figure 2.16. Schematic sketch of groin fields with different inclination angles and their influence on the development of the two gyre system

An important feature of the flow field in groin fields is the transition region between the dead-water zone and the main stream called mixing layer. It is characterized by a time-averaged velocity profile shown in figure 2.17, i with the typical negative flow velocities close to the channel bank due to the recirculating movements.

In rivers the flow is usually very shallow which means, that the horizontal dimension of the flow is much larger than the water depth. This shallowness of the flow is the reason for the development of large coherent structures within the mixing layer. These flow structures emerge because of separation effects at the upstream groin heads and travel downstream within the mixing layer. During their travel they grow predominantly in horizontal direction and reach a final extension which is again much larger than the water depth (figure 2.17, ii). These structures are travelling into the dead-zone or remain in the main stream and therefore play an important role in terms of exchange processes between the main stream and the dead-zone.

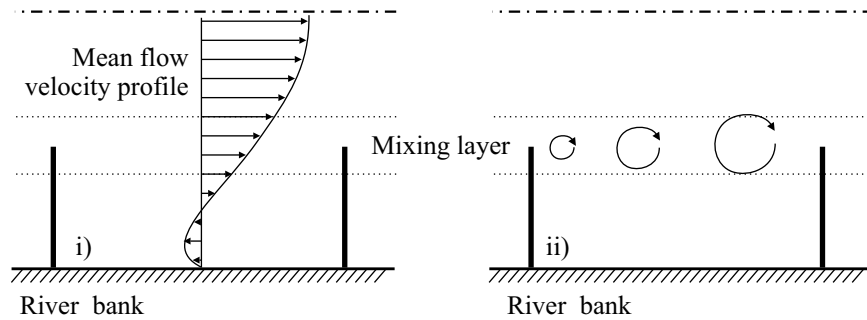


Figure 2.17. Characterization of the flow in the mixing layer; i) Mean velocity profile across a groin field and the mixing layer, ii) Schematic sketch of large coherent motions that emerge at the groin heads and grow during their travel downstream

2.4 Qualitative description of transport processes due to groin fields

The most important process that determines the effect of dead-water zones on the mass transport in rivers is the storage of mass for a certain time T_D . Mass that travels downstream within the main stream gets trapped in the dead-zone, remains there an average time T_D , and gets back into the main stream. The exchange of mass between the dead-water zone and the main stream results from the following processes:

- a) Mass exchange due to turbulent mixing, governed by two-dimensional coherent motions in the mixing layer between dead-water zone and main stream
- b) Mass exchange due to advection in the case of water level changes, which can be caused by passing ships or hydrological water level changes
- c) Mass exchange due to surface shear stresses induced by wind
- d) Mass exchange due to density differences that can be caused by temperature changes because of solar radiation

In the present study the focus is on the first item, because we assume this process to have the strongest influence on the mass exchange, which can be explained mainly with the fact that turbulent mixing is a constant process, whereas the other processes occur only temporarily. In periods of high shipping density this can also have an influence on the mass exchange. Passing ships can increase drastically the mass exchange for very short intervals. Due to surge waves a large percentage of the water contained in the dead-water zone can then be washed into the main stream (Guhr 2002).

In the previous section the existence of large two-dimensional coherent motions in the mixing layer has been mentioned. These rotating flow structures lead to increased concentration gradients and therefore they amplify mixing processes in transverse direction. Moreover, these structures can travel into the groin field before they reach the downstream groin. They can be relatively large, which means that the amount of mass which is transported in that manner into the groin field is dominating the exchange process between groin field and main stream.

The effect of these exchange processes can be quantified by looking at two different transport parameters: the mean transport velocity c , defined as the velocity of the center of mass of the tracer cloud, and the longitudinal dispersion that describes the stretching rate of the tracer cloud. In a channel without dead-water zones we assume that the transport velocity of a tracer cloud that is well mixed over the river cross-section is the same as the mean flow velocity. If, there are dead-water zones, mass that stays in these zones gets retarded compared to the mass that travels in the main channel with the mean flow velocity. In that case, the transport velocity c of the tracer cloud is lower than the mean flow velocity. Translated into a scenario of an accidental spill, the pollutant reaches a certain position later than a calculation would predict, which uses the mean flow velocities calculated by hydrodynamical models.

The second effect of the mass exchange can be described as an increased stretching of a passing tracer cloud which means that the longitudinal dispersion is increased. This effect can be explained by two processes. First, the presence of groin fields alters the mean flow profile in the main channel and enhances turbulent mixing in transverse direction, which are the determining parameters for longitudinal dispersion (section 3.2). The second process that influences the stretching of a tracer cloud is caused by the retention of mass in the dead-water zones compared to mass that travels in the main channel. This shows, that longitudinal dispersion is expected to be much stronger in the presence of groin fields. In the case of an accidental spill, this process leads to strong uncertainties in the prediction of how long critical concentration values are exceeded. Increased longitudinal dispersion leads to smaller peak levels but the period during which critical values are exceeded can be much longer.

All these processes are strongly related to the geomorphological conditions of the dead-water zones. Hence, in order to predict transport characteristics in rivers these dependencies must be understood.

3. Transport Processes: Theoretical Background

In the following chapter the basic concepts of mass transport of solute material in open channel flows are described, including the derivation of the governing transport equations. The analysis of Taylor (1954) to predict longitudinal dispersion in turbulent pipe flows that leads to the 1-dimensional Advection-Dispersion-Equation ADE is discussed in detail. In a further step the extensions for dispersion in rivers following Fischer et al. (1979) is presented. Because in many cases field observations differ from the results that are obtained with solutions from the ADE, due to skewness and reduced transport velocity, alternatives to the ADE, like the dead-zone model and random walk models are discussed.

3.1 Basic processes

The transport of mass in fluid or gas flows, can be described as the interplay of the three following physical processes:

- 1) Diffusion
- 2) Advection
- 3) Transformation

Transport due to advection means that mass of a certain species gets transported by the movement of the surrounding medium. Advective motion has a certain direction which is determined by flow field. Diffusion describes a transport mechanism that is characterized by random movements of the surrounding medium, which forces a tracer to spread out in any direction.

Transformations are processes that change the amount of mass of a certain species due to physical, biological or chemical reactions. In the present study we focus on conservative tracers, which means that transformation processes are not taken into account. In the case of accidental spills, the influence of transformation processes can often be approximated by first order reactions.

Longitudinal dispersion is not mentioned in the list of basic transport processes above, because it can be described as a combination of advection in shear flow and diffusion in transverse direction to the flow. In the present study, where the transport of pollutant spills is analyzed in very long river reaches, longitudinal dispersion is the dominating process and is described in section 3.2.

3.1.1 Diffusion

Diffusion can be described as the transport of a certain quantity due to random movements. In the case of molecular diffusion, Brownian motion leads to mass transport. Diffusion can be described using Fick's law (equation 3.1) that succeeds the following principle: The mass flux is proportional to the concentration gradient, and it is directed from high to low concentrations. The one-dimensional, diffusive mass flux per unit area in x-direction, can therefore be derived to be

$$q_x = -D \frac{\partial C}{\partial x} \quad (3.1)$$

with:

q_x	=	mass flux per unit area
D	=	diffusion coefficient
C	=	concentration

The diffusion coefficient D has the dimensions of [m²/s] and can be interpreted as the product of a characteristic length and a characteristic velocity.

In turbulent air or water flows, a higher order diffusion process takes place, called turbulent diffusion. This process reflects the interplay of molecular diffusion and micro advection. The flow in turbulent eddy motions leads to random advective motion in all directions and causes increased concentration gradients, resulting in increased molecular diffusion. Taylor (1921) conducted experiments in turbulent pipe flows, where he showed that a particle cloud grows linearly with time, which is in analogy to a Fickian type of diffusion. This means that the spreading of a particle cloud due to the random turbulent motions of the surrounding fluid can be described using Fick's law as well, where the diffusion coefficient is some orders of magnitude larger than in the case of molecular diffusion.

In rivers, turbulent diffusion in vertical and lateral direction has to be considered separately. Vertical mixing in a wide open channel is characterized by the water depth h , that represents the maximum size of the turbulent eddies, and the shear flow velocity u_* which characterizes the turbulent behavior of the flow

$$u_* = \sqrt{Igh} \quad (3.2)$$

with:

I	=	slope of the energy grade line
g	=	acceleration due to gravity
h	=	water depth

Assuming a logarithmic velocity profile, Fischer et al. (1979) showed that the turbulent diffusion coefficient in the vertical direction can be expressed by

$$D_z = 0.067u_*h \quad (3.3)$$

In the present study, mixing due to transverse diffusion is of particular interest, because it plays an important role in terms of longitudinal dispersion. As it is impossible to determine a standard velocity profile in transverse direction of a river, we cannot determine

an analytical value for D_y such as in the case of vertical mixing. Fischer et al. (1979) presented results from field and laboratory experiments in uniform channels, where the transverse diffusion coefficient was determined to be on average

$$D_y = 0.15u_*h \quad (3.4)$$

within an accuracy of $\pm 50\%$. It is remarkable that the channel width is not a parameter of equation 3.4. The problem is, that in uniform wide channels, the width B does not correspond with the size of the largest eddies in horizontal direction. In uniform channels or in laboratory flumes the size of the horizontal eddies are determined by the width of the boundary layer at the channel banks which is in the order of 3-5 water depths. In rivers the B/h ratio is much higher and therefore not confining the eddy size as it is confined by h in the case of vertical mixing.

In natural rivers the mixing in transverse direction frequently is influenced by the presence of large, coherent, lateral motions, which are generated by irregularities of the river morphology. Such structures are also found in the mixing layer between groin fields and the main stream in rivers. In addition, secondary currents, due to the curvature of the river, can have a strong influence on transverse mixing. Fischer et al. (1979) proposed the following relation to describe transverse diffusion in natural rivers

$$D_y = 0.6u_*h \quad (3.5)$$

The constant 0.6 represents the mean value of a range that lies typically between 0.4 and 0.8.

It has to be noticed, that turbulent diffusion in horizontal direction need not be constant over the channel width. Assuming a flow field which is typical for rivers with groin fields we can divide the river in transverse direction into three typical regions of different diffusion characteristics.

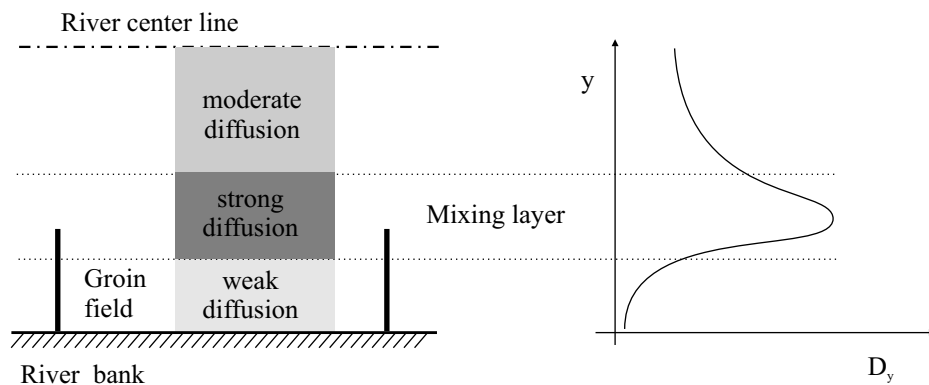


Figure 3.1. Characteristic regions of different diffusivity and the expected distribution of the diffusivity in transverse direction

In the mid channel section which is characterized by "moderate diffusion" (Fig. 3.1) D_y can be determined using equation (3.4). In the mixing layer the transverse diffusion is amplified by velocity fluctuations in transverse direction due to the presence of the large coherent structures. In the groin fields the turbulent diffusion is very weak because the

velocities are much lower than in the main stream. Therefore, the turbulent diffusion here is overestimated using equation 3.4. The shear velocity u_* defined for the main channel does not adequately describe the characteristic velocity of the turbulent flow in the mixing layer and the groin field. The strength of the velocity fluctuations can be expressed using the Root-Mean-Square-Velocity v' which is defined as

$$v' = \sqrt{\overline{v'v'}} \quad (3.6)$$

If we assume that the turbulent diffusivity is proportional to the the transverse velocity fluctuations, D_y can be obtained by multiplying D_y with $v'(y)$ which is normalized with v'_C found in the channel mid section.

$$D_y(y) = 0.15hu_* \frac{v'(y)}{v'_C} \quad (3.7)$$

The result of this adaptation, is a profile of the transverse diffusivity, that is equal to the v' distribution shown in Fig. 3.1. In the main channel the resulting diffusivity is the same as obtained by 3.4; it gets amplified in the region of the mixing layer and attenuates in the region of the groin field.

In 1-dimensional transport models this differentiation is not used, because the transverse turbulent diffusion sits in the longitudinal dispersion coefficient which has to be calibrated with tracer tests. In order to quantify the effects of dead-water zones using a Lagrangian-Particle-Tracking-Method presented in section 6, where 2-dimensional information of the flow field is used, this method leads to more accurate results.

3.1.2 Advection-diffusion

Advection describes mass transport due to the mean motion of the surrounding medium. The mass flux J_x due to advection in x-direction is

$$J_x = UAC \quad (3.8)$$

where U is the mean velocity, A the area, and C the concentration. Transport processes in rivers are mainly due to the combination of advection and turbulent diffusion. The total mass flux out of advection and diffusion can be written as follows

$$J_x = uAC - D_x A \frac{\partial C}{\partial x} \quad (3.9)$$

In order to derive the governing differential equation describing the time-dependent change in concentration due to advection and diffusion we use the principle of mass conservation. The change in mass in the control volume shown in Fig. 3.2 can be described by the mass conservation law

$$\frac{\partial M}{\partial t} = \sum J_{in} - \sum J_{out} \quad (3.10)$$

Using linear Taylor series expansion to combine the two fluxes at the inflow and outflow cross-section we obtain, for example, the net flux in the x-direction

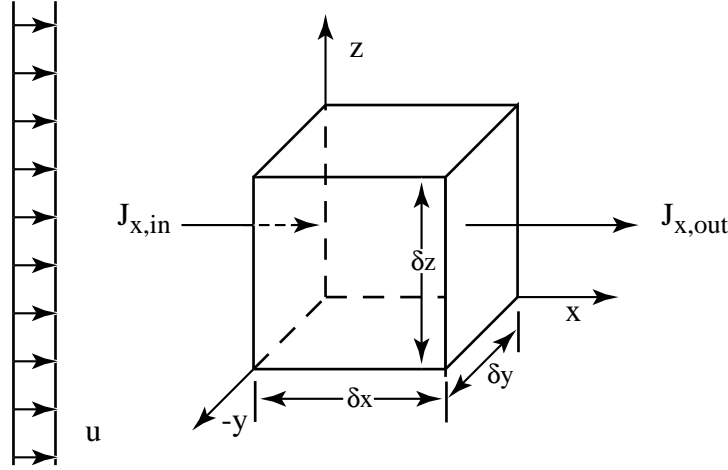


Figure 3.2. Control volume illustrating the mass flux J due to advection u in x -direction

$$\Delta J_x = -\frac{\partial(uC)}{\partial x} \delta x \delta y \delta z + D \frac{\partial^2 C}{\partial x^2} \delta x \delta y \delta z \quad (3.11)$$

By substituting (3.11) into (3.10) with $M = C \delta x \delta y \delta z$ and following this procedure for the other two components we get the 3-D-Advection-Diffusion equation for conservative tracer

$$\frac{\partial C}{\partial t} + \frac{\partial(uC)}{\partial x} + \frac{\partial(vC)}{\partial y} + \frac{\partial(wC)}{\partial z} = D_x \frac{\partial^2 C}{\partial x^2} + D_y \frac{\partial^2 C}{\partial y^2} + D_z \frac{\partial^2 C}{\partial z^2} \quad (3.12)$$

This equation describes the mass transport due to advection and diffusion in the most general case, with varying diffusion coefficients, in a three dimensional flow field. Assuming a 1-dimensional homogeneous flow field $q = (u, 0, 0)$, and no concentration gradients in y - and z -direction the equation can be written as follows

$$\frac{\partial C}{\partial t} + u \frac{\partial C}{\partial x} = D_x \frac{\partial^2 C}{\partial x^2} \quad (3.13)$$

In the case of an instantaneous plane source in a uniform flow U , this equation can be solved for C analytically leading to the known result, which represents a Gaussian distribution

$$C = \frac{m''}{\sqrt{4\pi D_x t}} \exp\left(-\frac{(x - Ut)^2}{4D_x t}\right) \quad (3.14)$$

where m'' denotes mass per unit area, distributed at a certain moment in the y - z -plane at $x = 0$. In figure 3.3 such a transport problem is visualized, showing three different Gaussian curves, determined by equation 3.14, at three different times steps. The processes acting on the tracer cloud in figure 3.3 are advection in x -direction and diffusion in longitudinal direction. Transverse diffusion does not play a role, because in this case the concentration gradients in the lateral directions are zero.

A measure of the width of a tracer cloud is given by the standard deviation σ (figure 3.3), that is proportional to the square root of the diffusion coefficient D , multiplied by the mixing time.

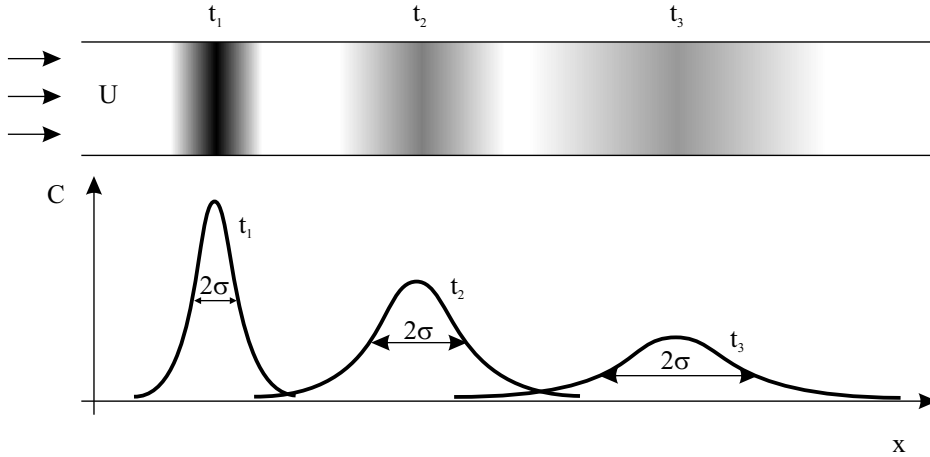


Figure 3.3. Transport of a tracer cloud in a homogeneous flow field $q = (u, 0, 0)$ due to advection and diffusion, where the tracer cloud is visualized at three different time steps

$$\sigma = \sqrt{2Dt} \quad (3.15)$$

Up to now equation 3.14 describes a transport process in a uniform and homogeneous flow field. In real systems, such as natural rivers as well as pipe flows, transport processes are also influenced by velocity profiles in the horizontal and vertical direction, if we assume no changes in the river shape in longitudinal direction. Also the diffusion coefficient is dependent on its orientation in space (section 3.1.1). Therefore, the full 3-dimensional equation should be applied (equation 3.12), in order to describe such a process sufficiently. The problem is, however, that accidental spills have to be predicted fast and easy with online operating systems, which makes it necessary to keep the equations as simple as possible. One alternative possibility is to approximate with a 1-dimensional approach the solution of the 3-dimensional ADE. This is given by the principle of longitudinal dispersion which is discussed in the following section.

3.2 Longitudinal dispersion

A tracer cloud that is well mixed over the width of a river cross-section (section 3.3) grows much faster in the longitudinal direction than it would have been expected, considering only turbulent diffusion in x-direction. The reason for that are the effects of the velocity shear in y- and z-direction. Mass travels fast in regions of high velocity that can be found in the river mid-section, and slow close to the river banks and at the river bottom. In Fig. 3.4 a scenario is visualized where tracer is uniformly distributed over the cross-section and gets distorted by the flow field.

Due to the distortion of the tracer cloud by the velocity shear, the concentration gradients in lateral direction (Fig. 3.4 ii) are amplified, which increases the mixing due to diffusion in y-direction. Taylor (1954) showed that after a certain time T_l an equilibrium gets established between the stretching rate due to velocity shear and the mixing in transverse direction due to diffusion (Fig. 3.4 iii) (section 3.2.1). If this equilibrium is

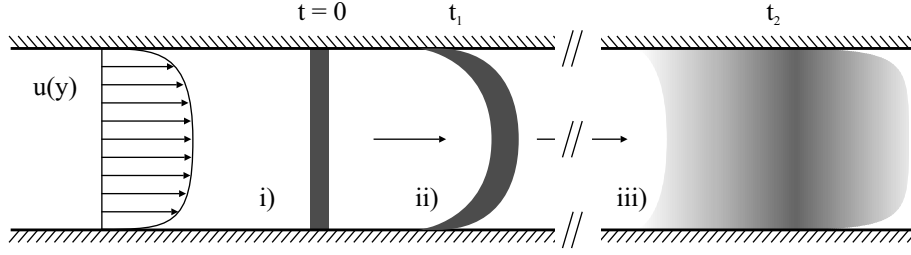


Figure 3.4. Top view on a river to visualize the stretching of a tracer cloud due to dispersion; i) initial homogeneous tracer injection; ii) tracer cloud gets deformed corresponding to the velocity distribution; iii) turbulent diffusion leads to a homogenization of the tracer cloud in transverse direction of the river

reached, the length of the tracer cloud in the longitudinal direction grows linear with time, which is again an indication for a Fickian behavior of the process. This fact allows in many cases to describe mass transport in a river as a 1-dimensional problem by an equation of the same form as equation 3.14.

In rivers, dispersion is mainly driven by the lateral velocity profile (figure 3.4) and the turbulent diffusion in the lateral direction. The transport due to dispersion in a river is the dominant process with respect to the stretching rate of a tracer cloud and the associated dilution of the tracer (section 3.3). Dispersion is of negligible importance in cases of stationary transport problems, such as continuous mass releases. Here the effect of dispersion is only visible at the moving front of a tracer cloud.

3.2.1 Taylor's approach

In the following section Taylor's analysis to determine the governing 1-D Advection-Dispersion-Equation is given as is discussed by Socolofsky & Jirka (2002). This equation is used as the basic equation to describe different transport applications that deal with dispersion problems. In a further step the analytical derivation to calculate the corresponding longitudinal dispersion coefficient is given.

The starting point of the analysis presented by Taylor (1953) is the 3-dimensional ADE, that has already been introduced in equation 3.12.

If we assume an infinitely wide channel, in which the v and w components of the flow are zero, and the concentration gradients in the lateral directions are small, which means that we talk about a laterally well mixed situation, equation 3.12 can be simplified to:

$$\frac{\partial C}{\partial t} + u \frac{\partial C}{\partial x} = D_x \frac{\partial^2 C}{\partial x^2} + D_z \frac{\partial^2 C}{\partial z^2} \quad (3.16)$$

In equation 3.16, u and C do not only depend on x , but also on z . Similar to the Reynolds decomposition, which is used to deal with fluctuating velocities, we can now insert a spatial Reynolds decomposition, where u and C are split into a spatial mean value and a deviating part (figure 3.5), that represents the velocity and the concentration distribution, respectively.

$$u(x, z) = \bar{u}(x) + u'(x, z) \quad (3.17)$$

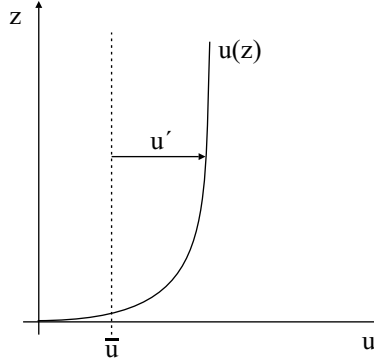


Figure 3.5. Schematic sketch of the Reynolds-Decomposition in vertical shear flow

$$C(x, z, t) = \bar{C}(x, t) + C'(x, z, t) \quad (3.18)$$

If we substitute the Reynolds decomposition for a shear flow profile into (3.16) we obtain:

$$\frac{\partial(\bar{C} + C')}{\partial t} + (\bar{u} + u') \frac{\partial(\bar{C} + C')}{\partial x} = D_x \frac{\partial^2(\bar{C} + C')}{\partial x^2} + D_z \frac{\partial^2(\bar{C} + C')}{\partial z^2}. \quad (3.19)$$

As \bar{C} is not a function of z this part of the second term on the right hand side of the equation drops out. In the next step Taylor states that the stretching of the cloud in longitudinal direction due to the vertical velocity profile is much stronger than the influence of the turbulent diffusion in x -direction allowing us to neglect the D_x term. In addition we transform this equation into a coordinate system that moves with the mean advection velocity in order to get rid of \bar{u} . The following coordinate transformation is introduced:

$$\xi = x - \bar{u}t \quad (3.20)$$

$$\tau = t \quad (3.21)$$

$$z = z, \quad (3.22)$$

By using the chain rule, the differential operators become:

$$\frac{\partial}{\partial x} = \frac{\partial \xi}{\partial x} \frac{\partial}{\partial \xi} + \frac{\partial \tau}{\partial x} \frac{\partial}{\partial \tau} = \frac{\partial}{\partial \xi} \quad (3.23)$$

$$\frac{\partial}{\partial t} = \frac{\partial \xi}{\partial t} \frac{\partial}{\partial \xi} + \frac{\partial \tau}{\partial t} \frac{\partial}{\partial \tau} = \frac{\partial}{\partial \tau} - \bar{u} \frac{\partial}{\partial \xi} \quad (3.24)$$

Substituting this transformation into (3.19) we obtain the governing equation for the concentration deviations \bar{C} with respect to time:

$$\frac{\partial(\bar{C} + C')}{\partial \tau} + u' \frac{\partial(\bar{C} + C')}{\partial \xi} = D_z \frac{\partial^2 C'}{\partial z^2}, \quad (3.25)$$

Because u' varies with z , this is still an intractable equation. The concentration and velocity deviations in vertical direction are responsible for the increased longitudinal stretching of the tracer. Therefore Taylor discards the non-fluctuating terms \bar{C} from (3.25) by applying the depth average operator $\frac{1}{h} \int_0^h dz$ which leads to a one-dimensional transport equation

$$\frac{\partial \bar{C}}{\partial \tau} + \frac{\partial \overline{u' C'}}{\partial \xi} = 0, \quad (3.26)$$

where $u' C'$ represents the additional mass transport rate due to the velocity distribution. As u' is a known function the goal is to find a relation for C' . Therefore (3.26) has to be subtracted from (3.25) which leads to

$$\frac{\partial C'}{\partial \tau} + u' \frac{\partial \bar{C}}{\partial \xi} + u' \frac{\partial C'}{\partial \xi} = \frac{\partial \overline{u' C'}}{\partial \xi} + D_z \frac{\partial^2 C'}{\partial z^2} \quad (3.27)$$

In order to simplify equation (3.27) a scale analysis can be performed. Hereby the variables get replaced by a characteristic scale, multiplied with a dimensionless coefficient. These coefficients are marked in the following with a '★'.

$$\xi = L \xi^* \quad (3.28)$$

$$z = H z^* \quad (3.29)$$

$$C' = c' C'^* \quad (3.30)$$

$$\bar{C} = \bar{c} \bar{C}^* \quad (3.31)$$

$$u' = U' u'^* \quad (3.32)$$

$$\tau = \frac{L}{\bar{U}} \tau^* \quad (3.33)$$

where $(L, H, c', \bar{c}, U', \bar{U})$ are the typical scales that describe the problem. If these expressions are inserted into equation 3.27 we get

$$\underbrace{\frac{c' L}{\bar{U}}}_{1} \frac{\partial C'^*}{\partial \tau^*} + \underbrace{\frac{U' \bar{c}}{L}}_{2} u'^* \frac{\partial \bar{C}^*}{\partial \xi^*} + \underbrace{\frac{U' c'}{L}}_{3} u'^* \frac{\partial C'^*}{\partial \xi^*} = \underbrace{\frac{U' c'}{L}}_{4} \frac{\partial \overline{u'^* C'^*}}{\partial \xi^*} + \underbrace{\frac{D_z c'}{H^2}}_{5} \frac{\partial^2 C'^*}{\partial z^{2*}} \quad (3.34)$$

If the scales $(L, H, c', \bar{c}, U', \bar{U})$ are chosen to be on the correct order of magnitude, it can be stated that all the dimensionless $\frac{\partial^*}{\partial^*}$ terms are of order one. In order to decide which terms are dominating the equation and which terms can be neglected, the terms 1-4 in equation 3.34 have to be compared. If we divide term 2 by term 3 or 4 we get

$$\frac{\frac{U' \bar{c}}{L}}{\frac{U' c'}{L}} = \frac{\bar{c}}{c'} \gg 1 \quad (3.35)$$

which means that the terms 3 and 4 of equation equation 3.34 are negligible compared to the second term. This statement is true, because we are looking for solutions in the far-field of a tracer release, which means that the tracer mass has already been distributed over the whole cross-section. Therefore the concentration deviation c' in transverse direction is small compared to the mean concentration \bar{c} . Discarding term three and four and going back to the dimensional form we can write

$$\frac{\partial C'}{\partial \tau} + u' \frac{\partial \bar{C}}{\partial \xi} = D_z \frac{\partial^2 C'}{\partial z^2} \quad (3.36)$$

Furthermore Taylor (1954) stated, that in a far-field of a tracer transport scenario, the temporal changes reach almost a steady state, so that he also discarded the first term of equation 3.36 to get

$$u' \frac{\partial \bar{C}}{\partial \xi} = D_z \frac{\partial^2 C'}{\partial z^2} \quad (3.37)$$

The first term of equation 3.37 is an advection term with the mean concentration \bar{C} that gets distorted by the velocity deviation u' , due to the shear profile of the flow field. In other words, this term describes the stretching of a tracer cloud due to a given velocity profile. The term on the right hand side is a diffusion term that acts in the transverse direction to the mean flow. Equation 3.37 describes, therefore, a balance between stretching of the tracer in longitudinal direction and homogenization due to diffusion in transverse direction.

In order to solve equation 3.37 for C' we have to integrate this expression twice, using the boundary condition $\partial \bar{C} / \partial z = 0$ at $z = 0$ and $z = h$

$$C' = \frac{1}{D_z} \frac{\partial \bar{C}}{\partial \xi} \int_0^z \int_0^z u' dz dz \quad (3.38)$$

Relative to the moving coordinate system, the mass transport rate in longitudinal direction can be written as

$$q_\xi = \frac{1}{h} \int_0^h u' C' dh \quad (3.39)$$

If C' is substituted by the result from equation 3.38 we get

$$q_\xi = \frac{1}{h} \frac{1}{D_z} \frac{\partial \bar{C}}{\partial \xi} \int_0^h u' \int_0^z \int_0^z u' dz dz dz \quad (3.40)$$

Assuming a uniform flow field, it can be stated that the mass flux q_ξ is proportional to the concentration gradient in longitudinal direction. That indicates that the cross-sectional integrated spreading, due to velocity shear and transverse diffusion, is a Fickian type of transport process. Analogous to molecular or turbulent diffusion it can be written

$$q_\xi = -D_L \frac{\partial \bar{C}}{\partial \xi} \quad (3.41)$$

where D_L stands for the following triple integral

$$D_L = \frac{-1}{h} \frac{1}{D_z} \int_0^h u' \int_0^z \int_0^z u' dz dz dz \quad (3.42)$$

what is called the longitudinal dispersion coefficient, which plays the same role for the whole cross-section as the turbulent diffusion coefficient on a turbulent length scale. From equation 3.42 it can be seen that the longitudinal dispersion coefficient can be determined analytically, if the diffusion coefficient in transverse direction and the velocity distribution are known. Inserting equation 3.41 into equation 3.26 gives

$$\frac{\partial \bar{C}}{\partial \tau} = D_L \frac{\partial^2 \bar{C}}{\partial \xi^2} \quad (3.43)$$

By replacing the moving axis by the Eulerian coordinates, the following one-dimensional Advection-Dispersion-Equation ADE of the already known form is reached

$$\frac{\partial \bar{C}}{\partial t} + \bar{u} \frac{\partial \bar{C}}{\partial x} = D_L \frac{\partial^2 \bar{C}}{\partial x^2} \quad (3.44)$$

A solution to this equation, representing a Gaussian curve in the case of an instantaneous point source in a homogeneous channel, is already given in equation 3.14. Herewith Taylor (1954) showed, that in the case of homogeneous flow conditions, where the mass is fully mixed over cross-section of the flow, the mass transport can be modelled using the 1-dimensional advection diffusion equation, regardless whether the flow is laminar or turbulent.

3.2.2 Application of Taylor's approach

Taylor's theory of 1-dimensional dispersive transport has been applied to several different types of flow. Fischer et al. (1979) applied this theory for laminar shear flow between two parallel plates of infinite extent, where the top plate moves with velocity U compared to the bottom plate (Fig. 3.6), so that the velocity distribution is

$$u(y) = U \frac{y}{h} \quad (3.45)$$

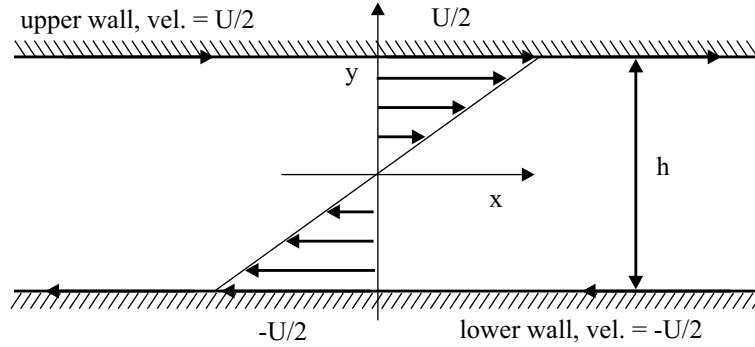


Figure 3.6. Laminar velocity distribution

The diffusion coefficient D_y in transverse direction is constant over the whole width of the flow. As an example, the derivation of this solution is shown, starting from equation 3.37 where Taylor (1953) showed that the dispersion of mass in the far-field of a release point is determined by the equilibrium of longitudinal stretching and transverse diffusion.

Inserting the velocity profile given in 3.45 into the solution of 3.37, which was given by 3.38, we get an expression for the concentration deviation C' in y -direction

$$C'(y) = \frac{1}{D_y} \frac{\partial \bar{C}}{\partial x} \int_{-h/2}^y \int_{-h/2}^y \frac{Uy}{h} dy dy + C'(-h/2) \quad (3.46)$$

$$= \frac{1}{D_y} \frac{\partial \bar{C}}{\partial x} \frac{U}{2h} \left(\frac{y^3}{3} - \frac{h^2 y}{4} - \frac{h^3}{12} \right) + C'(-h/2) \quad (3.47)$$

In the moving coordinate system the rate of mass \dot{m} , which is transported in longitudinal direction, is given by $\dot{m} = \frac{1}{h} \int u' C' dy$. If we insert the expression for C' from 3.47, we get

an expression in which the mass flux \dot{m} is proportional to the cross-sectional averaged concentration gradient in the longitudinal direction. The constant of proportionality is the longitudinal dispersion coefficient E_L and in this case given by

$$D_L = -\frac{U}{2h^2 D_y} \left(\int_{-h/2}^{h/2} \frac{Uy}{h} \left(\frac{y^3}{3} - \frac{h^2 y}{4} - \frac{h^3}{12} \right) dy + \int_{-h/2}^{h/2} C'(-h/2) dy \right) \quad (3.48)$$

Because C' is expected to be symmetric to the origin of the coordinate system, positive for $y > 0$ and negative for $y < 0$, the second integral in Eq. (3.48) becomes zero. The first integral leads to the result presented by (Fischer et al. 1979)

$$D_L = \frac{U^2 h^2}{120 D_y} \quad (3.49)$$

In the case of laminar pipe flow Taylor (1953) determined the longitudinal dispersion coefficient D_L to be

$$D_L = \frac{D^2 u_{max}}{192 D_y} \quad (3.50)$$

With the aid of laboratory experiments Taylor (1954) proved that his theory also leads to good results in the case of turbulent pipe flow. Using an empirical velocity distribution (Taylor 1954), the dispersion coefficient can be determined in that case by

$$D_L = 10.1 r u_* \quad (3.51)$$

where r is the pipe radius.

A first attempt to apply Taylor's theory to open channel flow was done by Elder (1959). In this work the dispersion coefficient was determined under the assumption of an infinite wide open channel with a logarithmic velocity profile over the water depth

$$u(z) = -\frac{1}{\kappa} \ln(1 - z) \quad (3.52)$$

where the Karman constant κ is 0.41 and a parabolic distribution of the vertical turbulent diffusion coefficient in analogy to the distribution of the eddy diffusivity

$$D_z = \kappa z \frac{1 - z}{h} \quad (3.53)$$

Solving the triple integral presented in equation 3.42 Elder (1959) came up with the following result

$$D_L = 5.86 u_* h \quad (3.54)$$

Elder (1959) validated his result also with experiments, in which he used a shallow water table with a water depth of 1 cm, in order to approximate an infinitely wide open channel. In section 3.3.2 it is shown why Elder's theory underestimates strongly the dispersive character of natural rivers.

3.3 Mass transport in rivers

Mass transport in natural rivers is much more complicated than mass transport in pipe flow, as has been described by Taylor (1954). In rivers the morphologic conditions are changing in the stream-wise direction, which means that the width, depth are not a constant. Reaches with groins are followed by reaches without groins, strongly meandering reaches are followed by rather straight sections. Therefore, different approaches were developed in order to apply Taylor's approach to natural rivers. An important assumption in order to apply the concept of the ADE is that the mass has to be well mixed over the entire river cross-section. This is discussed in the next section, when fully mixed conditions can be assumed, followed by the description of different approaches to quantify dispersion in natural rivers.

3.3.1 The advective zone

Longitudinal dispersion, as is discussed in the previous section, takes place if the tracer mass is distributed completely over the the river cross-section, which means that the standard deviation σ_y of the tracer cloud is much bigger than the river width. Depending on the initial conditions of the tracer injection, it can take a long time until well-mixed conditions are obtained, which is the precondition to apply a 1-dimensional mass-transport model. Following a tracer cloud from the source until it is spread over the entire cross-section of a river, three stages of mixing (Sullivan 1971) can be distinguished (figure 3.7):

- A) In the **near-field**, mixing is dominated by buoyancy and momentum forces that are determined by the effluent. Transport phenomena in the near-field have to be treated as 3-dimensional problems.
- B) In the **mid-field**, the tracer mass is already mixed over the river depth. Momentum and buoyancy forces are in most cases negligible. Transport phenomena in the mid-field can be treated as depth-averaged 2-dimensional problems. The sum of near-field and the mid-field is also known as the **advective zone**
- C) In the **far-field** the tracer mass has expanded over the entire river cross-section. Transport phenomena in the far-field are often treated as cross-sectional averaged 1-dimensional problems. The skewness of the tracer distribution in the longitudinal direction vanishes slowly.

Because the main focus of the present work is to analyze the influence of dead-water zones on the transport in the far-field it has to be determined when the far-field is reached. In section 3.1.2 it has been shown, that the standard deviation of a tracer cloud can be used as a measure of the width of a tracer cloud and that σ is equal to $\sqrt{2Dt}$. If we replace t by x/U , and σ by some characteristic length (should be related to the river width B), we can calculate the length of the advective zone L_x that determines the beginning of the far-field as follows

$$L_{xm} = \alpha \frac{B^2 U}{D_y}. \quad (3.55)$$

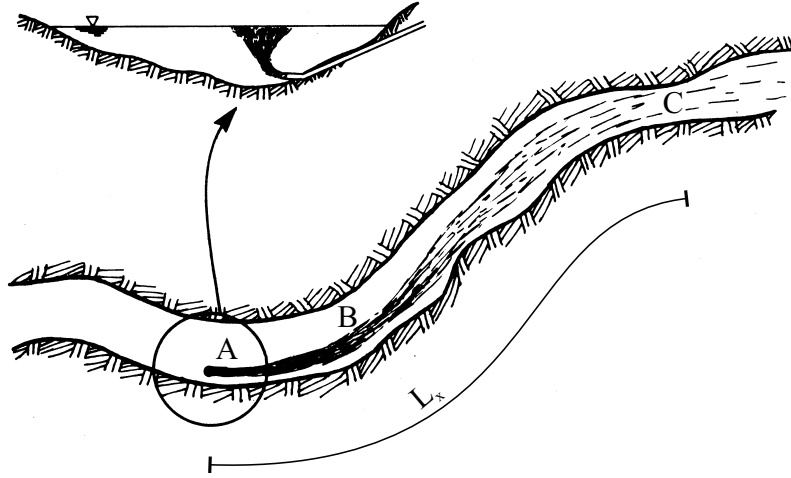


Figure 3.7. Visualization of the three different stages of mixing in a natural river and definition of the advective length L_x ; A) active mixing due to momentum and buoyancy forces in the near-field, B) turbulent diffusion in transverse direction in the mid-field, C) tracer is distributed over the river cross-section in the far-field; adapted from Fischer et al. (1979)

In the case of a mass release in the middle of the river σ is set to $B/2$, which gives $\alpha = 0.125$. If the mass gets released at the river bank where σ is equal to B , α can be determined to be 0.5.

These values for α can also be found by Fischer et al. (1979) and by Rutherford (1994). A significant increase of L_x has been observed in experiments in the presence of dead-water zones. Numerical experiments performed by Denton (1990), where dead-water zones covered 5% of the river volume showed that α should be of order 1.4. Valentine & Wood (1979) presented experiments in irrigation channels where the dead-water zones covered a much larger part of the river cross-section. In the case of 30% dead-water zones α was determined to be up to 10.

In table 3.1 the length of the advective zone L_x is calculated for two different sizes of rivers. In these examples the turbulent diffusivity is calculated using equation 3.5, and the shear velocity u_* is approximated with 10% of the mean velocity.

Table 3.1. Theoretical length of the advective zone, before well mixed conditions are established. D_y is determined by equation 3.5 and u_* is estimated to be to be 10% of the mean velocity; $L_{x,S}$ represents the case where the mass has been released in the center of the river and in the case of $L_{x,B}$ the mass has been released at the river bank; $L_{x,D}$ represents the case presented by Valentine & Wood (1979) including the effect of dead-zones

	Width [m]	Mean Velocity [m/s]	Water depth [m]	$L_{x,S}$ [km]	$L_{x,B}$ [km]	$L_{x,D}$ [km]
Case 1	100	2	2	10	41	833
Case 2	10	1.5	0.5	0.4	1.6	33

The result from table 3.1 is, that the application of 1-dimensional models for calculating tracer concentrations in natural rivers has to be reviewed very carefully.

If we consider Taylor's 1-dimensional approach (equation 3.14) another problem arises by the fact that the solution to this equation is always a symmetric Gaussian curve. Field experiments showed (Fischer et al. 1979, Rutherford 1994) that the cross-sectional averaged concentration distribution of tracer spills in the mid- and far-field are always strongly skewed, with a rising limb that is much shorter than the falling limb. Taylor (1953) showed (section 3.2.1) that the skewness decreases if the balance between longitudinal stretching and transverse diffusion is established, which is certainly not achieved before a tracer cloud is well mixed over the river cross-section. In channels with strong morphological changes this equilibrium cannot be reached because it is determined by the morphological conditions. This means that changes in the river geometry can cause a shift from strong transverse diffusion to strong longitudinal stretching or vice versa. According to Fischer et al. (1979), a Gaussian approximation can be applied at $x = 2.5L_x$ (values up to $x > 50L_x$ can be found in literature). Thus, in order to apply Taylor's theory with a certain accuracy the values given in table 3.1 have to be multiplied by a factor of 2.5. However, no drastic changes in the morphologic conditions of the river have to be assumed in order to reach a Gaussian concentration distribution (section 3.4.1). A more detailed discussion about the influence of dead-water zones on the length of the advective zone is given in 6.4.

3.3.2 Dispersion coefficients in rivers

Rutherford (1994) presented a large collection of field data that leads to the conclusion that the longitudinal dispersion coefficient in the far-field of a transport problem in natural rivers falls within the range of

$$30 < \frac{D_L}{u_* h} < 3000. \quad (3.56)$$

This shows clearly that Elder's approach (section 3.2.2) strongly underestimates the dispersive character of natural streams. The reason for this can be seen as the shallowness of a river. Typically, the width to depth ratio lies between 10 and 100. Fischer et al. (1979) showed, using scale analysis, that D_L is proportional to the square of the channel width, which means that dispersive effects due to the transverse velocity distribution should be at least 100 times bigger than due to the vertical velocity profile (which was used in the Elder's case). Therefore Fischer et al. (1979) reformulated Taylor's triple integral (3.42) in such way that u' denotes the velocity deviation in the horizontal direction

$$D_L = -\frac{1}{A} \int_0^B u' d \int_0^y \frac{1}{D_y h} \int_0^y u' h dy dy dy \quad (3.57)$$

where A represents the cross-sectional area, and B the width of the channel. The difference between equation 3.42 and equation 3.57 given here is that h is now a variable dependent on the y -position, which means that also the influence of a variable water depth is taken into account. With the help of this equation dispersion coefficients in rivers can be predicted analytically, if the velocity distribution in lateral direction and the transverse diffusivity are known. Equation 3.57 is only applicable if the morphologic conditions

do not vary strongly in longitudinal direction, which means that equation 3.57 is still restricted to regular channels.

Fischer et al. (1979) developed a simple equation by introducing two non-dimensional parameters into equation 3.42, which represent the shape of the velocity deviation in transverse direction. With the help of field and laboratory measurements, Fischer et al. (1979) determined typical values for these parameters, which leads to

$$D_L = 0.011 \frac{B^2 U^2}{u_* h} \quad (3.58)$$

where U is the mean flow velocity in x-direction and h the mean flow depth. Herein the coefficient of turbulent diffusion in transverse direction is determined by equation 3.5. Comparison with tracer tests showed that equation 3.58 is accurate within a factor of four. Fischer et al. (1979) stated that it is not possible to take into account explicitly the effects of dead-zones with this simplification.

Seo & Cheong (1998) tried to improve Fischer's 1-D approach by transforming equation 3.58 into

$$\frac{D_L}{hu_*} = \alpha \left(\frac{U}{u_*} \right)^a \left(\frac{B}{h} \right)^b \quad (3.59)$$

In a further step they adapted the parameters α , a and b using a fitting routine in such way that the predicted D_L -values give the best results compared with data sets from different field measurements. Best results were obtained with $\alpha = 5.915$, $a = 0.620$ and $b = 1.428$. They stated, that this equation is valid with an accuracy of 79%.

Deng et al. (2001) presented an extension of Fischer's approach by introducing the channel sinuosity which leads to reformulated triple integrals that are solved analytically, using regression equations for different width to depth ratios and sinuosity. Comparison with data from 70 different tracer tests showed again an improvement compared to the approach presented by Seo & Cheong (1998).

All these approaches can be used to predict roughly dispersion coefficients in the far-field of a tracer transport problem with a certain accuracy, to determine concentration profiles with the given solution of the ADE. The problem of modeling transport phenomena with the ADE is, that in terms of dead-water zones this equation does not represent the physical behavior of the flow, which means that in the presence of dead-water zones the accuracy of these approaches can be strongly reduced.

3.4 Alternatives to the advection diffusion equation

As has been stated in the previous sections, observed tracer concentrations from instantaneous pollutant spills in many cases are not satisfactorily described with the ADE presented by Taylor (1954). Two main discrepancies between observed and calculated concentration distributions can be described (figure 3.8):

- 1) Field measurements showed that even in the theoretical far-field of a transport problem the concentration distributions in longitudinal direction are skewed in most cases (Sukhodolov 1998, van Mazijk 2002), which means that a breakthrough curve somewhere downstream of a pollutant source shows a sharp front and a long tailing (figure 3.8).
- 2) In natural rivers the travel time of the pollutant is always somewhat smaller than the mean velocity of the river. This phenomenon can be explained by the interaction between main stream and dead-water zone, which leads to a retention of the dissolved material.

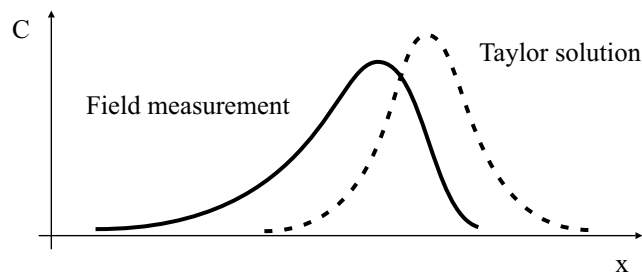


Figure 3.8. Schematic sketch of a typical longitudinal concentration profile compared to the Gaussian concentration profile according to Taylor's 1-dimensional solution

One reason for the skewness in measured concentration profiles is the fact that they are commonly temporal rather than spatial measurements, which means that a tracer cloud that passes a measurement station is stretched during its passage at this point. Direct comparison with the given solutions of the ADE would require spatial measurements. In the work of Thackston & Schnelle (1970) it has been stated that this does not account for all the skewness in the measurements. Taylor (1953) and Elder (1959) explained these differences in their experiments with the existence of a viscous sub-layer. Fischer (1966) stated that in rivers these effects can arise also due to dead-water zones at the river banks. One possibility to describe the transport of dissolved material in natural rivers is given by the so called Dead-Zone-Model, which is described in the next section.

3.4.1 Dead-zone-model

The idea of the so called Dead-Zone-Model (DZM) is to describe the cross-section of a river by two distinct zones: main stream, and dead-zone (Hays et al. 1966). In the case of a river with groin fields the separation between main stream and dead-zone is given by a stream line leading from groin head to groin head (figure 3.9). In the main stream the mass transport is dominated by advection in longitudinal direction, longitudinal shear due to the velocity distribution and lateral turbulent diffusion. Thus, the transport in the main stream under well mixed conditions should be adequately described with the 1-dimensional Taylor model. In the dead-water zone the mean velocity in main flow direction is essentially zero, which means that the only important transport mechanism in the dead-water zone is lateral turbulent diffusion.

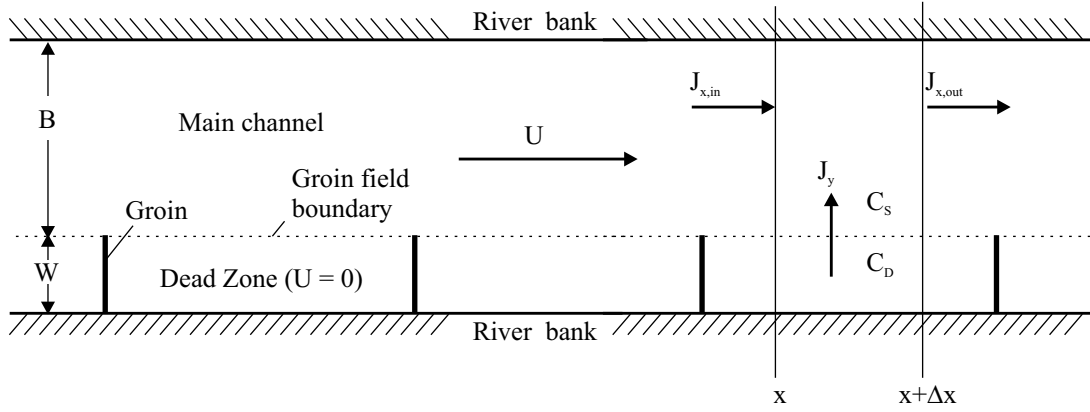


Figure 3.9. Schematic top view on a river where the two regions main channel and dead-zone are illustrated. In order to derive the associated equations by performing a mass balance, the corresponding mass fluxes in the 1-dimensional case are shown

In order to specify the mass transport across the interface between dead-water zone and main channel, Hays et al. (1966) assumed uniform concentrations in the dead-water zone. This assumption allows to postulate that the mass transport across the the interface is proportional to the difference of the averaged concentration in the dead-water zone and the main channel.

The corresponding equations can be obtained by performing a mass balance (figure 3.9)

$$\frac{\partial M}{\partial t} = \sum J_{x,in} - \sum J_{x,out} + J_y \quad (3.60)$$

Analogous to the mass balance described in section 3.1.2 the difference between J_{in} and J_{out} leads to

$$\Delta J_x = -U \frac{\partial C}{\partial x} B h_S \Delta x + D_L \frac{\partial^2 C}{\partial x^2} B h_S \Delta x \quad (3.61)$$

that includes mass transport due to diffusion and advection.

In the case of the fully mixed assumption of the dead-water zone, the mass flux J_y , due to mass exchange between the dead-water zone and the main channel, can be defined as an exchange velocity E , multiplied with concentration difference between dead-zone and main stream, multiplied with the contact area $h \Delta x$ (figure 3.10).

$$J_y = E(C_D - C_S) h_E \Delta x \quad (3.62)$$

If we substitute equation 3.61 and equation 3.62 into equation 3.60, recalling that the mass M can be expressed as $M = C B h_S \Delta x$, we get

$$\frac{\partial C_S}{\partial t} = -U \frac{\partial C_S}{\partial x} + D_L \frac{\partial^2 C_S}{\partial x^2} + \frac{h_E E}{h_S B} (C_D - C_S) \quad (3.63)$$

Thus, equation 3.63 describes the mass transport in the main channel analogous to the 1-dimensional advection-diffusion equation given in equation 3.44, extended by an exchange term $(h_E E)/(h_S B)(C_D - C_S)$.

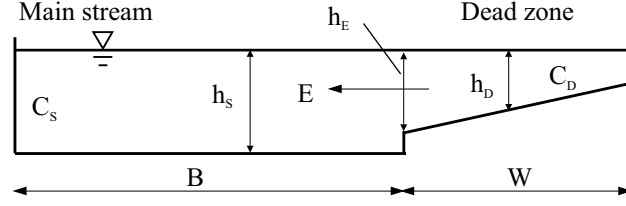


Figure 3.10. Schematic side view of a river where the two regions: main channel and dead-zone are illustrated

A second equation is needed now to describe the concentration in the dead-water zone. The mass balance in this case leads to

$$\frac{\partial C_D}{\partial t} = -\frac{h_E E}{h_D W} (C_D - C_S) \quad (3.64)$$

with W = width of the dead-water zone. Usually $(h_E E)/(h_D W)$ and $(h_E E)/(h_S B)$ are called *exchange coefficients* and have the units $[1/s]$. The two exchange coefficients are defined as

$$\frac{h_E E}{h_S B} = K_S \quad (3.65)$$

$$\frac{h_E E}{h_D W} = K_D \quad (3.66)$$

Out of these equations different parameter groups can be formed, describing different physical meanings of such a dead-zone transport problem. One important parameter describes the average residence time T_D of a particle entering the dead-zone. T_D can be approximated by calculating the period needed for a complete exchange of all the water in the dead-water zone. This can be done by dividing the the volume of the dead-water zone by the exchange velocity and the contact area (Thackston & Schnelle 1970)

$$T_D = \frac{W h_D \Delta x}{E h_E \Delta x} = \frac{1}{K_D} \quad (3.67)$$

The average residence time T_D can also be explained by solving equation 3.64 for the case of a instantaneous and homogeneous mass release into the dead-water zone, while the concentration in the main stream is zero (figure 3.11 a). In that case the concentration in the dead-zone is described by

$$C(t) = C_o e^{(-K_D t)} \quad (3.68)$$

with C_o = the initial concentration in the dead-water zone at the moment of the tracer injection (figure 3.11).

In this case the mass exchange between dead-water zone and main stream is described by the initial slope of the exponential function in figure 3.11 b. The initial slope in equation 3.68 is given by K_D , which means that again $T_D = 1/K_D$. Experiments are described in chapter 5 where the average residence time T_D and the exchange velocity E has been measured directly and independently for different dead-zone geometries.

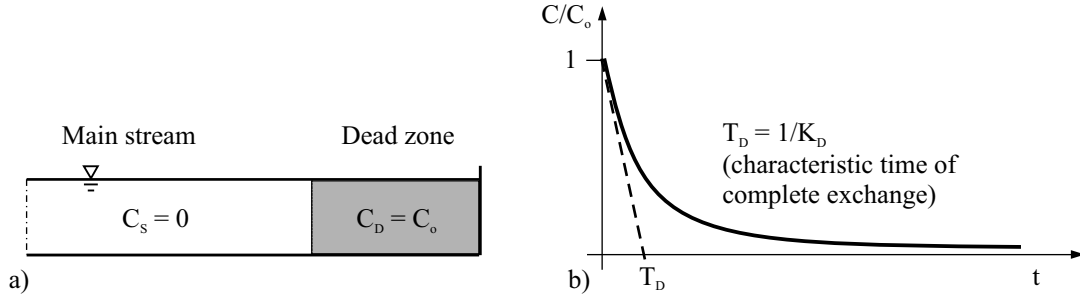


Figure 3.11. a) visualization of the initial conditions in the case of a instantaneous volume source in the dead-zone leading to the unit impulse response showed in b) with the exponential concentration decay in the dead-water zone due to exchange processes

Another important parameter that has to be analyzed in terms of the dead-zone model, is the mean transport velocity, defined as the propagation velocity of the center of mass of a tracer cloud. As mentioned before (figure 3.8) it can be stated that in transport processes in natural rivers the actual transport velocity c is somewhat smaller than the mean flow velocity U . This effect can be explained by the retention of mass in the dead-water zone, where the mean flow velocity U is zero. In the case of the Dead-Zone-Model the transport velocity c can be determined by a weighted average

$$c = \frac{M_S U + M_D U_D}{M_S + M_D} \quad (3.69)$$

with:

- M_S = tracer mass in main stream
- M_D = tracer mass in the dead-zone
- U = velocity in the main stream
- U_D = velocity in the dead-zone

Because the mean velocity in the dead-zone U_D is zero and M_S and M_D can be determined by $M_S = h_S B \Delta x C_S$ and $M_D = h_D W \Delta x C_D$, the transport velocity is given by

$$c = \frac{U}{1 + \frac{h_D W C_D}{h_S B C_S}} = \frac{U}{1 + \beta} \quad (3.70)$$

Thus, the transport velocity of a tracer cloud in the far-field is determined by the ratio between the cross-sectional area of the dead-water zone and the main channel, and the ratio between the concentrations in the main stream and the dead-zone.

If we assume that the concentration in the dead-water zone and in the main stream are equal, the parameter β reduces to the ratio between the cross-sectional areas between main channel and dead-zone. van Mazijk (1996) called β in that case the *dead-zone-parameter*. In section *LPTM* it is discussed in detail when this assumption of equal concentrations can be made.

The influence of the dead-zone concept on the skewness of the concentration distribution has been examined by Schmid (1995), who analyzed the dead-zone model numerically, including a first order decay. He showed that the evolution of the skewness in principle

does not differ from the evolution in the Taylor model. It could be shown that the skewness also tends to zero (figure 3.12 a) after a very long travel time, depending also on the delay parameter β (figure 3.12 b) and the residence time T_D (figure 3.12 c).

In section 6.4 these results are compared with the results that were obtained using the *Lagrangian-Particle-Tracking-Method* that has been developed during this study.

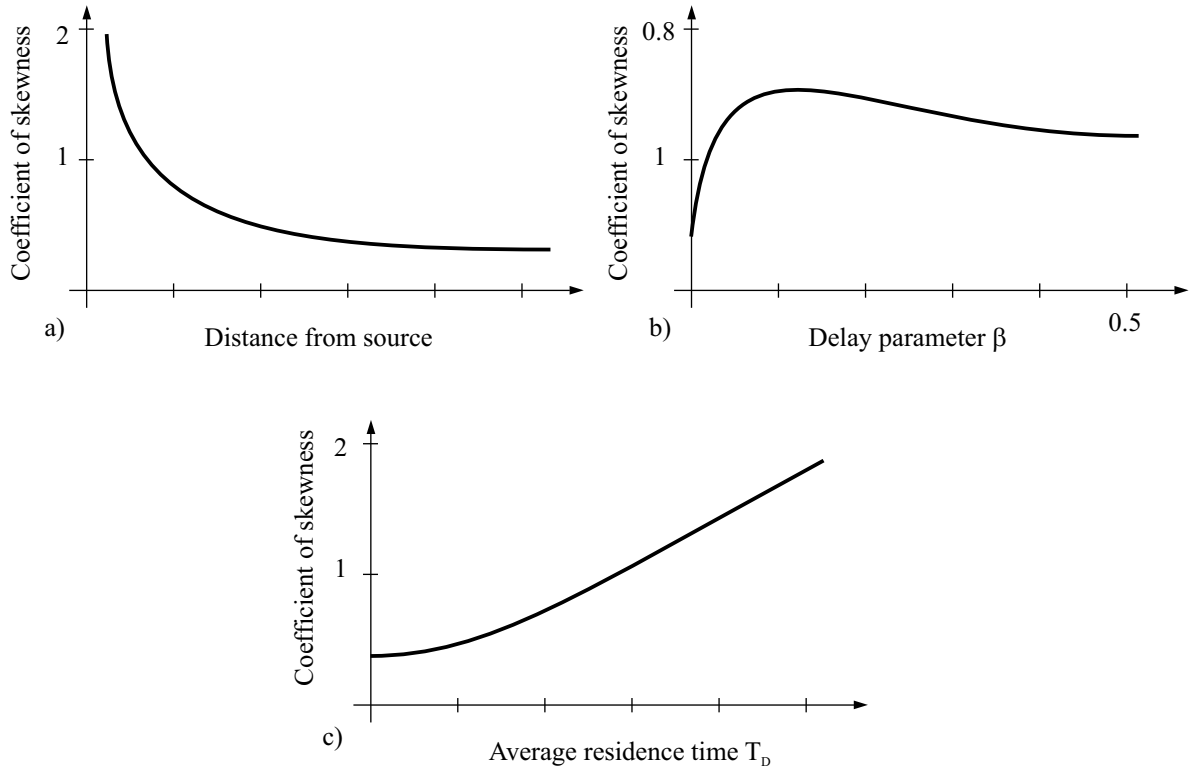


Figure 3.12. a) evolution of the skewness in dependence of the distance from the source; b) skewness in dependence of the ratio between cross-sectional area of the dead-zone and the main stream expressed by β ; exponential concentration decrease in the dead-water zone due to exchange processes; taken from Schmid (1995)

In the previous paragraphs it turned out that the key parameter of the dead-zone model is given by K_D . It controls the transport velocity and has a major influence on the skewness of a tracer cloud. In terms of the Taylor model without the dead-zone, K_D has also a strong influence on the dispersion coefficient. Long residence times in the groin fields lead to small K_D values. Long residence times also mean, that the stretching of the tracer cloud is stronger, which corresponds to a higher dispersion coefficient, if the process would have been described by the Taylor model (Aris 1959). Thus, the exchange coefficient K_D has to be very well known in order to predict the evolution of a pollutant spill, using the dead-zone-model. Valentine & Wood (1979) analyzed the non-dimensional form of K_D

$$k = \frac{WK_D}{U} = \frac{W}{T_D U} = \frac{E h_E}{U h_D} \quad (3.71)$$

and with the help of field data showed that k lies within the range of 0.01 - 0.03. No information was given about the influence of the shape of the dead-zones on k . Laboratory experiments by Lehmann (1999) and field experiments by Sukhodolov et al. (2002) verified these results. If k were a constant it could be stated that in case of groin field, the mass exchange would be the same, if the ratio between cross-sectional area of the main stream and the dead-zone does not change. In that sense the length of the groin field does not play any role, which is in contrary to the results of this study (section 5.1.7).

An application of the dead-zone-model can be found in the *Rhine-Alarm-Model* which has been developed by Spreafico & van Mazijk (1993) in order to predict online the transport of pollutant clouds in case of accidental spills. van Mazijk (2002) developed the following approximation for the of concentration distributions

$$C(x, t) = \frac{M/Q}{\sqrt{4\pi D_L t/c^2}} \exp\left(-\frac{t-x/c^2}{4D_L t/c^2}\right) \left[1 + \frac{1}{6} H_3\left(\frac{t-x/c}{\sqrt{2D_L t/c^2}}\right)\right] \quad (3.72)$$

with: M = tracer mass
 Q = flow rate
 c = transport velocity
 H_3 = third Hermite-polynomial; $H_3 = \tau^3 - 3\tau$

The basic equation in this case has been developed by Chatwin (1980), representing an approximation of the advection-diffusion-equation, taking into account the skewness of the concentration distribution with the help of the Hermite-polynomial. In addition, analytical solutions of the dead-zone-model (equation 3.63 and 3.64) were used, describing the first and the second moment of the concentration distribution determined by Valentine & Wood (1979). An important assumption made by van Mazijk (1996), is that the coefficient of skewness can be approximated by the factor one, which was proven by different field experiments in the River Rhine (van Mazijk 2002).

3.4.2 Lagrangian-Particle-Tracking-Method

Lagrangian-Particle-Tracking-Methods (LPTM) or random walk models (Sullivan 1971) represent another alternative to simulate transport problems. The principle of these models is to track numerically a large number of particles that move through a virtual representation of a flow field. In every time step the particles follow an advective motion due to the mean flow field and a random component representing diffusion. These models are computationally very simple compared to numerical solutions of the ADE and the DZM. Much research has been performed to establish solid and robust methods to solve the ADE numerically correct (Abbott & Basco 1989) in an Eulerian coordinate scheme. The problem of numerical diffusion and grid-scale oscillations within numerical solutions of the ADE remain.

LPTM models do not have the problem of numerical diffusion and computational instabilities. The accuracy of these models is mainly determined by the number of particle. As

input parameters random walk models need mean velocity fields and diffusion coefficients. In addition to the simple implementation of a random walk model, this approach has the advantage of simulating directly the physical processes, such that the interpretation of the results is very clear. In section 6 this approach is discussed in detail.

4. Experimental Studies

In this chapter, laboratory experiments are described that have been performed for studying the flow patterns and local mass transport characteristics in the presence of groin fields. The idea of these experiments is to measure local phenomena of flow and transport characteristics that can be used in a further step (chapter 6) to determine mass transport characteristics in the far-field of a transport scenario. This extra step is needed because it is not possible in this case to measure directly transport characteristics like dispersion coefficients or transport velocity, due to the limited length of the experimental facility. The problem is that the transport characteristics are changing with the distance to the tracer source (section 3.3.1) and reach their final behavior after a very long travel time that is coupled to the time needed for the tracer to be fully mixed over the channel width. Especially in cases where the lateral extent of the flow is large compared to the water depth, which is typical for river flows, the initial region of mixing is very long.

The experiments cover flow visualizations, velocity and concentration measurements. Flow visualizations are necessary for the understanding of the flow phenomena, and are needed for the preparation of quantitative measurements to assure that the important flow properties are covered. Velocity measurements have been performed, using planar and point measurement techniques to determine mean and turbulent flow characteristics. A surface PIV system has been developed (section 4.2), which has also been used to determine the local mass exchange between main channel and dead-water zone. Concentration measurements have been performed, using Planar-Concentration-Analysis (PCA) to determine the depth-integrated mass exchange between dead-water zone and main channel, which leads to mean residence times of mass in the dead-water zone (section 4.3).

4.1 Laboratory facilities

In the present study the experiments have been performed in a laboratory flume of 20m length and 1.8m width, which has an adjustable bottom slope. In all the experiments only half of the channel width has been modelled, which means that only on one side of the flume groins have been placed. The shape of the groins was chosen to be very simple due to the fact that earlier investigations suggest that there is no significant effect of the groin shape on the exchange processes (Lehmann 1999). Using a simple geometry leads to a small number of parameters, which allows clear understanding of the basic relations between geometry and flow or transport phenomena, respectively.

The flume bottom consists of a plastic laminate with small roughness elements < 0.2 mm. Level changes in x- and y-direction (figure 4.1) of the flume bottom are

smaller than 0.2 mm. The flume is connected to a system of a water storage tank and a constant head tank, which is supplied by three different pumps, enabling discharges up to $100\ell/s$. The discharge is controlled by an inductive-flow-meter together with an PC controlled gate valve. In the present case, only very small discharges of up to $10\ell/s$ are needed. Therefore, the gate valve is equipped with a pentagonal regulating orifice, which leads to constant discharges (changes smaller than 0.5%), even if the valve is opened only 5%.

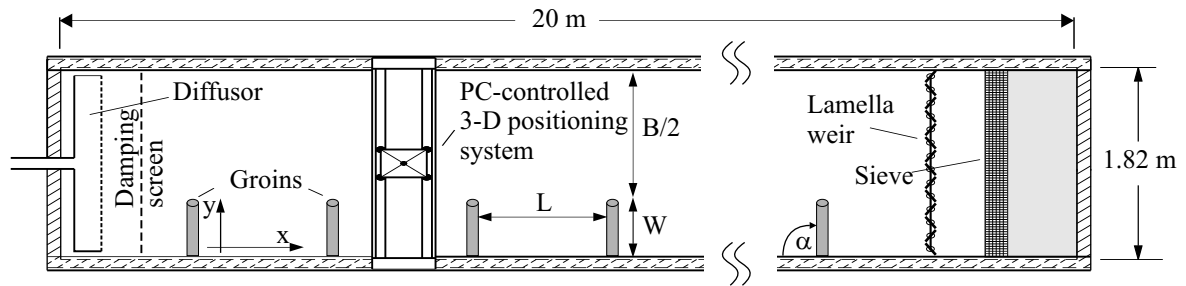


Figure 4.1. Schematic top view of the laboratory flume

The water inlet of the flume consists of a multi-port diffuser built over the complete width, followed by damping screens and a 20cm honeycomb flow stabilizer. This arrangement leads to a homogeneous flow situation without the disturbance of secondary currents that can have significant influence on the flow even after a long flow distance.

A weir at the outlet of the flume consisting of 12 vertical lamellas controls the water depth of the flow. This device combined with two ultrasonic water level meters makes sure that the water surface can be adjusted reproducibly within a range of 0.2mm.

The flume is equipped with an automatic 3-D positioning system that allows to place any kind of sensor within a volume of $2.3\text{m} \times 1.7\text{m} \times 0.6\text{m}$, with an accuracy of 0.0125mm (this accuracy was helpful for the test of the PIV system in section 4.2).

In order to simulate flow patterns under the influence of dead-water zones, respectively groin fields, a series of 15 schematized groins made of PVC with a heavy core were built, so that these elements could be placed at variable positions. The outline of a single groin was chosen to be a combination of a rectangular box ($0.45\text{m} \times 0.05\text{m} \times 0.05\text{m}$) with an attached half cylinder (diameter = 0.05m).

4.2 Measurement techniques: velocity

In shallow flow problems, such as river flows under the influence of groin fields, velocity information with high spatial and temporal resolution is needed to understand the dynamics of the flow and the related mixing processes. Large coherent motions, that are initiated in the mixing layer between groin field and main channel, strongly influence the dynamics of the system and are a determining factor for the mixing and transport processes. Due to

the fact, that these motions are mainly 2-dimensional processes in the horizontal plane, the fundamental properties can be obtained by measuring surface velocities. Because of scaling effects laboratory simulations of shallow flows always lead to measurement areas, which are in the order of meters. Therefore, a large-scale Particle-Image-Velocimetry (PIV) system has been developed that is able to track surface velocities with high spatial and temporal resolution. The flow structure in vertical direction of shallow flows can be determined using the measured surface velocities and adapting known vertical velocity profiles, such as those determined by Blasius for open-channel flow (Schlichting 1979), or for turbulent jets in shallow water (Giger, Jirka & Dracos 1991). In the present work additional Laser-Doppler-Velocimetry LDV measurements have been performed in order to determine the vertical velocity structure (section 4.2.5).

4.2.1 Surface Particle-Image-Velocimetry (PIV)

The Particle-Image-Velocimetry (PIV) technique has been developed to analyze flow fields of gaseous and liquid media. It is a powerful technique for performing 2-dimensional quantitative measurements for a large variety of flows (Adrian 1991, Raffel, Willert & Kompenhans 1998), and can also be used for the evaluation of the deformation field of a granular material (Nübel & Weitbrecht 2002). The rapid development in computer, laser, optics, electronics and video techniques was necessary to use PIV in an efficient manner.

For evaluating flow fields, digital recordings of a 2-dimensional plane of the flow have to be taken, where the flow field is seeded with appropriate tracer particles (section 4.2.2). A so called Area-Of-Interest (AOI) is cut out of the digital image and divided into small subareas, called *interrogation cells*. A local displacement vector is determined for each interrogation cell between two following digital images of a time series by means of a cross correlation of the following form

$$C_{orr}(dx, dy) = \sum_{x=0, y=0}^{x<n, y<n} Int_1(x, y) Int_2(x + dx, y + dy) \quad (4.1)$$

Hereby, I_1 and I_2 are the image intensity of the first and second interrogation cell and the 2D array C gives the correlation strength for all integer displacements (dx, dy) between the two interrogation cells, while n is the size of the interrogation cell (Raffel et al. 1998). Equation (4.1) yields a correlation distribution on the correlation plane (Fig. 4.2), where the highest peak represents the most probable displacement. Therefore, disregarding the background noise, the displacement vector for each interrogation cell is calculated by starting at the center of the cell of the first image and ending at dx, dy of the corresponding correlation peak. The result is a time series of vector fields, where the temporal and spatial resolution depend on the optical quality of the camera system, the seeding particles, the illumination and the computer power.

Many investigations have been made to improve the performance of PIV in the past by developing new correlation methods (Gui & Merzkirch 1996) or improving the image processing (Scarano & Riethmüller 1999). These efforts have led to "off the shelf" PIV packages that are easy to adapt for different applications. In the presented work PIV

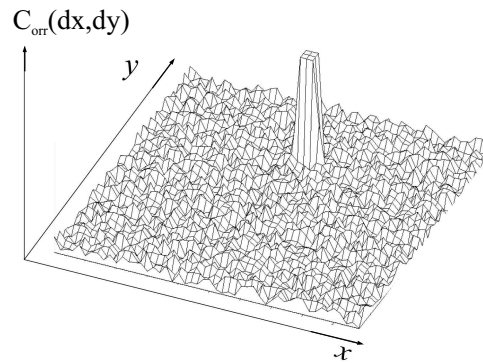


Figure 4.2. Correlation plane with correlation peak

has been used to measure velocity fields at the water surface. Compared to standard PIV applications, where measurements are carried out within the water body using laser light sheet to illuminate the measuring plane (Sheridan, Lin & Rockwell 1997, Willert & Gharib 1997, Adrian, Meinhardt & Tomkins 2000), surface PIV measurements are relatively straightforward because no laser is needed. For surface PIV measurements the measuring plane is given by the water surface, which means that for illumination standard flood lights can be used provided that the water surface is not strongly disturbed by wave motions. To keep the developed system flexible, a commercial PIV package including camera, frame grabber, controlling and evaluation software has been used, with special adaptation to the large scale laboratory problem. PIV measurements in large measuring areas have been performed in former investigations by Linden, Boubnov & Dalziel (1995) and Tarbouriech, Didelle & Renouard (1997) in rotating tanks with stratified flow conditions. In both cases the measurements have been performed using a light sheet to illuminate the measuring plane. Uijtewaal (1999) presented particle tracking measurements at the water surface where the particles were distributed manually on the water surface. In Uijtewaal & Jirka (2003) measurements can be found using the presented method, where the influence of grid turbulence on shallow flows was determined. von Carmer, Weitbrecht & Jirka (2001) used the present technique to analyze shallow wake flows.

4.2.2 Elements of the PIV system

In the following, the different parts of the developed measuring system, PIV package, camera, particles, particle dispenser, and illumination are described.

PC and software. The acquisition and analyzing system represents a standard PIV package from LaVision© including PC, PIV and control software, PIV camera, frame-grabber and programmable-timing-unit (PTU) (figure 4.3). The PTU is a PC integrated timing board that allows a precise time management for the trigger pulses needed to control camera and illumination, like a laser or strobe light. The PC is equipped with 1 GB RAM that is used to store the images before shifting them to the hard disk. Therefore, the

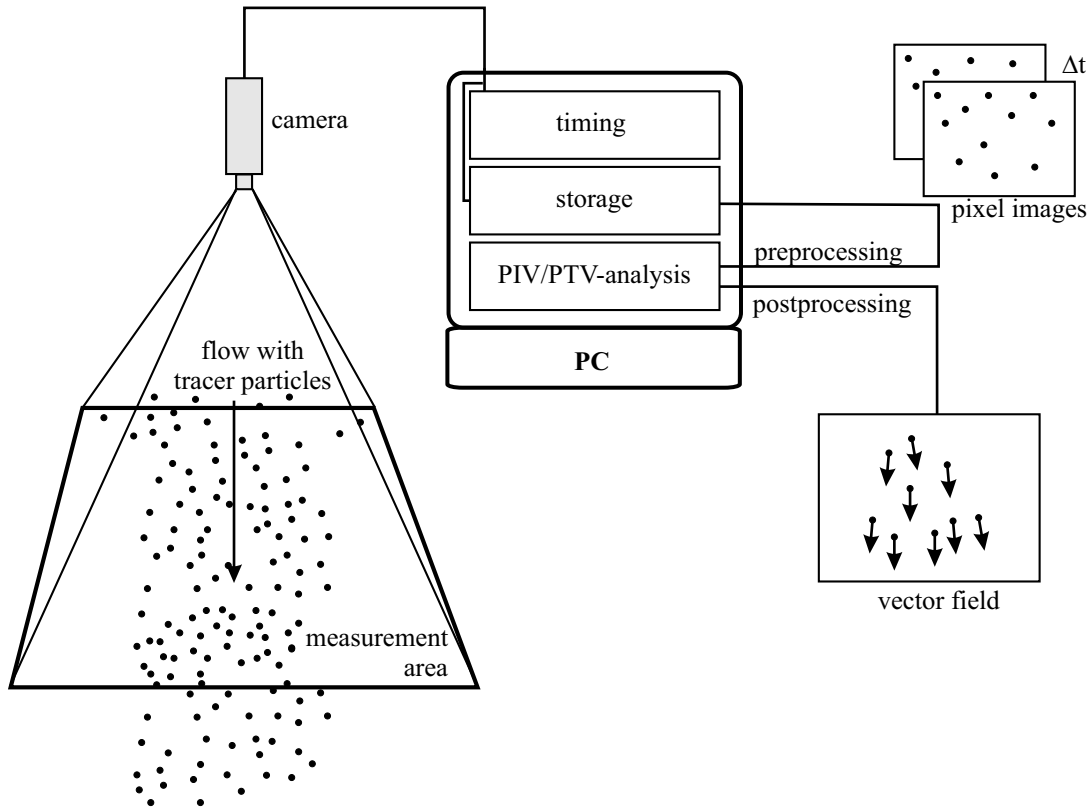


Figure 4.3. Schematic sketch of the different components of a typical PIV system

RAM is the limiting factor for the length of a time series. To control the capturing process and the analysis of the images the software package DaVis© provided by LaVision was used. DaVis includes algorithms for PIV and Particle-Tracking-Velocimetry (PTV) evaluation. While the PTV algorithm attempts to track every particle from one image to the next, the PIV algorithm is based on a standard cross-correlation via Fast Fourier Transformation (Adrian 1991) between two images. A limitation of the DaVis PTV package is that only 16000 particles per image are supported.

As the dynamic range of the velocities in the presented case is very high, a simple PIV algorithm would fail. Therefore, an adaptive multi-pass process is applied, reducing the initial cell size to a fixed smaller cell size. Then, a first vector field of the big cell size is computed and used as a reference vector field for the next pass. In the next pass the cell size is half the previous size and the vector calculated in the first is used as a best-choice cell shift for the second pass. With this multi-pass computing larger velocity differences can be captured without losing a high resolution (Scarano & Riethmüller 1999).

Camera and optics. The PCO camera, Sensicam, with a 1/2inch-CCD-sensor, has a resolution of 1280 x 1024 pixels with a gray scale resolution of 12 bits. With a pixel clock of 12.5MHz, frame-rates up to 8Hz are possible. The camera can be operated in two different modes. The first mode is a single-frame mode. In this mode, every image is directly read out after it is captured, so that the frames are captured in even time steps. If the flow field

is slow enough, this mode can be used, and 7 velocity fields per second can be obtained. For flows with higher velocities, the double frame mode has to be used. In this mode, two images can be captured within a very short time. The first image is not read out, but shifted to the storage position on the chip and then the second frame is taken. The shortest time allowed between the two frames is 400ns. During the transfer of these two frames to the RAM a read-out time of 125 ms is necessary, which allows measurement series of four double frames per seconds, and, therefore, four velocity fields per second. The chosen camera (Sensicam) needs a specialized camera-specific frame-grabber. Camera and frame-grabber are connected with a fiber-optic cable that allows distances between both elements up to 1000m.

To cover large measurement areas while the space above the laboratory flume is limited to a maximum of three meters, an f-mount, 15mm wide angle lens (NIKON©) has been used. If the camera is mounted normal to the water surface, the image distortion in the boundary regions of the lens is less than 1%. This lens provides high resolution combined with high luminosity, which is important for the measurement accuracy.

Seeding particles. A difficult part of the PIV setup is the choice of proper tracer particles. In case of surface velocity measurements, the density of the tracer particles must be smaller than the density of water. On the other hand, particles which are too light can be affected by air flow above the water surface. All the material listed in table 4.1 is floating on the water surface. In the case of Polystyrene, the influence of the air flow above the water surface was clearly visible. Polyethylene (PE) and Polypropylene (PP) have a density of $0,9 \text{ g/cm}^3$, which seems to be a reasonable value for the used purpose.

Another important parameter is the size of the particles. Very small particles are invisible for the camera, or they evoke peak-locking effects (section 4.2.3). Raffel et al. (1998) suggests to use particles, with a diameter bigger than 1.5 pixel on the camera chip. Good results can be achieved with particle dimensions between 2 to 5 pixels. If the particles are too large, they do not follow the flow structures, that we want to resolve, due to inertial forces. Flow structures can be adequately resolved, if their length scale is at least 5 times bigger than the particle diameter. In the present application, the particle diameter was about 2-3 mm.

A serious problem in applications at the water surface is given by the fact that many particle materials have the tendency to form conglomerates, due to surface tension effects. All of the tested materials show this tendency. Extensive bottle tests with all kinds coating materials showed that PE and PP coated with lacquer exhibits minimal agglomeration effects and has been adopted in the presented applications.

Also, the color of the particles plays a certain role, as they have to provide sufficient contrast to the channel bottom. In our case the flume bottom was necessarily painted white, because of the concentration measurements. Therefore, black lacquer has been chosen to coat the particles. A blender was used to add the lacquer finish on the particles to avoid conglomeration during the drying process. Experiments attempted with fluorescent material showed much less contrast.

Summarizing the properties of the different particles (table 4.1), it can be stated that Polypropylene with additional matt black lacquer finish gives the best results. These

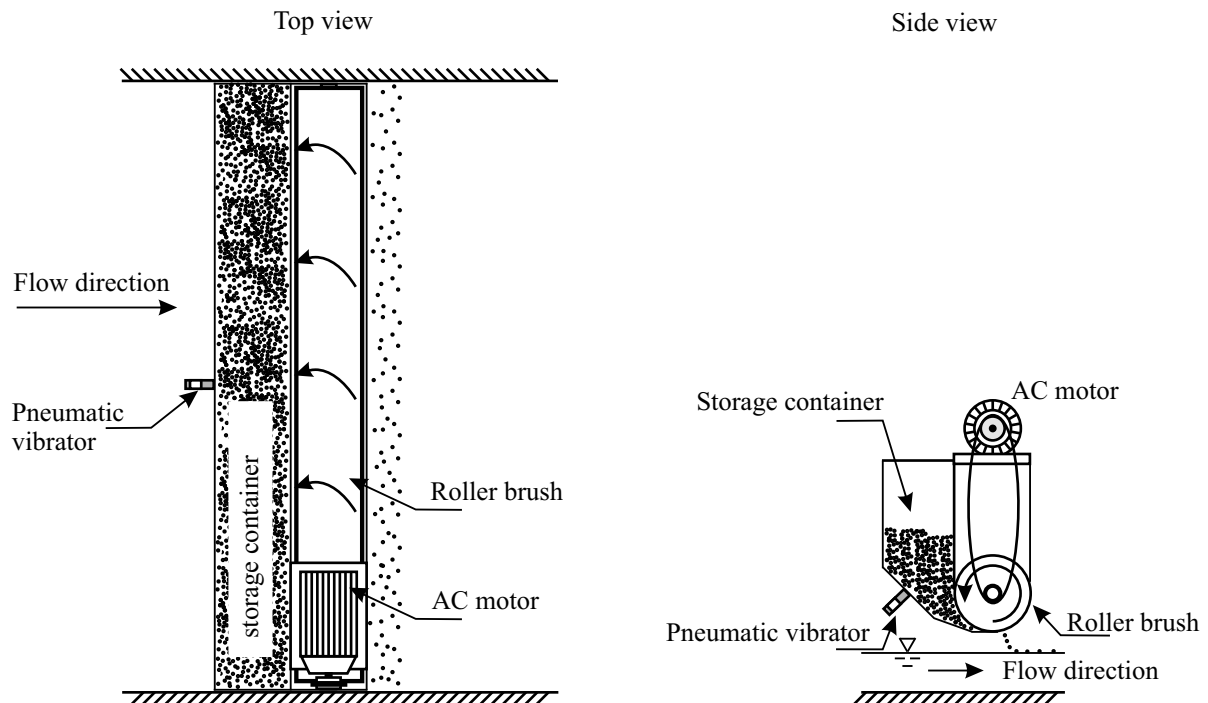
Table 4.1. Properties of the different tracer material and their applicability to water surface measurementst

	(1)	(2)	(3)	(4)	(5)	(6)
material	Polystyrene	coal	wood	expanded clay	Polyethylene	Polypropylene
form	sphere	die	sphere	sphere	cylinder	cylinder
diameter [mm]	2	1-5	4	1-2	2-3	2-3
density [g/cm ³]	0.04	0.50	0.50	0.73	0.90	0.90
resistance to air flow	-	+	+	+	+	+
avoidance of agglomeration	-	-	o	-	-	o
price	o	+	-	+	+	+
durability	+	o	-	+	+	+

-poor, o acceptable, + good

particles can be purchased by "Feddersen & Co." under the name "Hostacom PPR 1042 12".

Particle dispenser. A homogeneous particle distribution within the area of interest is essential for good results in terms of a closed velocity vector field. In regions where the particle density is too small, the cross correlation algorithm fails and misleading vectors occur. Therefore, a particle dispenser has been developed, which is able to seed the water surface homogeneously with particles. The seeding rate can be adjusted according to the ambient flow velocity (figure 4.4).

**Figure 4.4.** Schematic top and side view of the particle dispenser

The essential part of the dispenser is a roller brush, which is driven by an *AC* gear motor. With the help of a planetary gear system, the velocity of the brush can be continuously changed between zero and five rounds per minute, to controls the particle release rate. The brush ensures an equal particle distribution over the whole width of the flow. In the present case the maximum seeding width is 1.7m. The tracer particles are stored in a container behind the brush. An important feature is a pneumatic vibrator, that has been installed on the container in order to ensure a constant particle supply. The vibrator moves the metal wall of the storage container with up to 6000 oscillations per minute and centrifugal force of 50N. The force and number of oscillations can be adapted to the material and its humidity.

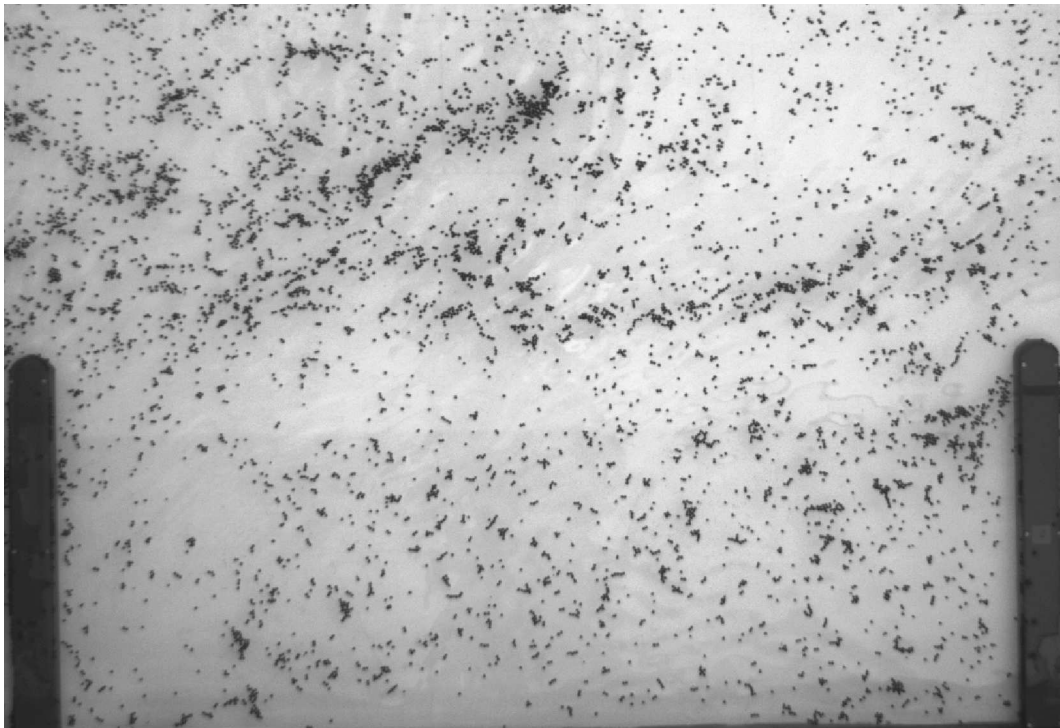


Figure 4.5. Raw pictures of the measurement field where the Polypropylene particles on the water surface are visible.

The dispenser is located only a few centimeters over the water surface in order to avoid surface waves produced by falling particles. It is also advisable to place the dispenser close to the measurement plane to minimize the number and size of particle conglomerates. In figure 4.5 a typical raw picture is shown, which is located 1.5 m downstream of the particle dispenser. Even if the particles have only a weak tendency to form conglomerates it can be seen that at some positions the particles stick together. It could be observed, that in the region of the shear layer these conglomerates do also break up.

Because the amount of particles needed for an experiment is quite high, the particles are recollected in a sieve at the end of the flow section and can be reused. In the present

case, approximately 2ℓ of the mentioned particles are needed to seed the water surface for one minute.

Illumination. In the single frame mode that can be used under slow flow conditions, the measurement plane can be illuminated with constant halogen floodlights. Four 1 kW-floodlights were used indirectly to achieve diffusive light and to reduce the disturbing effects of shadows, which leads to homogeneous illumination conditions. Additionally, matte reflection screens were installed above the flume to reduce inhomogeneous mirroring from the ceiling. In the double frame mode, which is to used under fast flow conditions, the camera shutter is not closed after the second image until both frames are read out. In this case, a strong stroboscope is used as light source, which has been triggered with the help of the PTU of the PIV system. An external optical sensor was developed to measure delay times and jitter of the stroboscope for the programming of the timing scheme.

4.2.3 Accuracy of the PIV system

A common technique to test the accuracy of PIV system is given by Westerweel (2000), where artificial particle clouds are generated with random spatial distribution to simulate a reproducible particle movement under well determined boundary conditions.

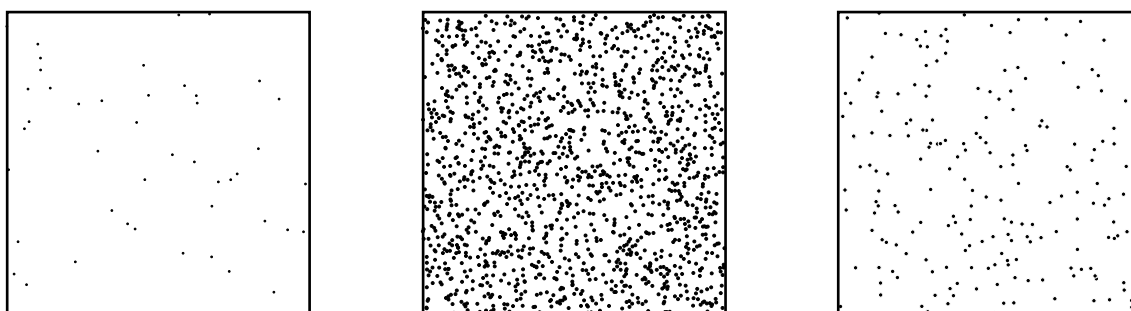


Figure 4.6. Artificial particle clouds with different particle size and density

In the present case, the randomly generated particle clouds were plotted on white paper and mounted on a 3-D positioning system below the *CCD* camera. This positioning system is able to do stepwise movements, with an accuracy of 0.0125mm. With the aid of this setup the measurement accuracy of the complete system, including the camera, was determined, depending on particle size, particle density, and particle displacement including the effect of shear.

The particle size is an important parameter in terms of the measurement accuracy. In figure 4.7 a section of a digital image is plotted showing the intensity distribution of one particle.

The PIV software is now trying to find the center of mass of the particle by fitting a Gaussian curve over the intensity distribution (figure 4.8). If the particle is smaller than one pixel (figure 4.8, ii), it is obvious that the intensity distribution finds the center of

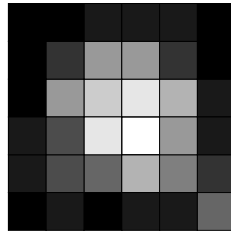


Figure 4.7. Digital image of a particle in a cell of 6 x 6 pixels

mass at a position of an integer pixel value. In the case of larger particles (figure 4.8, i), the center of mass can be determined with an accuracy of 0.1 pixels (Raffel et al. 1998, Nübel & Weitbrecht 2002).

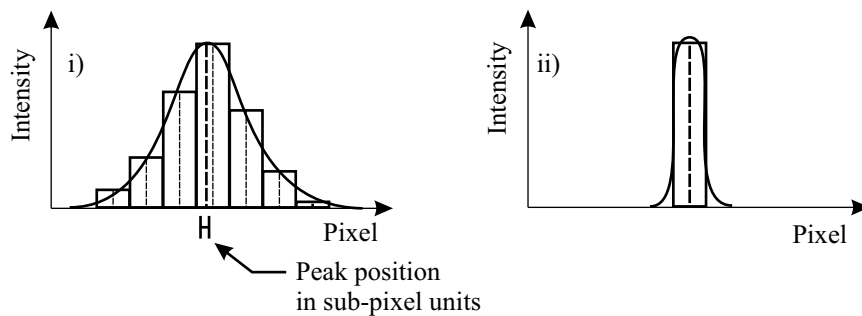


Figure 4.8. Evaluation of the position of the center of mass of a particle; i) particle is larger than 1.5 pixels, leading to a position accuracy in the order of sub-pixel units; ii) Particle is smaller than one pixel, leading to an accuracy in the order of one pixel.

If most of the particles are smaller than one pixel, the particle displacement distribution of a vector field contains strong peaks at the position of integer pixel displacement, which is called peak-locking-effect (figure 4.9). In the present case, tests using particles of different size showed that the minimal value of the particle diameter had to be at least 1.5 pixels in order to avoid peak-locking effects.

Raffel et al. (1998) showed that particle concentration influences the probability of detecting the valid displacement as well as the measurement uncertainty. Tests with changing particle concentration showed that the number of particles in each interrogation area should be higher than 5. The particle dispenser operation satisfies this criterion.

Tests to determine the influence of the particle displacement showed that the maximum particle displacement between two frames should be less than 25% of the interrogation area. For higher flow velocities the camera has to be used in the double shutter mode, using stroboscopic illumination. This shortens the time between two picture frames and the particle displacement, respectively.

Every image contains a certain distortion, which is caused by the camera lens. By tilting the camera towards the vertical, an additional error due to distortion effects has to

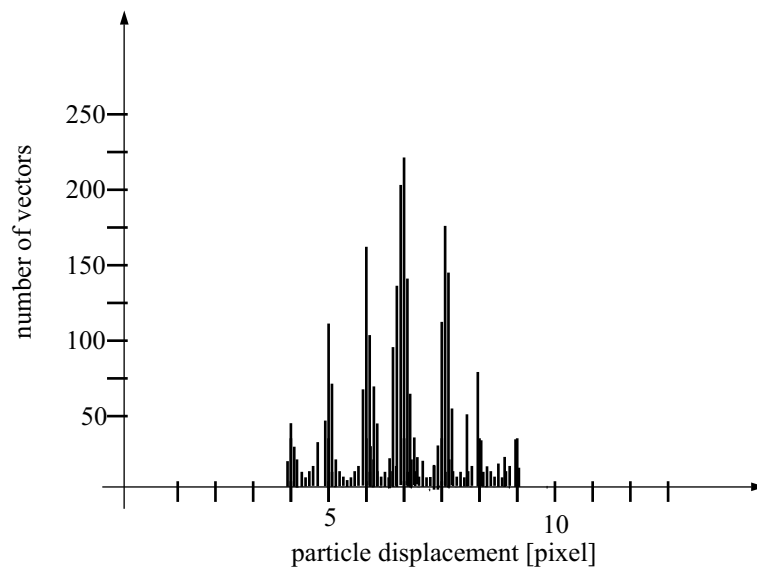


Figure 4.9. Illustration of peak locking effects, associated with insufficient particle image size, by showing a histogram of PIV displacements

be eliminated. These effects are minimized using a polynomial calibration of third degree in the x and y directions. It should be noted that this procedure increases the noise, which has a certain influence on the turbulent flow characteristics. Stronger tilting angles can only be handled by using additional optical components like a Scheimpflug optic.

Turbulent flows are characterized by random motions of different length and time scales. If a particle ensemble is transported within such a flow, it will get distorted due to shear. If the distortion in an interrogation area evoked by the velocity shear is too high, the cross correlation of the PIV evaluation can fail. Tests have been made, where every interrogation area of the second frame is rotated by a certain angle (figure 4.10) in order to determine the influence of velocity shear. Figure 4.11 shows that there is a dependency of the mean flow velocity on the rotation angle.

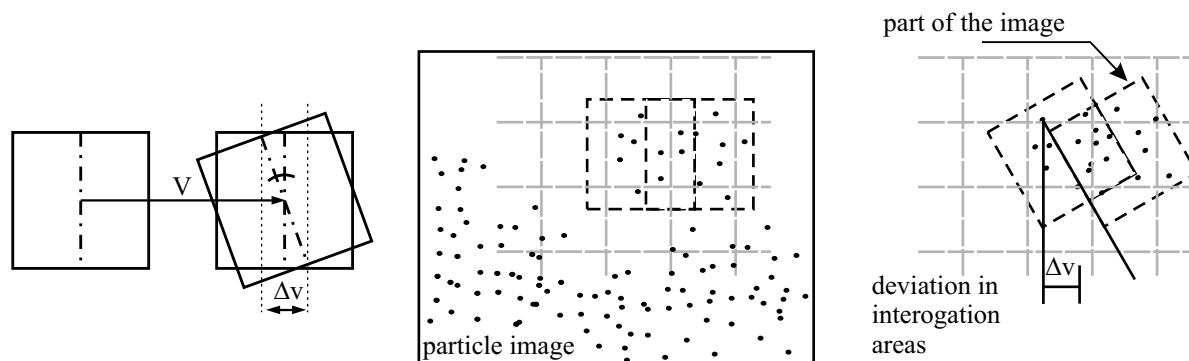


Figure 4.10. Rotation of interrogation areas in order to analyze the influence of velocity shear on the PIV results

The evaluation of the spatial standard deviation shows that additional noise generates these motions, due to the rotation of the interrogation area. Grant (1997) proposed as a quality criterion

$$\frac{\Delta u}{U} = \frac{\Delta v}{V} < 0.2 \quad (4.2)$$

with Δu and Δv as the velocity gradients in x- and y-direction and U and V the mean velocity in x- and y-direction, which could be verified in the present study.

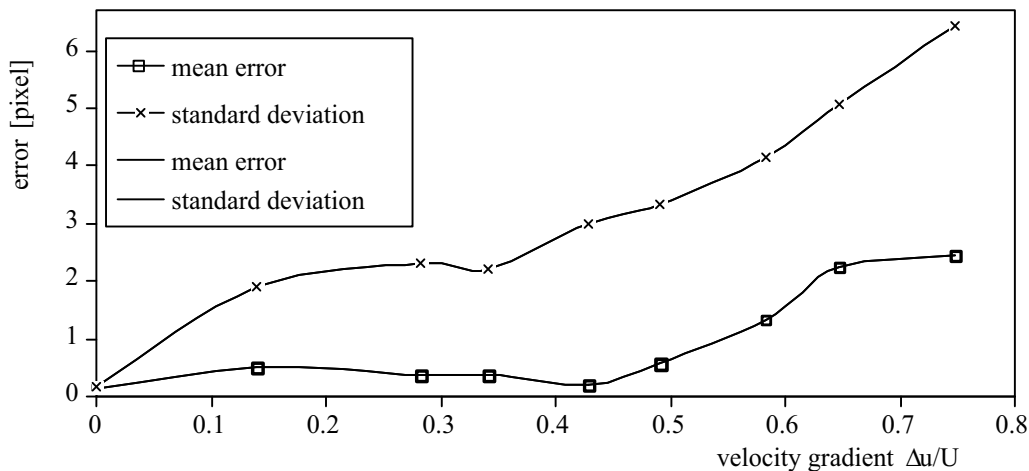


Figure 4.11. Rotation of interrogation areas in order to analyze the influence of velocity shear on the PIV results

Another test has been performed, where the particle plots were mounted on a rotating disc with a constant angular velocity to control the measured mean velocities. In figure 4.12 (i) it can be seen that the measured values represent the theoretical value very well. The strong deviations on the left hand side result from the fact that the measurement plane was not exactly centered to the camera, so that on this side, areas without particles are traveling through the measurement plane. Neglecting the left border, the deviation of the displacement from its theoretical value is less than 0.5 pixels, as shown in figure 4.12 (ii).

Image-preprocessing can also affect the accuracy. In the present case the pictures are first inverted and then filtered using a high-pass filter, which eliminates the background structures. Additional noise reduction by subtracting an offset value reduces the number of wrong vectors and the resulting pictures can be compressed much more efficiently, which saves a lot of storage capacity.

In summary, the systematic error of the measurement method is less than 0.5 pixels displacement (Kühn 2000, Weitbrecht, Kühn & Jirka 2002). The results are very sensitive, however, to different pre- and postprocessing parameters. Results can be obtained from any image-pair. For each experimental setup, the parameters have to be adjusted carefully to the existing conditions like flow velocity, size of the measurement plane, and

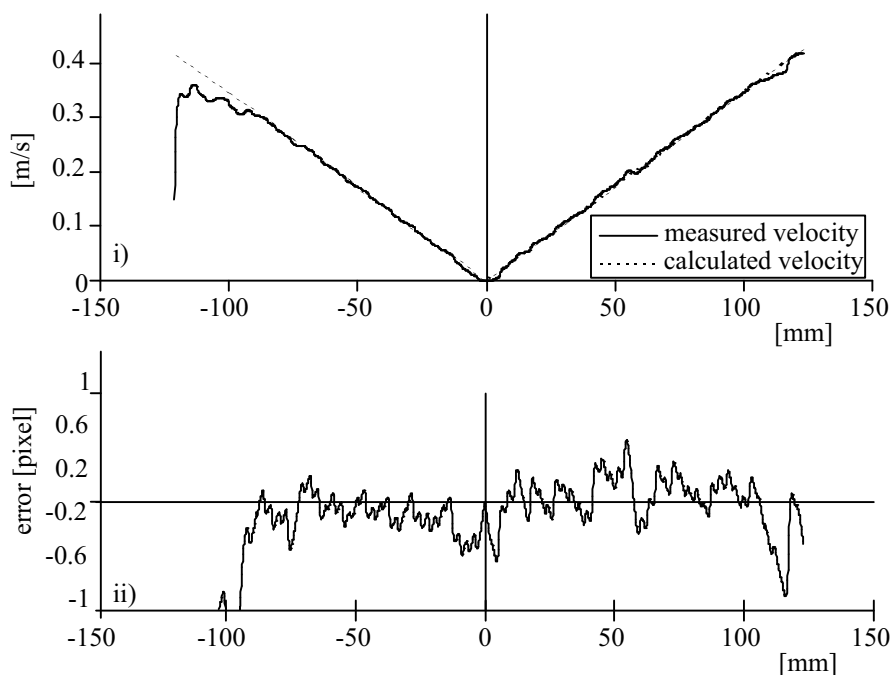


Figure 4.12. Rotating disk tests: i) Measurements of the velocity distribution; ii) Deviation from calculated velocity

illumination conditions. For the current application, the time series were captured at a frequency of 7 Hz leading to velocity fields with typically 78×64 vectors with a spatial resolution of about 2 cm in x- and y-direction.

4.2.4 PIV measuring and -evaluation settings

For every groin field setup three series of 200 images at a frequency of 7 Hz were taken to analyze the flow fields with the surface PIV system, described in section 4.2. These three series of about 30 seconds were then analyzed with the PIV software, leading to vector fields of typically 64×78 vectors, which correspond to the spatial resolution of about $2 \times 2 \text{ cm}^2$. In the following the different steps of the PIV procedure that leads from the raw picture figure 4.5 to the instantaneous vector field are described:

1) Preprocessing

Inversion of the raw picture, particles appear bright on a dark background. Filtering so that locally the value of the averaged background is subtracted. Subtraction of an offset value of 70 counts. The final preprocessed image has a black background (zero counts) and bright spots at the position of the particles. With this process the needed memory space for one picture can be reduced by a factor of ten without losing velocity information.

2) PIV evaluation

Cross-correlation of subsequent preprocessed images using a standard Fast-Fourier-Transformation algorithm. The adaptive multi-pass process has been used with an

initial cell size of 64 pixels and a final cell size of 32 pixels. The initial cell shift which helps to find the velocity vector in the region of the main channel has been set to 3 pixels. Including an overlap between every interrogation area of 50 %, this process leads to a vector field of 64 x 78 vectors, each vector representing an area of approximately 2 x 2 cm².

3) Postprocessing

During the multi-pass process the plausibility of every vector is checked by comparing the values with the surrounding vectors. If the deviation between the actual value is larger than 1.6 times the root-mean-square value of the surrounding vectors, the vector gets replaced by the second- or third-order vector. In regions, where no vector could be found, due to a lack of particles, vectors are inserted using a linear interpolation function.

The result of this procedure is visualized in figure 4.13 where instantaneous vector fields, taken from the $W/L = 0.35$, are plotted with a Δt of 2 seconds.

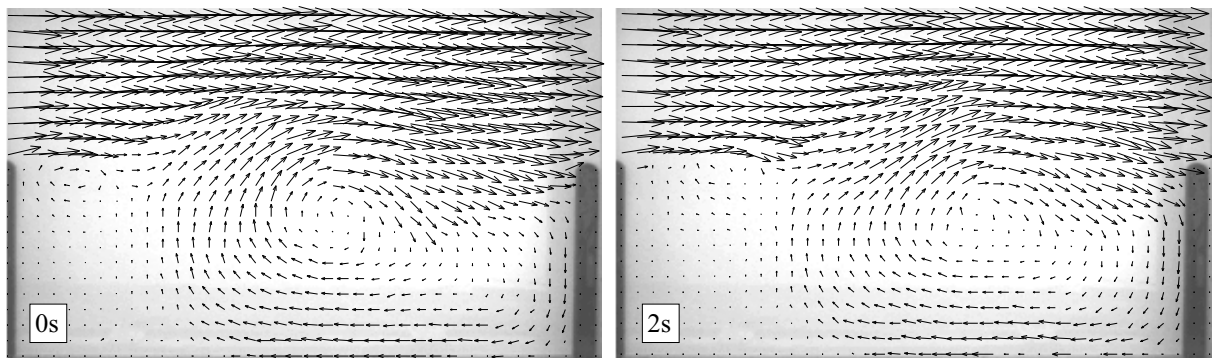


Figure 4.13. Result of surface PIV measurements where the instantaneous flow is visualized at two different time steps with a Δt of 2 seconds. Example with $W/L = 0.33$

A very efficient way of analyzing the measured time series is given by the use of 3-dimensional matrices for the u- and v-component respectively (figure 4.14).

In the present case Matlab© has been used to built these matrices, such that each 3-dimensional matrix contains 3 x 200 velocity planes. Herewith the determination of the different statistic properties reduces in Matlab© to a single line of programming and needs almost no computation time.

4.2.5 Laser-Doppler-Velocimetry (LDV)

Laser-Doppler-Velocimetry (LDV) is a point measurement technique of very high accuracy in terms of mean and turbulent flow properties (Durst, Melling & Whitelaw 1981, Ruck 1987). It determines velocities with the help of the *Doppler-Effect* that is evoked by the light refraction of small particles that travel through a measurement volume within the crossing point of two laser beams. LDV represents an optical measurement technique that

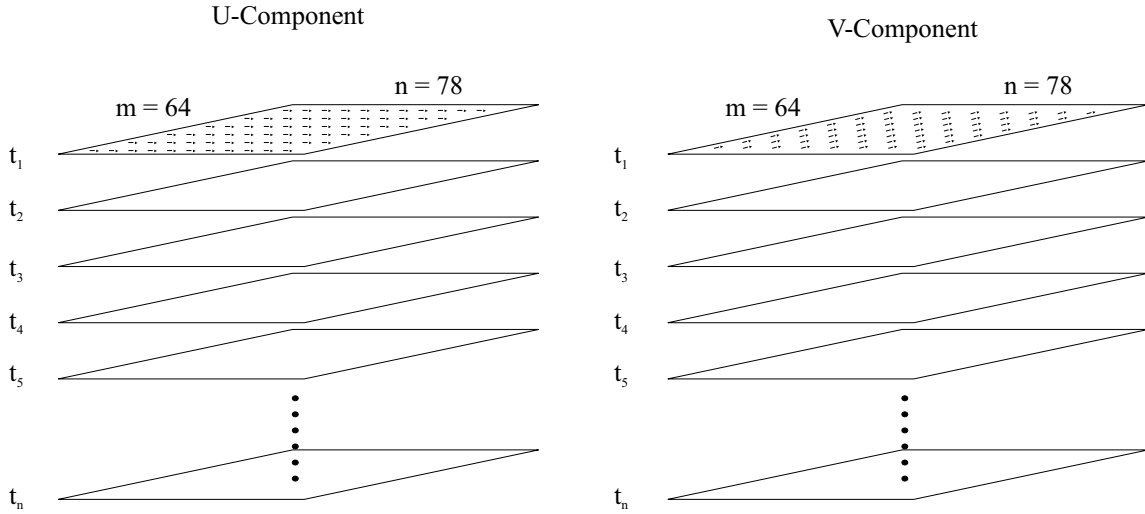


Figure 4.14. Schematic visualization of the vector processing procedures.

does not disturb the flow field as long as the density and size of the seeding particles are small. In the present case LDV measurements have been performed in order to analyze the flow structure in the vertical, which is of importance for the interpretation of the PIV results at the water surface. Due to the fact that LDV measurements are very reliable and accurate, they are used as another check for the PIV measurements.

In the present case a 2-dimensional TSI© system with a 10W Argon-Ion-Laser (INNOVA70/5E) has been used. The sensor head uses backscatter technique and has a focal length of 160mm. The sensor is connected to the multi-color beam-separator with a 10m optical fiber cable (figure 4.15). The system provides a temporal resolution of order 10^{-4} s and the size of the measurement volume is about 0.07mm x 0.80mm. The accuracy of the system has been tested to be of order 1% (von Carmer, Koch & Jirka 2000).

With the help of an automatic 3-dimensional positioning system (figure 4.1), different vertical and transverse profiles (section 4.4) of velocities in the horizontal plane (x- and y-direction) have been measured. The fact that the flume does not have a glass bottom and therefore the measurements have to be taken from above through the water surface, presents a minor problem, if surface waves are negligibly small (von Carmer 2000). If the laser beam crosses a water surface is moving, due to small surface waves, the submerged part of the laser beams and therefore the measurement volume is also moving, which, of course, has a direct influence on the results. If we assume that the influence of the waves is not biasing the movement of the measurement volume, it only has an influence on the fluctuating part of the velocity information, while the mean velocities are still correct. If the surface movements increase, the probability that the laser beams cross each other in the water body gets smaller and smaller, hence the sampling rate can be strongly reduced or can even be zero.

In order to avoid the problem of the surface waves, supplementary measurements have been performed, placing a round quartz glass plate on the water surface (diameter =

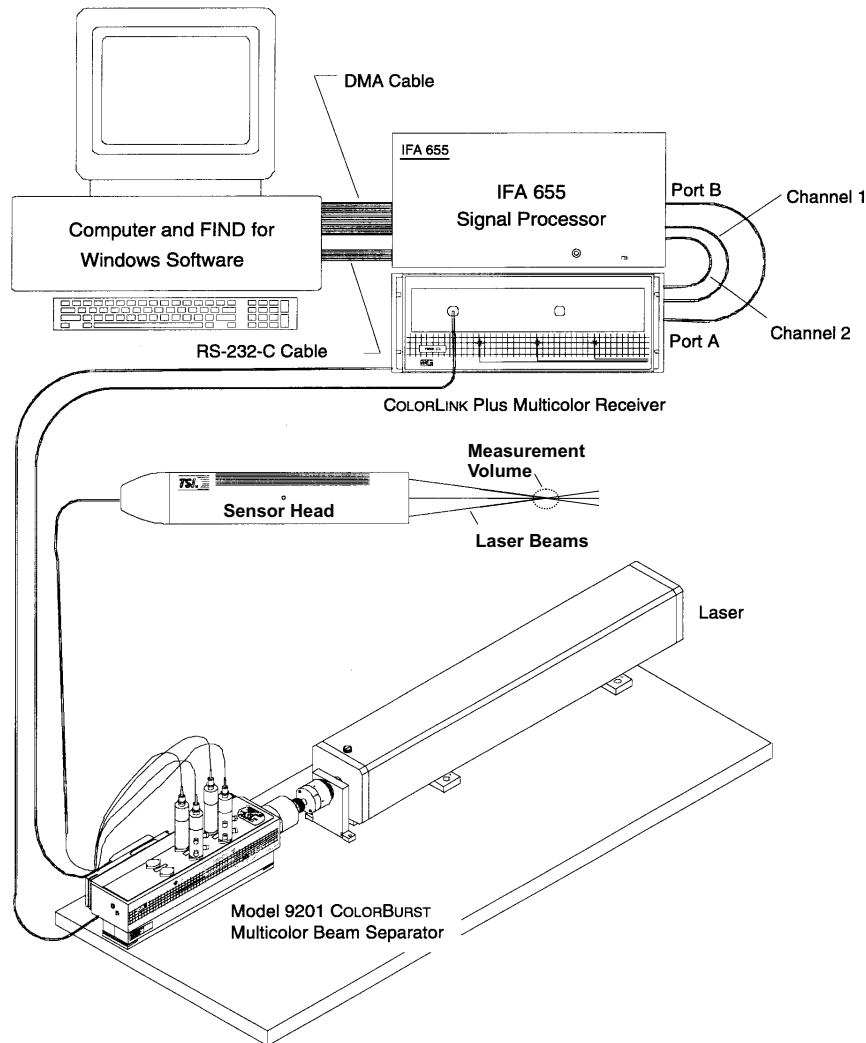


Figure 4.15. Schematic sketch of the different components of the 2-dimensional *LDV*-system taken from (TSI 1996)

50mm, thickness 6.3mm). This glass plate ensures that the laser beam is intruding the water body without being disturbed by motions of the water surface. In that case, the surface velocities are influenced by the shear at the glass plate, making a comparison with the PIV measurements impossible.

In the present case, surface waves occur especially close to the separation points in the mixing layer downstream of the groin heads. They are small enough to allow measurements of the mean flow velocities. The flow in the main channel and in the groin field is very calm and allows accurate measurements of mean flow and *rms*-values without using the glass plate on top of the water surface.

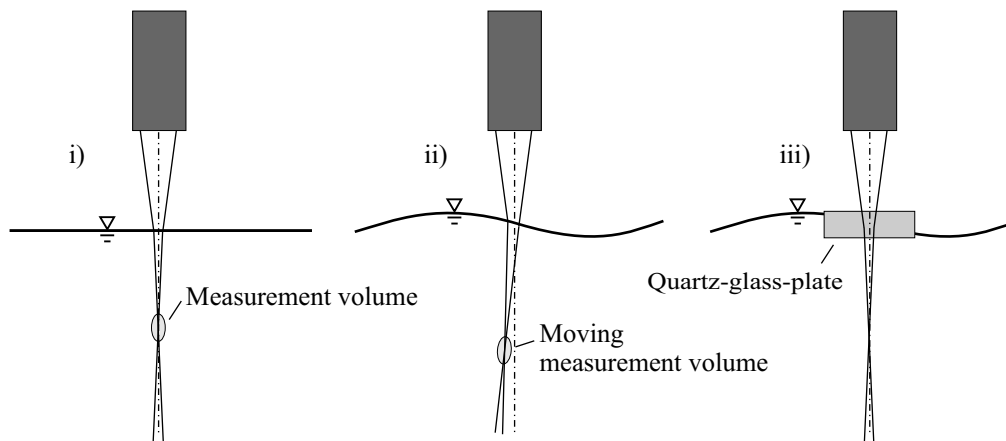


Figure 4.16. Schematic sketch of the laser beams that cross the water surface: i) in the case of horizontal water surface ; ii) in the presence of surface waves with a moving measurements -volume; iii) surface waves suppressed by a quartz-glass-plate on the water surface

4.3 Measurement technique: Planar-Concentration-Analysis (PCA)

Planar-Concentration-Analysis (PCA) has been performed to determine the mass flux between the dead-water zone and the main stream, which is driven by large, horizontal, coherent motions in the mixing layer. Because these motions are mainly two-dimensional, a depth averaged approach has been chosen. The idea of the measurements is to determine the horizontally and vertically averaged concentration decay in the dead-water zone, while the concentration in the main stream is always zero. Therefore, the tracer has to be injected instantaneously and homogeneously distributed in the horizontal plane into the dead-water zone. This has been achieved with the help of a Multi-Port-Injection-Device, described in section 4.3.1. With the help of a digital camera above the flume the concentrations in the dead-water zone are recorded.

Compared to Laser-Induced-Fluorescence (LIF) techniques, where the concentration is determined by the intensity of fluorescence which is evoked with a laser, the present case uses the effect of light absorption. In the case of high concentrations the area of interest appears dark because the tracer that is distributed homogeneously over the water depth filters the light. Zero concentration means, that the white bottom of the flume can reflect most of the light back to the camera.

4.3.1 Elements of the PCA system

Camera and optics as well as the camera control-system have already been described in section 4.2.2. In the case of concentration measurements, the 12-bit technique of the camera is an important advantage compared to standard 8-bit systems, because inhomogeneous light attenuation decreases the measurement range. For the described surface PIV measurements an 8-bit system would be sufficient.

Almost homogeneous illumination of the flow field is reached with the system described in section 4.2.2. The calibration procedure, taking into account the inhomogeneities in the illumination and background concentrations, is described in section 4.3.2.

A movable Multi-Port-Injection-Device (MPID) has been developed to provide instantaneously a homogeneous concentration field in the groin field (figure 4.17 and 4.18). The main part of the MPID is a movable injection box of 1.4 m length 0.6 m width and 2 cm high that is connected to a moving frame (figure 4.18, ii), mounted upon the flume's walls above the water surface. The bottom side of the box consists of a 3 cm x 3 cm array of thin needles, through which the tracer can be injected into the flow without penetrating the water surface.

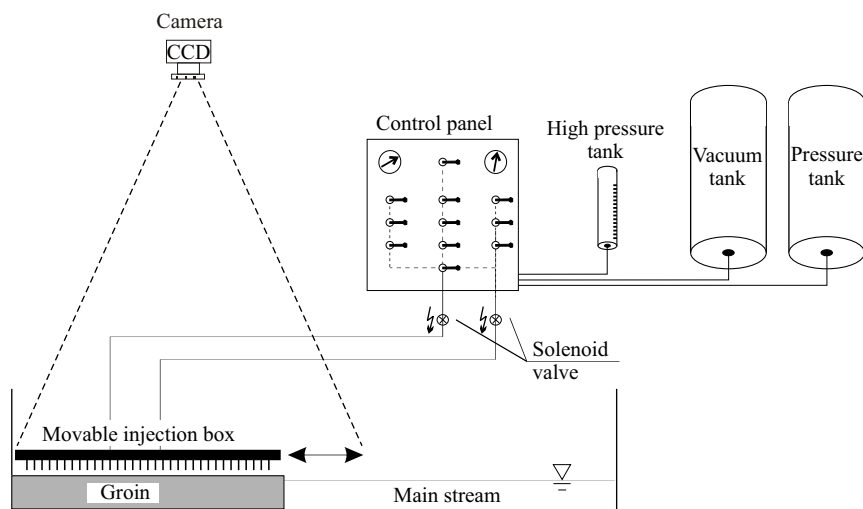


Figure 4.17. Schematic sketch of the movable Multi-Port-Injection-Device (MPID)

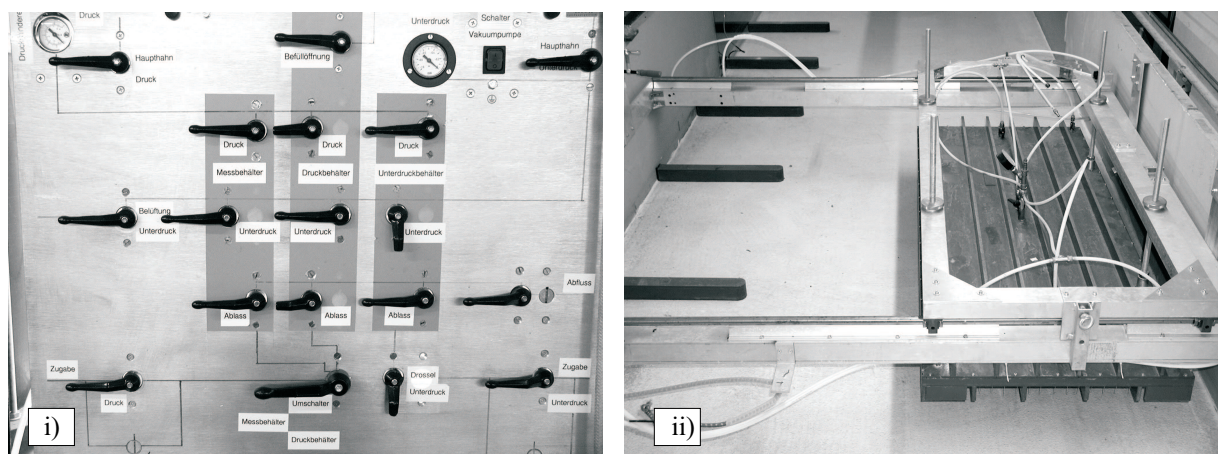


Figure 4.18. Photo of the control panel i) and the movable Multi-Port-Injection-Device ii)

The injection box is connected to a vacuum-pressure-system that allows to pump the dissolved tracer from the different reservoirs into the movable injection box and into the high pressure tank. From the high pressure tank (3.5 bar) an exact amount of tracer can be injected via the movable injection box into the water body. The tracer injection is controlled, such that a homogeneous concentration field is reached after a injection period of 5 s. At the moment when the valve of the high pressure tank is closed and the dye injection stops, the injection box can be pushed to the other side of the flume with the help of pneumatic cylinders to make the measurement field visible for the camera. The tank motion needs about 0.7 s, which means that the measurements can start 5.7 s after the start of the tracer injection. In order to avoid any disturbing dripping of dye from the needles while the box moves to the other channel wall, the valve to the vacuum tank is opened for 0.8 s right after the injection.

The system is equipped with electronic valves, such that the tracer injection and box-moving sequence can be operated by a PC. The system can also be operated manually via the control panel (figure 4.18).

Figure 4.19 shows the concentration field at the moment when the movable injection box has been pushed to the other side of the channel. In figure 4.19, i) tracer spots corresponding to single needles are still visible, which will vanish within a few seconds figure 4.19, ii).

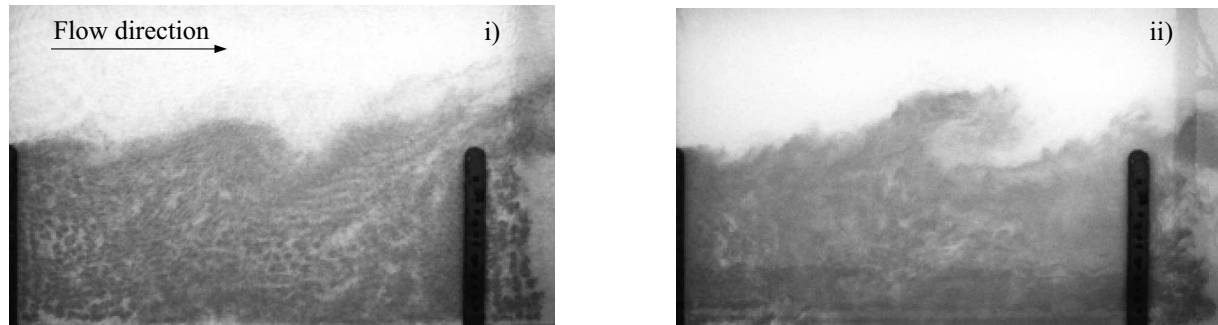


Figure 4.19. Top view on the measurement area showing the concentration field; i) 6.5 seconds after the start of the injection; ii) 16.5 seconds after the start of the injection

As tracer material red food dye (Amaranth 85, E 123) has been used. It is a color of high intensity and provides a very stable aqueous solution. Therefore, no deposition or readsorption problems occur during the experiments (Rummel, von Carmer & Jirka 2002). Previous experiments with potassium permanganate (KMnO_4) as tracer material showed that the material is settling on the flume bottom which means that it has to be cleaned after every experiment. Another problem are the needles and the flexible tubes of the *MPID* (figure 4.17), which are very sensitive to suspended particles in the water. Deposition of KMnO_4 in these parts of the *MPID* would have an influence on the hydraulic conditions which would decrease reproducibility and accuracy of the measurements.

4.3.2 Calibration and evaluation of concentration fields

In order to evaluate dye dependent concentration fields, a Matlab© routine, using a graphical user interface, has been developed. This program transfers gray scale (intensity) values into concentration fields, taking into account changes in the illumination and the background concentrations during the experiment as well as illumination inhomogeneities in the horizontal plane.

In preliminary tests, a nonlinear function had been determined that gives the best and most efficient fit for the relation of light intensity on the CCD-chip and concentration in the flow field equation 4.4. Earlier investigations (Uijtewaal et al. 2001) proposed the following relation

$$C_{i,j} = a \{-1 + \exp(b \text{Int}_{i,j})\} + c \text{Int}_{i,j} \quad (4.3)$$

with: $C_{i,j}$ = depth integrated concentration at position i, j of the flow field
 $\text{Int}_{i,j}$ = light intensity at position i, j on the CCD-chip
 a, b, c = fitting parameters

However, further investigations (Kurzke et al. 2002) revealed a problem in the determination of the coefficients a , b , and c of equation 4.3. Figure 4.20 shows the different calibration curves for different elements of the gray-scale picture. The reason for these differences are variations in the brightness of the picture due to reflections from the channel walls, the groins and the ceiling. These changes in brightness signify that the calibration curve of every element has its own characteristic form as shown in figure 4.20.

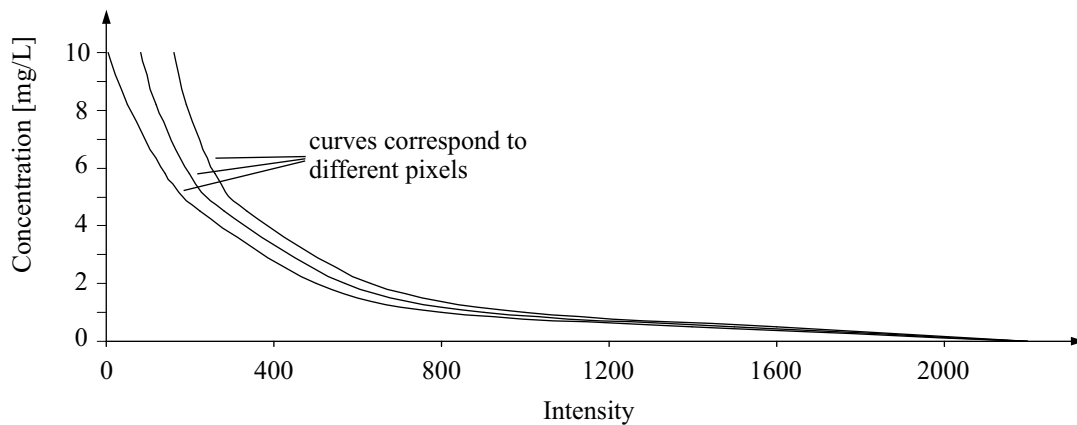


Figure 4.20. Schematic representation of intensity-dependent concentrations

Since every data set stands for one element of the intensity matrix, those variations in curvature denote that all coefficients have to be calculated for every element of the matrix. However, the coefficients a , b , and c of equation 4.3 are calculated iteratively from given concentration and intensity values, and good starting guesses speed up the

calculation. With variable curvatures, good starting values are difficult to find, leading to an increased computing time as well as an increased chance of errors. The assumption of an inverse dependency leads to

$$Int_{i,j} = a + (b C_{i,j} + c) \exp(d C_{i,j}) + e C_{i,j} \quad (4.4)$$

where d , and e are additional fitting parameters compared to equation 4.3. Although it seems that even more coefficients have to be calculated iteratively with this equation, studies showed an almost constant value of the coefficient d for every element of the matrix. Furthermore, the coefficient e represents the curve for infinite x (i.e. concentration) values, where there is no influence of the exponential part of the equation. This means that this coefficient can be estimated from the slope between the two data points with the highest concentrations. With d and e set, only the coefficients a , b , and c have to be determined iteratively. This leads to much faster computing times and less errors when fitting a curve through the data sets with equation 4.4 than with equation 4.3. So, even though the actual concentrations have to be calculated iteratively, equation 4.4 has not only proven to be the most representative fitting curve for the given data, but also assured minimal computing times.

To apply equation 4.4 to the present problem, the fitting parameters a , b and c have to be calibrated for every point of the concentration field (figure 4.21), because the illumination is not exactly homogeneous (figure 4.22).

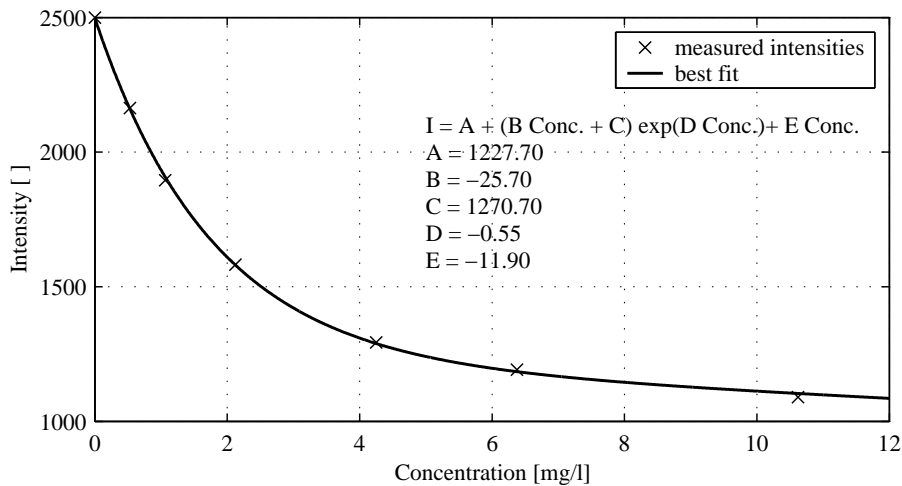


Figure 4.21. Measured intensity-concentration dependence, and fitted curve from equation 4.4.

Therefore, a sequence of pictures with known concentrations in the measurement field were captured before starting the experiment. In figure 4.22 a typical calibration procedure in the flume with four different concentrations is shown. Hereby the measurement area has been separated from the flow with the help of a frame that is somewhat larger than the measurement area to provide stationary concentration conditions. Preliminary tests

showed that the most significant intensity changes can be achieved in a range between 0 mg/ℓ and 10 mg/ℓ of the used tracer (E 123).

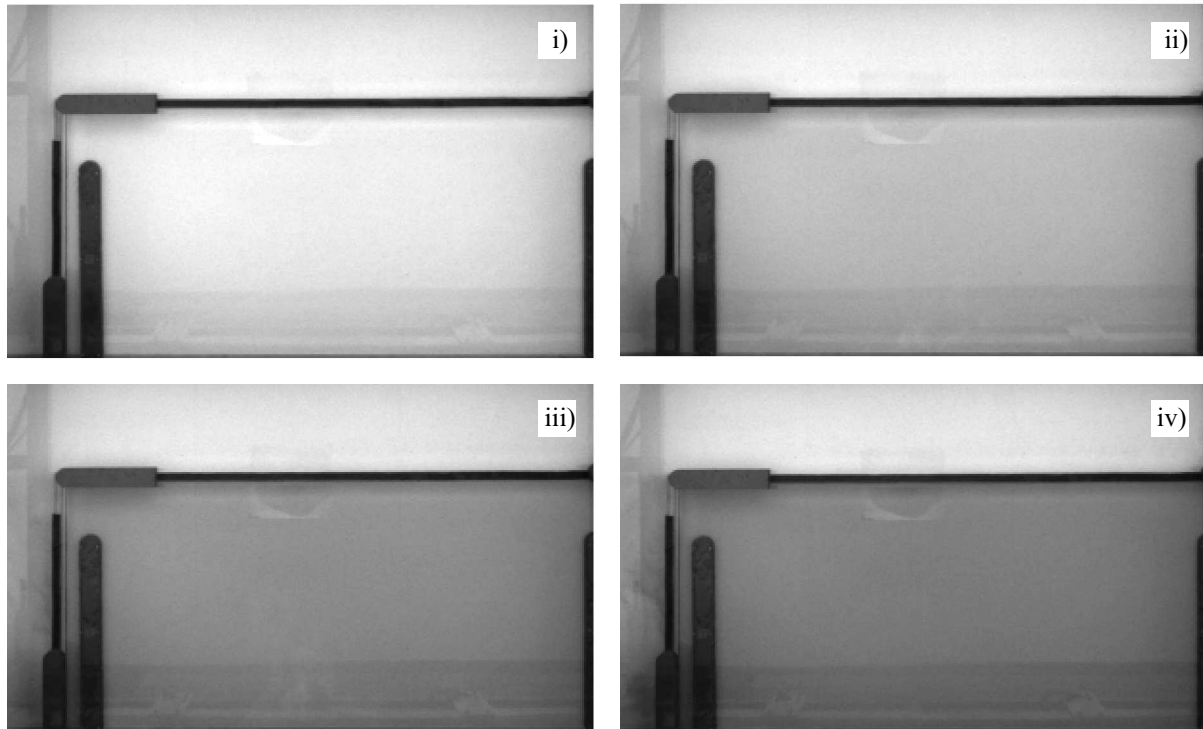


Figure 4.22. Calibration procedure with four different concentrations in the inner frame. i) 0 mg/ℓ; ii) 1.0 mg/ℓ; iii) 4.2 mg/ℓ; iv) 10.6 mg/ℓ

In figure 4.21 the measured intensity-concentration dependence are plotted together with the result from the fitting routine. The measured values correspond to a point in the lower left part of the groin field.

Before determining the concentrations in a series of gray-scale images, they have to be preprocessed. The images are resized such that the final matrix consists of about 100 elements in the area of interest (figure 4.23, ii). This saves not only memory space but also computing time. Studies with different binning factors showed that if the binning factor is selected too big, leading to a small amount of matrix elements, errors that result from the calibration are weighted too heavily. On the other hand, a small binning factor increases the number of elements where the calibration curve does not fit perfectly. Each element of the resized matrix is then subtracted from a mean reference matrix determined without tracer. This means that the actual concentration analysis was done with the intensity differences between reference picture and dye series.

In order to analyze a series of gray scale pictures the area of interest has to be defined and the reference frame has to be set (figure 4.23, i). The reference frame has to be outside the of the measurement field and represents an area of zero concentration. The mean intensity value of the reference frame in every time step is then compared with the

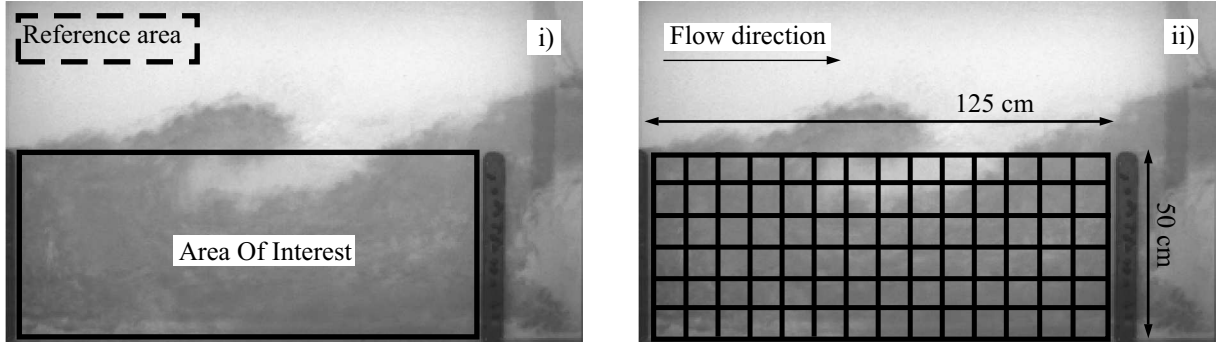


Figure 4.23. PCA, i) gray-scale picture with the measurement area and the reference frame to take into account changing illumination conditions during the experiment; ii) gray-scale picture with the final size of the concentration matrix (app. 100 elements)

corresponding value of the reference image. The intensity matrix is multiplied with the relative difference between those two values. Herewith changes in background illumination, which cannot be avoided completely during the experiment, are compensated. Also the influence of changing background concentration can be minimized with the help of this adjustment.

Tests with the reference series of zero concentration showed that the maximum deviation was about $\pm 0.015 \text{ mg}/\ell$. The error is bigger with increasing concentrations compared to evaluating the pictures from the calibration, the difference between measured and actual concentration being less than 5 %.

4.4 Experimental program

The most important process in the presence of dead-water zones in terms of mass transport, is the mass exchange between the dead-water zone and the main channel. The exchange leads to retention of tracer mass in comparison to particles flowing in the main channel. The mass exchange is governed by transverse flow velocities that force mass to cross from the main channel into the dead-zone and vice versa. In such a turbulent and shallow flow system, the dominating velocities responsible for the mass transfer are driven by large coherent flow structures that emerge at the groin heads and travel downstream in the mixing layer between groin field and main stream. The characteristics of these structures dominating the transfer velocity E between groin field and main stream are mainly determined by the following parameters:

$$E = f(U, g, \nu, D_y, h_D, h_S, B, W, L, k_s, \alpha, S) \quad (4.5)$$

with: E = exchange velocity
 U = mean flow velocity
 g = acceleration due to gravity
 ν = kinematic viscosity

D_y	=	turbulent diffusivity
h_D	=	water depth in the groin field
h_S	=	water depth in the main stream
B	=	channel width
W	=	length of the groin
L	=	length of the groin field
k_s	=	bed roughness
α	=	inclination angle of the groin
S	=	shape of the groin

Equation 4.5 can be rewritten leading to the following dimensionless form

$$\frac{E}{U} = f \left(\frac{h_S U}{\nu}, \frac{U}{\sqrt{g h_S}}, \frac{D_y}{h_S U}, \frac{k_s}{h_S}, \frac{h_D}{h_S}, \frac{B}{h_S}, \frac{W}{L}, \alpha, S \right) \quad (4.6)$$

where the dimensionless form of the exchange velocity E/U represents the exchange coefficient k that has been introduced in section 3.4.1. Therefore, equation 4.6 can be interpreted as

$$k = f \left(Re, Fr, Pe, \frac{k_s}{h_S}, \frac{h_D}{h_S}, \frac{B}{h_S}, \frac{W}{L}, \alpha, S \right) \quad (4.7)$$

with Re = Reynolds-Number, Fr = Froude-Number and Pe = Peclet-Number.

The influence of viscous forces expressed by the Reynolds-Number (Re) in most cases of the present experiments is negligible. Sufficiently large Re (typically 7300 in the main stream) have been chosen to ensure fully turbulent flow conditions. Regions of low Re can be found in the groin field and especially in secondary gyres where the flow velocities are small. However, these regions are small compared of regions with strong turbulent flow so that we can assume the influence of Re to be small compared to other influences.

In order to reproduce flow conditions that are similar to the real world the Froude-Number (Fr) has to be chosen in a reasonable range. In the present experiments Fr , as defined in equation 4.6 and 4.7, is constant with 0.24.

The influence of varying diffusivity can be expressed with the Peclet-Number (Pe) that describes the ratio between advective and diffusive transport. Within the present problem the mass transport across the groin field boundary expressed by the exchange velocity E contains the diffusive mass transport and is therefore, a part of the quantity that has to be determined. In chapter 6.3.1 the influence of the Peclet-Number is discussed within the Lagrangian-Particle-Tracking approach.

The fourth term in equation 4.7 describes the influence of bed roughness on the mass exchange processes. The influence of bed roughness can be divided in two parts. First, bed roughness enhances turbulent mixing and therefore supports turbulent mixing. Second, bed roughness leads to increased energy and momentum losses, which decreases the advective transport in the region of the dead-water-zone and towards the groin field boundary. Westrich (1978) stated that the influence of the bed roughness is negligible in small dead-water-zones, but increases with the shallowness of the flow. A slight increase of the bed

roughness after Westrich (1978) leads to increased exchange. As the roughness is increased further, the mass exchange gets damped. From these studies can be summarized, that the influence of bed roughness is small as long as the roughness elements consist of sand or gravel. Considering vegetation as roughness, the influences on the mass exchange can have large influence. In the present experiments the bed roughness has been set constant.

The influence of the water depth is expected to be small as long as the flow is fully turbulent and shallow. In the present experiments two sets with changing water depth have been performed with a mean water depth of 50 % of the water depth in the main channel. The water depth in the main channel has been set constant. The contact area between dead-water zone and main channel, which controls the mass exchange, is determined mainly by the water depth h_d in the dead-water zone. If it is assumed that the vertical velocity distribution in the mixing layer is much more uniform than in the main channel, the influence of the difference between water depth in the main channel and in the dead-water zone is small. Therefore, in all experiments except experiment No. 18 from table 4.2 the water depth in the main channel and in the groin field are equal.

The term B/h_S expresses the influence of the river width on the mass exchange. If we assume that the channel half width B is large compared to the horizontal extent of the coherent flow structures in the mixing layer, the influence of B can be neglected with respect to the mass exchange. This does not mean that the channel width is negligible with respect to the 1-dimensional longitudinal dispersion coefficient, which is shown in chapter 6.

As has been mentioned before, (Lehmann 1999) stated that the groin shape is of minor influence on the mass exchange as long as sharp edges are avoided. Therefore, in the present study changes of the groin shape, expressed by S , is not taken into account.

In nature the majority of the groins are positioned with an inclination angle of 90° to the main flow direction. In some cases upstream inclined groins can be found, for example in the river Elbe. Preliminary experiments showed that the inclination angle can have a strong influence on the mean flow pattern in the dead-water-zone. Therefore, the inclination angle has been varied in the experiments No. 10-13 (4.2) in order to determine these additional effects (figure 4.24).

Taking into account the previous assumptions it can be stated that under typical turbulent flow conditions and low Froude-Numbers a major influence on the mass exchange is given by the aspect ratio W/L and the inclination angle α leading to the following simplified relation

$$k = \frac{E}{U} = f\left(\frac{W}{L}, \alpha\right) \quad (4.8)$$

In section 2.2 it could be shown that in nature the most common type of groin field represents more or less a rectangular box with different aspect ratios. Therefore, groin fields with different W/L ratios varying from 0.17 up to 3.5 have been investigated. The very narrow dead-water zones with $W/L > 1$ do not represent typical groin fields, but can be seen as extreme cases of harbor facilities. These cases help to understand the functional relation between exchange and geometry. In table 4.2 the settings for the different experiments are summarized.

Table 4.2. Experimental settings, describing the positions, width and length and inclination angles of the groins fields.

Series No.	Length L [m]	Width W [m]	W/L	Inclination angle [°]	Velocity U [m/s]	Water depth h_S [m]	Feature
1	1.45	0.5	0.35	90	0.16	0.046	
2	1.25	0.5	0.40	90	0.16	0.046	reference case
3	1.05	0.5	0.48	90	0.16	0.046	
4	0.85	0.5	0.59	90	0.16	0.046	(upper part of figure 4.24)
5	0.65	0.5	0.77	90	0.16	0.046	
6	0.45	0.5	1.12	90	0.16	0.046	
7	0.25	0.5	2.00	90	0.16	0.046	
8	0.15	0.5	3.35	90	0.16	0.046	
9	1.25	0.5	0.40	90	0.17	0.058	submerged groins
10	1.16	0.46	0.40	64	0.15	0.046	backward inclined groins
11	1.16	0.46	0.40	116	0.15	0.046	forward inclined groins
12	0.46	0.46	1.00	64	0.16	0.046	(lower part of figure 4.24)
13	0.46	0.46	1.00	116	0.16	0.046	
14	1.45	0.25	0.17	90	0.16	0.046	short groins
15	1.00	0.25	0.25	90	0.16	0.046	(mid part of figure 4.24)
16	0.63	0.25	0.40	90	0.16	0.046	
17	1.25	0.5	0.40	90	0.16	0.046	groin field with sloping depth*
18	1.25	0.5	0.40	90	0.16	0.046	groin field with half depth**

* figure 4.25 iii)

** figure 4.25 iv)

Series No. 1-8 represent experiments where all the parameters except the spacing between the groins were fixed (figure 4.24). In series No. 14-16, the groin field width is only 50%, which reduces also the groin field volume to 25% because the aspect ratio is kept constant. This allows the investigation of cases where the aspect ratio W/L is smaller than 0.35 without changing the optical unit of the PIV system. Furthermore, these measurements give additional information about the influence of the dead-zone volume on the transport characteristics, because the W/L ratio is constant while the overall volume changes. Also in series No. 17,18 (figure 4.25 iii,iv) the groin field volume has been reduced to 50% by changing the position of the groin field bottom. For the cases 18 and especially 17 it has to be stated that due to the small water depths in the region of the channel wall combined with low flow velocities the Reynolds number is very low, which means that viscous effects can play a role.

The influence of inclined groins have been simulated in the experiments No. 10-13 with two different W/L -ratios, where the inclination angle has been changed from 90° to 64° (backward inclined) and 116° (forward inclined, see lower part of figure 4.24). Forward inclined groins ($\alpha > 90^\circ$) rarely exist in nature, whereas backward inclined groins with an inclination angle $\alpha < 90^\circ$ can be found in the river Elbe.

Series No. 9 (table 4.2) has been performed in order to show the different flow characteristics of submerged groin fields. If the groins are submerged, the mean flow velocity in x-direction in the region of the dead-water zone is non-zero and the mass exchange is not limited to the contact area between dead-water zone and main channel. Strongly 3-dimensional flow patterns evolve at the downstream side of the groins, which make

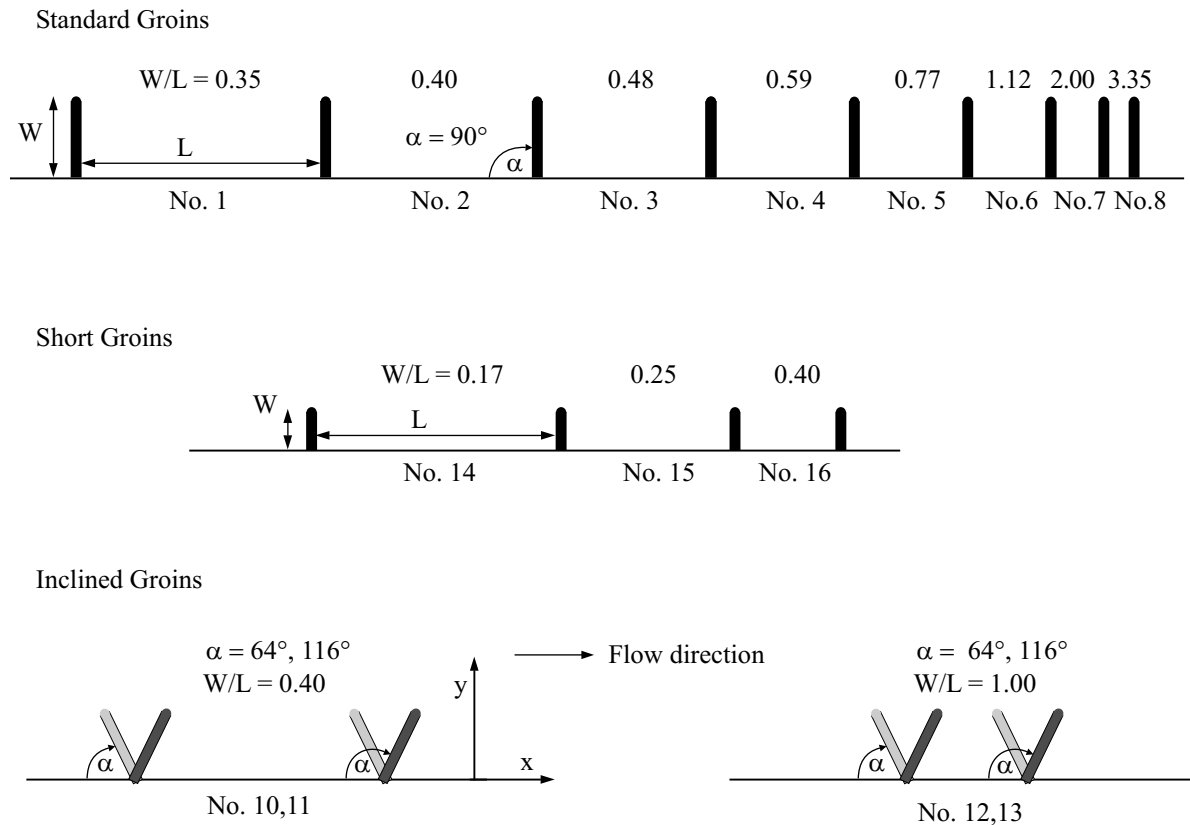


Figure 4.24. Schematic top view of the different aspect ratios and the different inclination angles; the indicated numbers correspond to the different cases described in table 4.2

it impossible to describe the flow characteristics with PIV measurements at the water surface. Also the depth-averaged PCA methods fails in the case of submerged groins. The upper layer of the dead-zone volume immediately is transported downstream with a certain mean flow velocity. During the time needed for the tracer injection and the movement of the injection box, the mass has already travelled already half the length of the dead-water zone downstream.

For each experiment described in table 4.2 the velocity pattern has been investigated with surface PIV measurements (section 4.2), and the exchange processes have been determined with depth average planar concentration measurements (section 4.3). Additional LDV measurements have been performed for experiment No. 2 in order to verify the PIV measurements and to determine vertical velocity profiles.

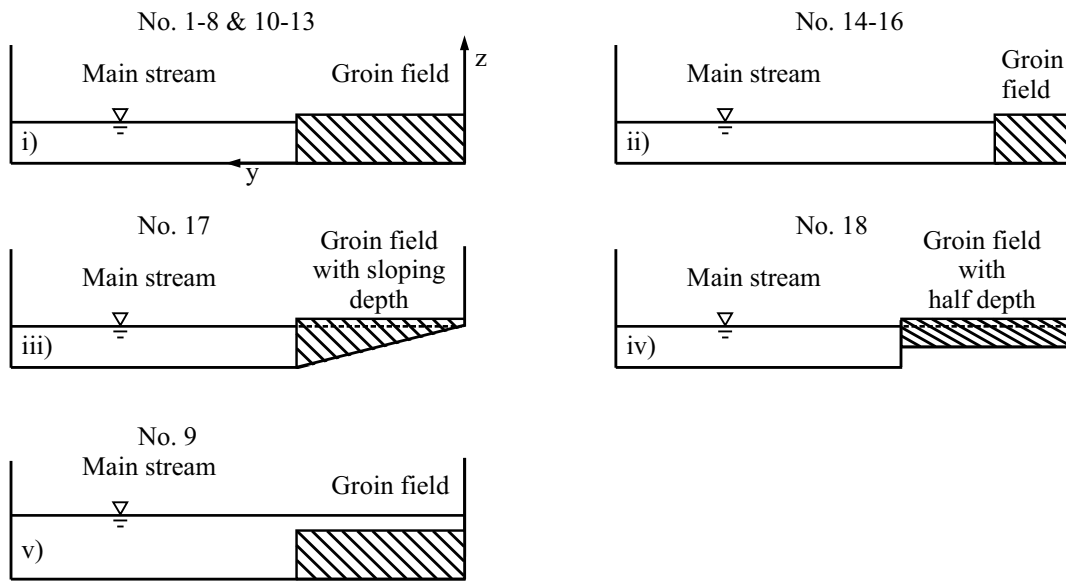


Figure 4.25. Schematic side view of the different experimental setups; the indicated numbers correspond to the different cases described in table 4.2

5. Experimental Results

5.1 Measured flow velocities

In this section, a quantitative description of the flow pattern and mass exchange properties in the presence of groin fields is given. First, the reference case (No. 2 of table 4.2) is presented in detail, which is then compared with the results of the experiments with inclined groins, short groins, submerged groins, and the experiments with reduced dead-zone volume, respectively.

5.1.1 Reference case ($W/L = 0.4$, $\alpha = 90^\circ$)

The reference case is given by experiment No. 2 (table 4.2) where the 50 cm long groin elements are positioned perpendicular to the main flow direction with a groin field aspect ratio $W/L = 0.4$. In that case, the water depth h is 4.6 cm in the main channel as well as in the groin field. The mean flow velocity is about 16 cm/s, which corresponds to a flow rate of 9.1 ℓ/s in the flume. With the given mean flow velocity and water depth the bulk Reynolds Number is 7360. The slope of the flume bottom has been adjusted to 0.032 %, which allows a flow regime in the main channel that is close to normal flow conditions.

Mean flow properties. A good impression of the mean flow properties in dead-water zones can be given with the help of streamline plots. In figure 5.1, i) the typical recirculation zone can be seen with a large primary gyre and a small secondary gyre in the upstream corner of the dead-zone. The primary gyre is driven by momentum exchange between main stream and dead-water zone and rotates in clockwise direction. The secondary gyre has no direct contact area with the main stream and is driven anticlockwise by momentum exchange with the primary gyre. In the reference case the secondary gyre covers about 15 % of the dead-zone volume.

As it is the ultimate goal of this study to determine 1-dimensional longitudinal dispersion coefficients, which are determined by velocity shear and transverse turbulent diffusion (section 3.2), we have a closer look at the mean velocity profiles of the u-component. The velocity profile in figure 5.1, ii) in the main stream part of the flow has the typical shape of a mixing layer velocity profile and can be approximated using a hyperbolic tangent function of the form

$$\frac{u(y)}{U_s} = a \tanh\left(\frac{y}{h_S} b\right) + c \quad (5.1)$$

where a, b and c are constants that have to be adapted. In figure 5.1, ii) the mean velocity profile for the $W/L = 0.4$ case is plotted together with the result of a fitting algorithm.

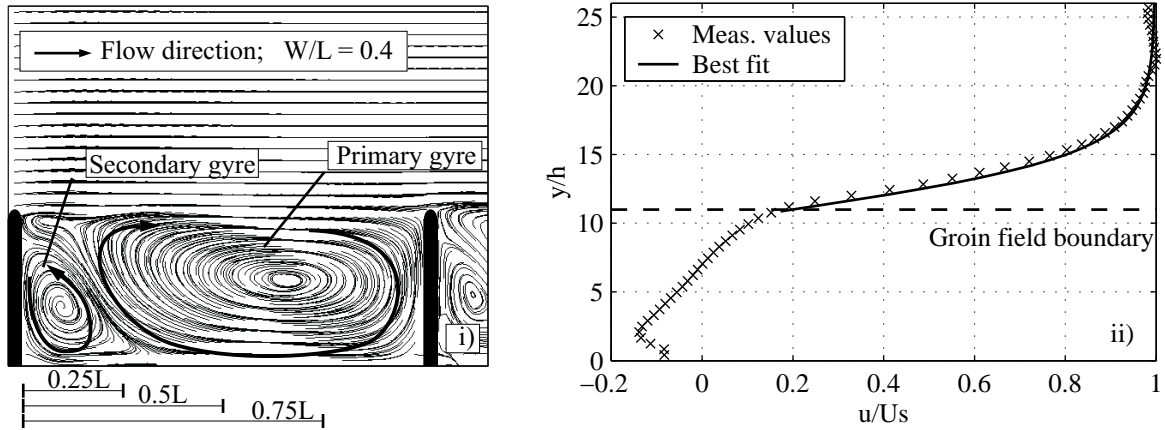


Figure 5.1. Mean flow characteristics; i) Streamline plot of the reference case; ii) Velocity profile of the u -component averaged over the length L of the groin field normalized with the maximum velocity at the water surface U_s . In addition, an approximation of the velocity profile with a hyperbolic tangent function is plotted. The horizontal dividing line indicates the position of the groin heads.

In the reference case the different parameters are determined to be: $a = 0.82$, $b = 0.24$ and $c = 0.17$. This represents the velocity profile that is responsible for the stretching mechanism of a tracer cloud in the main stream.

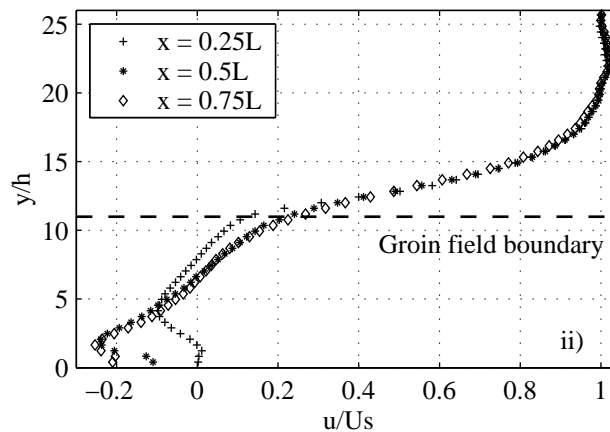


Figure 5.2. Normalized velocity profiles of the u -component at $x = 0.25L$, $0.5L$ and $0.75L$ (figure 5.1, i).

Figure 5.2) shows, that the shape of the velocity profile over the complete length of the groin field in the main stream is almost constant. This indicates, that the mixing layer between dead-water zone and main stream is already fully developed. There is a major difference to the experiments that have been conducted by Westrich (1978) and Booij (1989) where only one dead-zone has been implemented into the flow.

Booij (1989) and Westrich (1978) showed that the maximum velocity in the recirculating flow of the dead-water zone is about one third of the mean velocity. In our case this relation is slightly smaller, i. e. about 25 % of the mean velocity (at $u'/U = -0.25$,

$y/h = 2$ in figure 5.2), which corresponds to the value that has been found by Lehmann (1999) for groin field flows. The difference can be explained by the width of the upstream boundary layer (figure 5.3), which in the case of a single groin field is a regular wall boundary layer and not a fully developed mixing layer as in the case of groin fields. The regular wall boundary layer is smaller in width (figure 5.3) which leads to velocity gradients that are steeper and, therefore, to a larger momentum exchange. The final results are higher velocities in the dead-water zone compared to the expected velocities in a series of groin fields.

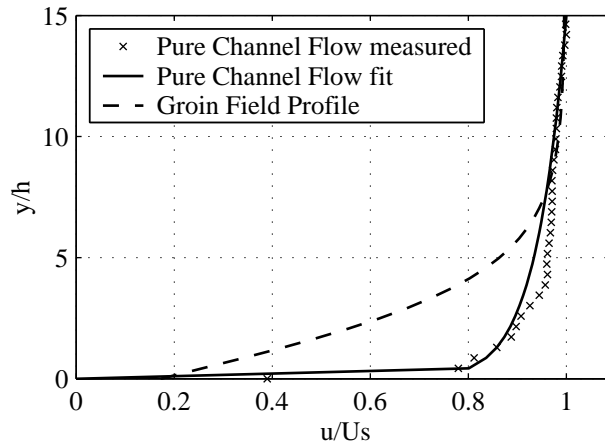


Figure 5.3. Comparison of the flow profile in the case of groin fields and in the case of a regular wall flow where the wall consists of glass. In the case of groin field flow $y/h = 0$ indicates the groin head, in the case without groins $y/h = 0$ indicates the channel wall.

In figure 5.3 the velocity profile in the mixing layer of the groin field flow is compared to the velocity profile of the channel wall boundary layer that has been measured in the same flume under the same flow conditions with a glass wall. That means, pure channel flow has been measured without groins. Only the discharge has been adapted to compensate for the larger cross-sectional area of the flow compared to the groin field flow. The flow distribution of pure channel flow has been approximated with the following power function

$$\frac{u}{U_s} = \left(\frac{y/h}{\delta} \right)^{\frac{1}{16}} \quad (5.2)$$

where δ is set to 15. The exponent $1/16$ arises because of the smooth glass walls that lead to a thin boundary layer and therefore, to a flat flow profile.

Already 80% of the main stream velocity are reached after one water depth in y -direction in the case of pure channel flow. The groin field mixing layer needs about four water depths of the groin heads to reach 80% of the main stream velocity.

Turbulent flow properties. In figure 5.4 and 5.5 the turbulence intensities are plotted which are defined as the ratio between Root-Mean-Square(RMS)-velocities and the shear flow velocity u_* . The RMS-velocities u' and v' are determined by

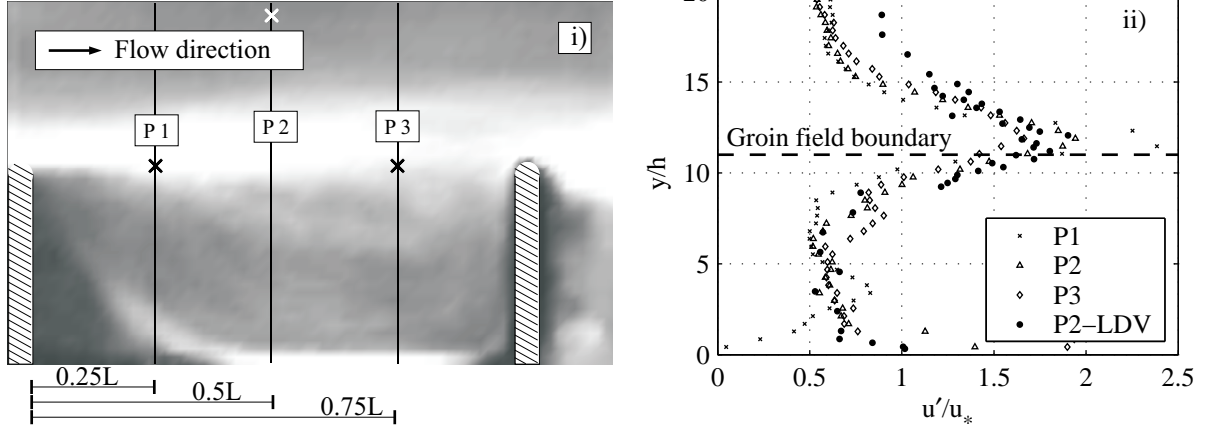


Figure 5.4. i) Intensity of the velocity fluctuations in x-direction (light colors indicate higher intensities), \times indicates the positions of vertical velocity profiles as given in figure 5.7 and 5.8; ii) RMS-velocity profiles P1, P2 and P3 at $x = 0.25L$, $0.5L$ and $0.75L$, normalized with the mean shear velocity u_* in the main stream. In addition the result of the LDV measurement taken at $x = 0.5L$ is plotted.

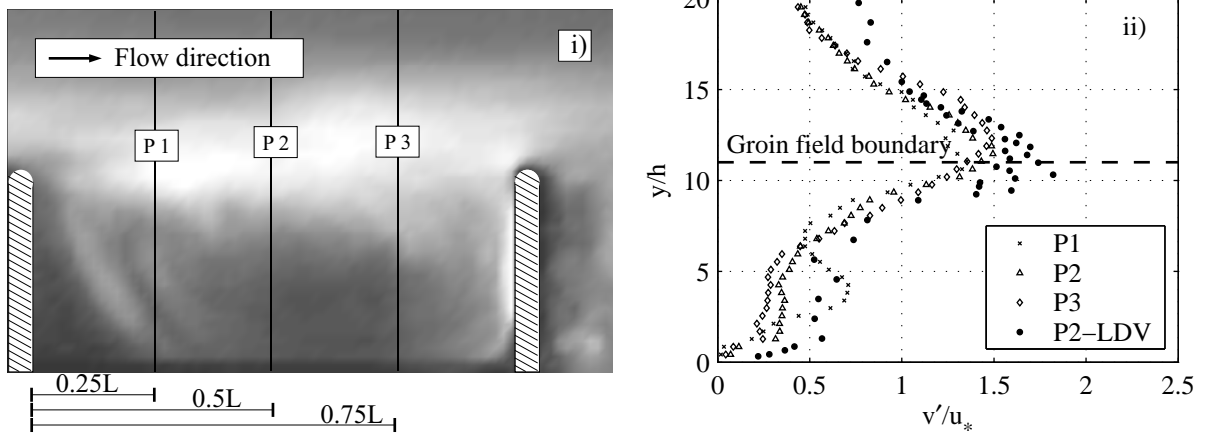


Figure 5.5. i) Intensity of the velocity fluctuations in y-direction (light colors indicate higher intensities); ii) RMS-velocity profiles P1, P2 and P3 at $x = 0.25L$, $0.5L$ and $0.75L$, normalized with the mean shear velocity u_* in the main stream. In addition the result of the LDV measurement taken at $x = 0.5L$ is plotted.

$$u' = \frac{1}{n-1} \sum_{i=1}^n \sqrt{(U-u)^2} \quad (5.3)$$

and u_* is given by $u_* = \sqrt{ghI}$, which in the present case is 1.2 cm/s. These values characterize the intensity of the velocity fluctuations and are indicative for the turbulent diffusive mass transport. Figure 5.4 and 5.5 show clearly that the peak of the turbulence intensities can be found in the mixing layer between dead-water zone and main stream at approximately one water depth from the groin heads into the main channel. The maximum of u'/u_* is about 1.8 and herewith slightly larger than the transverse component v'/u_* of about 1.5. An interesting behavior of the u' -profile P2 and P3 are the increasing values in the dead-zone close to the channel wall, which is an effect of the wall shear layer. The

profile P1 at $x = 0.25L$ does not show this behavior because here the profile leads through the secondary gyre (figure 5.1, i) where the flow velocities are much smaller.

Figure 5.4 shows, that the behavior of u' in the mixing layer remains almost constant in x-direction, which supports the conclusions from the mean flow profiles. The results for v'/u_* are slightly different. Here, the turbulence intensity is increasing with the distance from the upstream groin (figure 5.5, i). The results from the surface PIV -measurements could be confirmed through the accompanying LDV measurements in the regions of the mixing layer and in the dead-water zone. In regions where the velocity fluctuations are dominated by small scale fluctuations like in the undisturbed main channel flow, the LDV results deviate significantly from the PIV -measurements because of the limited spatial and temporal resolution of the PIV setup. The same problem can be observed close to groin heads. LDV measurements showed that the maximum v'/u_* -values, close to the groin heads are of order 1.4.

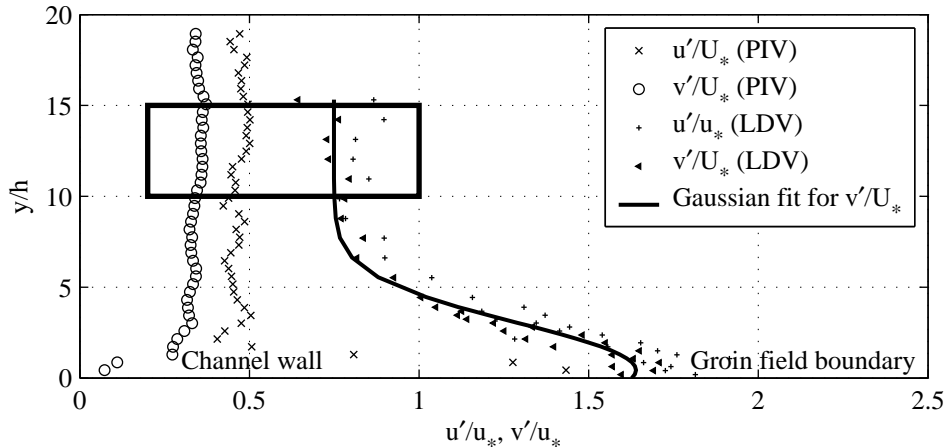


Figure 5.6. Turbulence intensity, measured with PIV in undisturbed channel flow compared with the LDV measurements and a Gaussian fit for v'/u_* . For the PIV measurements $y/h = 0$ indicates the position of the groin field head in the case of the LDV measurements, in the case of the PIV measurements, $y/h = 0$ indicates the channel wall. The box region indicates the undisturbed flow in the main channel where both measurements are comparable with the reference values taken from Nezu & Nakagawa (1993) given in table 5.1.

Due to the fact that the measurement area in figure 5.4 and 5.5 was restricted to $y/h = 20$, additional PIV -measurements have been performed in undisturbed channel flow to avoid influences of the mixing layer. In figure 5.6 the resulting turbulence intensities, measured with PIV and LDV, are compared in cases of undisturbed channel flow. The values from the region of undisturbed channel flow, which are highlighted in the rectangular box in figure 5.6, are summarized in table 5.1, together with reference values taken from Nezu & Nakagawa (1993).

As already mentioned, the error resulting from the PIV technique increases in the region of the undisturbed channel flow. The limited spatial and temporal resolution filters turbulent movements in these regions, which are not negligible. The deviation from the

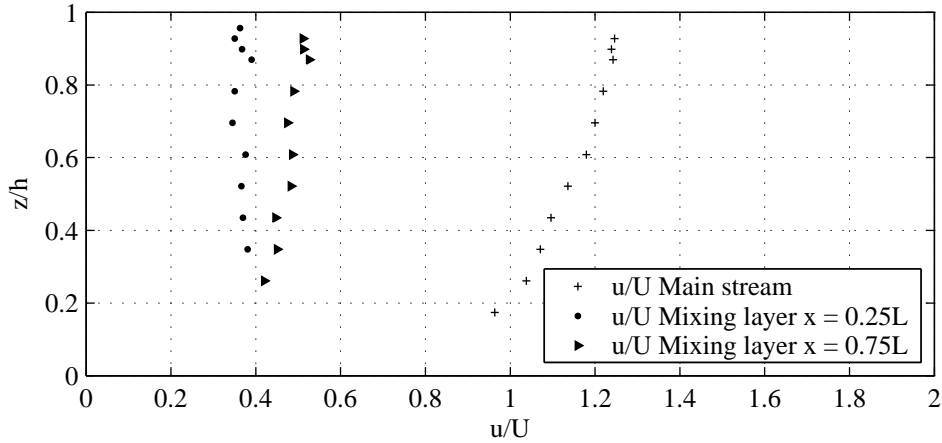
Table 5.1. Comparison of measured turbulence intensities in the undisturbed channel flow with reference values taken from Nezu & Nakagawa (1993)

	PIV present study	LDV present study	Reference value Nezu & Nakagawa (1993)
u'/U_* at the water surface	0.33	0.70	0.60
v'/U_* at the water surface	0.45	0.80	0.90

LDV results to the reference values, can partly be explained by difficulties in the determination of U_* in the experiment. The channel slope was determined as 0.00032, which means that the elevation difference between inlet and outlet of the flume is about 6 mm. The measurement accuracy of about 0.2 mm can lead to the observed deviations. However, in the present study the exact value is much less important than the actual shape of the distribution, which is used later to scale the turbulent diffusivity in transverse direction. In figure 5.6 the lateral distribution of the turbulence intensity of the transverse component has been approximated using a Gaussian curve (figure 5.6) of the form:

$$\frac{v'(y)}{u_*} = 0.75 + 0.93 \exp \left[-0.5 \left(\frac{y/h - 0.17}{2.74} \right)^2 \right] \quad (5.4)$$

Velocity distribution in the vertical. With the used PIV technique it is not possible to get information about the velocity distribution in vertical direction. Therefore, vertical velocity profiles have been measured using LDV, at two positions in the mixing layer ($x = 0.25L$ and $0.75L$) and in the undisturbed channel flow (figure 5.7). This information helps to interpret the results obtained at the water surface with respect to the depth averaged behavior of the flow.

**Figure 5.7.** Vertical velocity profiles of the u -component in the main channel and in the mixing layer, normalized with the mean velocity in the main channel $U = Q/A_S$. The position of the measurements are indicated in figure 5.4.

In figure 5.7 it can be seen, that the vertical velocity profile in the undisturbed channel flow, can be interpreted as a fully developed velocity profile of turbulent open channel

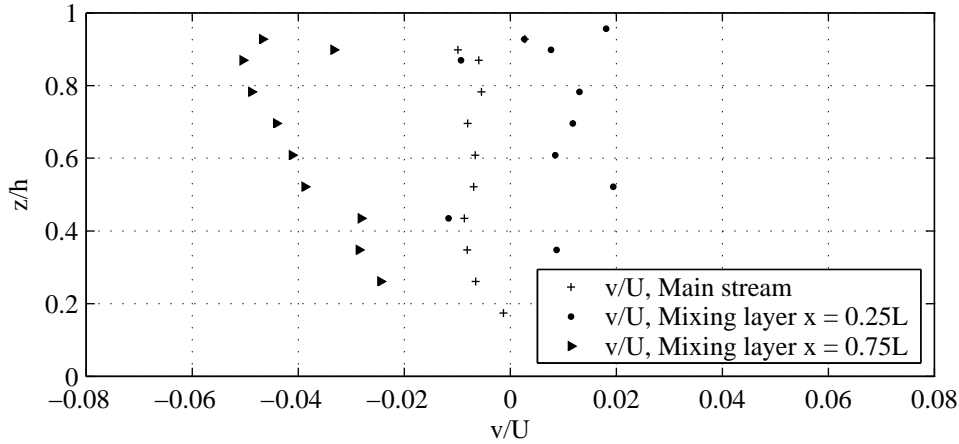


Figure 5.8. Vertical velocity profiles of the v -component in the main channel and in the mixing layer, normalized with the mean velocity in the main channel $U = Q/A_S$. The position of the measurements are indicated in figure 5.4.

flow. The profiles in the mixing layer are more homogeneous, which is typical for flow regions that are disturbed by large coherent motions in the horizontal plane. The velocity profile in the main channel (figure 5.7) shows that here the velocities are much larger than the cross-sectional averaged velocity U . The width of the mixing layer reduces the area of undisturbed channel flow, which means that the depth averaged velocity increases in this region.

The transverse velocity component in the vertical in the main stream is almost zero over the complete depth of the flow. In the mixing layer at $x = 0.25L$ the net flux is slightly positive, which means that on average the flow is directed from the dead-water zone into the main channel. At $x = 0.25L$ no clear tendency from water surface towards the channel bottom can be observed. At $x = 0.75L$ a net flow into the dead-water zone could be measured, which is stronger at the water surface than near the channel bottom. It has to be stated that in the mixing layer the LDV measurements are influenced by the small surface waves that emerge at the groins. This explains the large scatter of the data, especially at $x = 0.25L$.

Transverse velocities in the mixing layer. The mass exchange between dead-water zone and main stream is driven by flow velocities across the groin field boundary, which is the connecting line from groin head to groin head.

In figure 5.9 a velocity profile ($W/L = 0.4$) is plotted along the groin field boundary. Positive values indicate velocities that are directed from the dead-water zone into the main channel, negative values indicate velocities in the opposite direction. According to figure 5.9 on average mass travels from the dead-water zone into the main channel in the first $1/3$ of the dead-water zone. The maximum velocity in this region is about 13 % of the mean flow velocity in the main channel. The mass flux in the opposite direction is located in the following $2/3$ of the length of the dead-water zone. Here, the measured

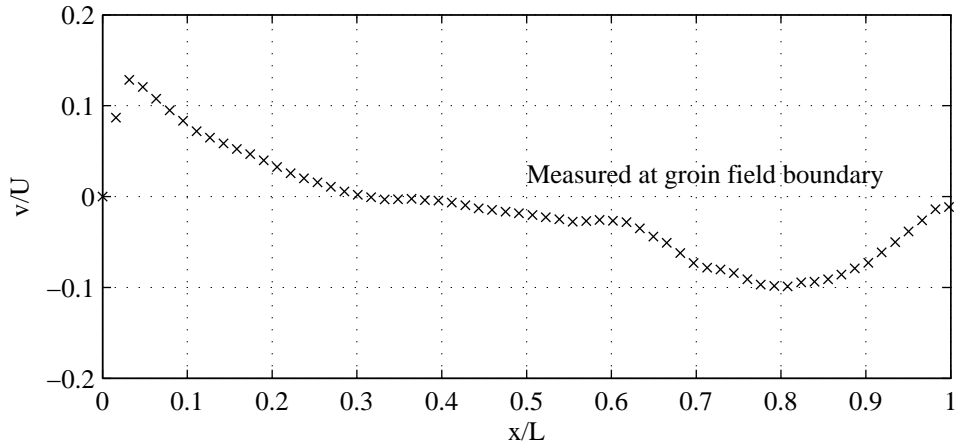


Figure 5.9. Time averaged velocities in transverse direction along the connection line between two groin heads.

mean velocities are about 10 % of the mean flow velocity, thus smaller than in positive y-direction.

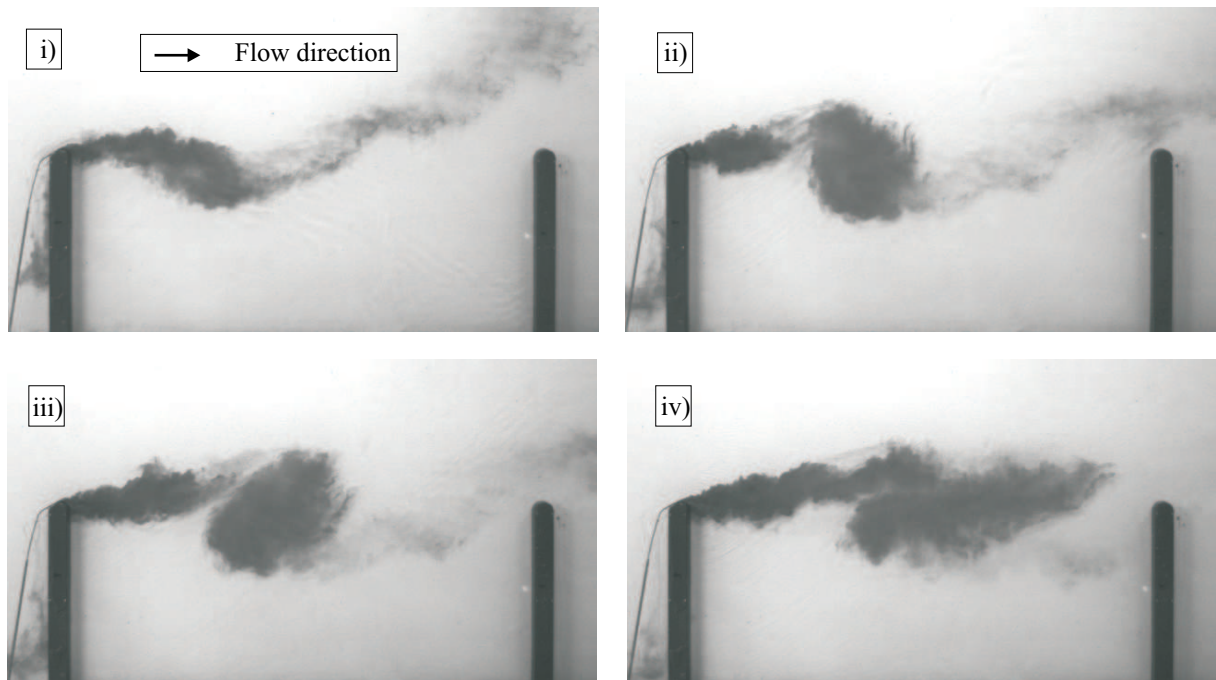


Figure 5.10. Visualization of the coherent flow structures that emerge at the groin head and grow during their travel through the mixing layer. Δt between two pictures is 1s.

Flow structures in the mixing layer. In figure 5.10 the flow pattern in the mixing layer of the reference case has been visualized with the help of food dye. At the upstream groin, horizontal eddies are generated (figure 5.10), and then advected downstream. During their

travel through the mixing layer they grow, due to the mean velocity shear that has been plotted in figure 5.1.

By analyzing the vorticity fields (figure 5.11) it can be seen, that these structures can either travel into the dead-water zone when they reach the downstream end of the groin field or they are just advected further downstream to the next dead-water zone. It is also possible that they break up, so that they just partly travel into the groin field. Figure 5.11 shows a clockwise rotating structure passing the downstream groin without any exchange.

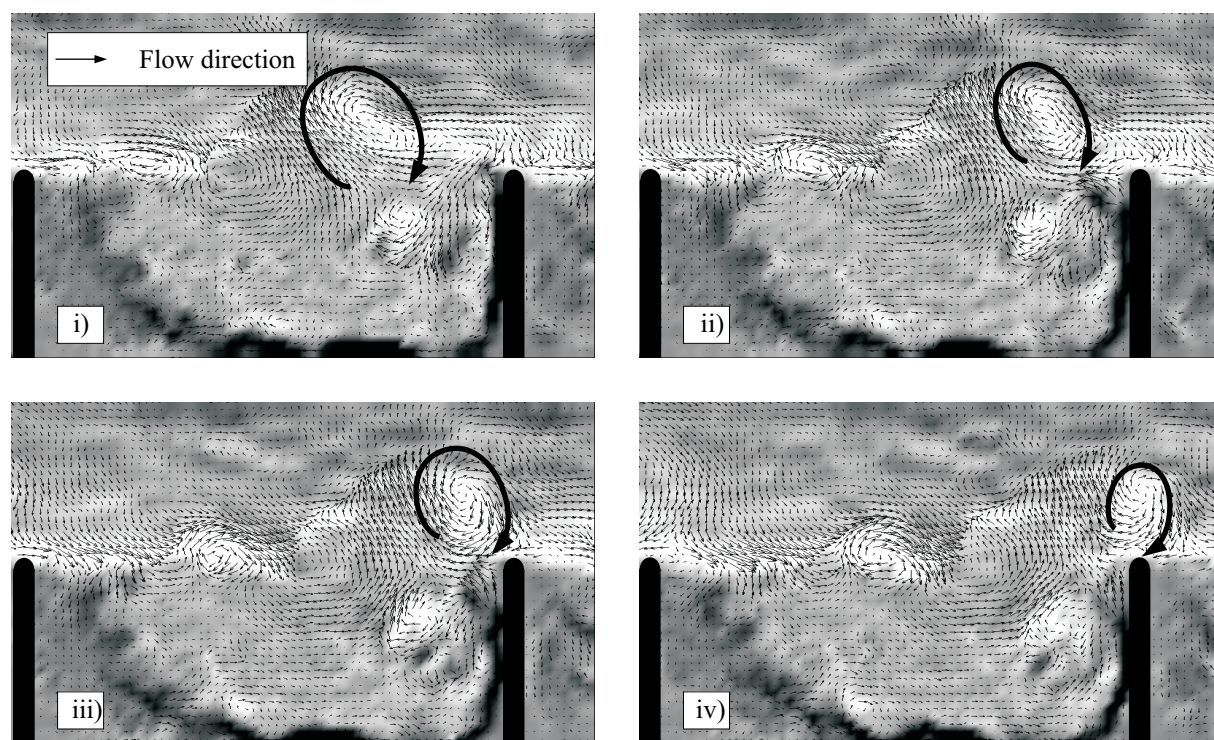


Figure 5.11. Visualization of the coherent flow structures with the help of the vorticity and the instantaneous velocity deviation from the mean velocity. Δt between two pictures is 1s. Light color indicates clockwise rotation and dark color anticlockwise rotation.

These measurements demonstrate that the time and spatial resolution of the PIV system is sufficient for detecting the driving mechanism for the mass exchange between dead-water zone and main stream. The frequency of these coherent motions could be determined to be of the order of 10 seconds.

5.1.2 Influence of the groin field aspect ratio W/L

The influence of the aspect ratio W/L on the flow pattern has been investigated within the measurement series No. 1-8 (table 4.2). The aspect ratio was varied from 3.35 (which indicates very narrow dead-water zones) to 0.35 (where the dead-water zone is more elongated). All the other parameters are identical to the reference case No. 2.

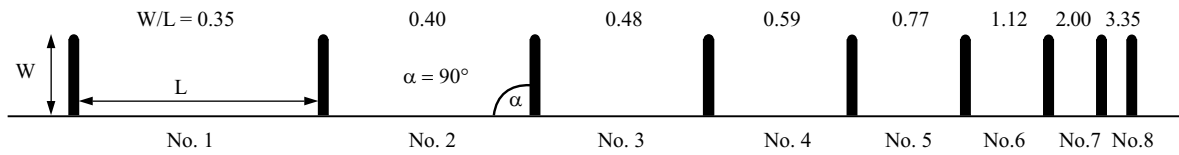


Figure 5.12. Schematic sketch of the series No. 1-8 from table 4.2 with changing W/L aspect ratio.

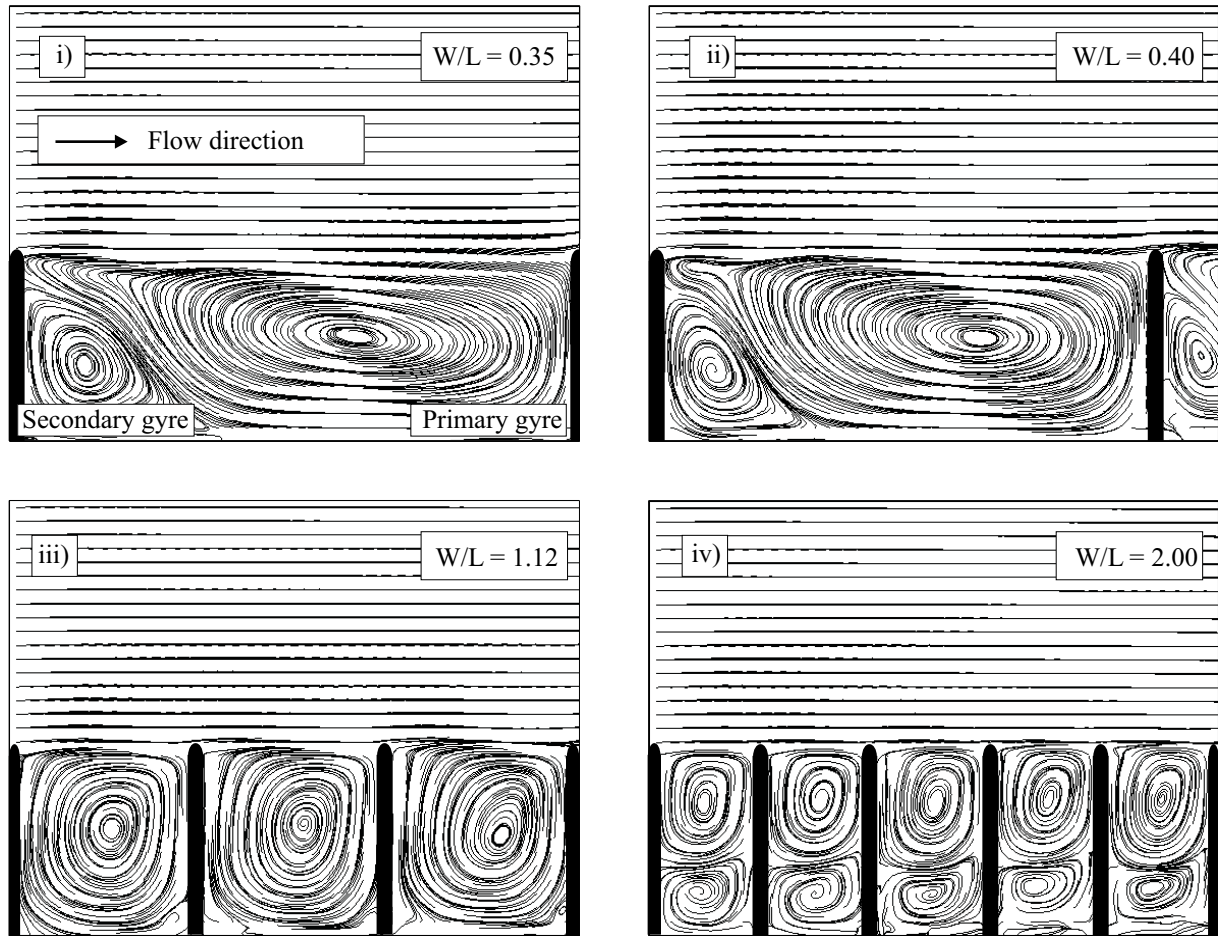


Figure 5.13. Mean flow properties in groin field flows with different W/L aspect ratios, where the three different possibilities of 1- and 2- gyre systems are visible.

In figure 5.13 the mean flow properties in dependence on the aspect ratio is visualized with the help of streamlines. The recirculation zone can be seen as well as the typical two gyre system. Hereby, three different cases can be distinguished that correspond to the results of Westrich (1978) and Booij (1989):

- 1) $W/L < 0.5$, figure 5.13, i-ii)

This is the typical case for groin fields in rivers, where the shape of the dead-water zone is elongated it longitudinal direction and a two gyre system can develop.

2) $0.5 < W/L < 2$, figure 5.13, iii)

In this case only one dominating gyre can be found in the dead-water zone that can have the shape of an ellipse with the ratio between the two axes at maximum 1.5 (Booij 1989).

3) $W/L > 2$, figure 5.13, iv)

In this case at least two gyres can be found in transverse direction (Booij 1989, Westrich 1978). The first gyre is driven by the mixing layer between dead-water zone and the main stream while the following gyres get their energy through additional mixing layers that exist between two gyres.

With respect to mass exchange between dead-water zone and main stream this differentiation is important, because mass that resides in the secondary gyre is exchanging much more slowly than the mass in the primary gyre. Hereby, a primary gyre is defined as recirculating water body that has a direct contact area with the main stream. The secondary gyre has a contact area only to a primary gyre and direct mass exchange with the main stream is therefore not possible.

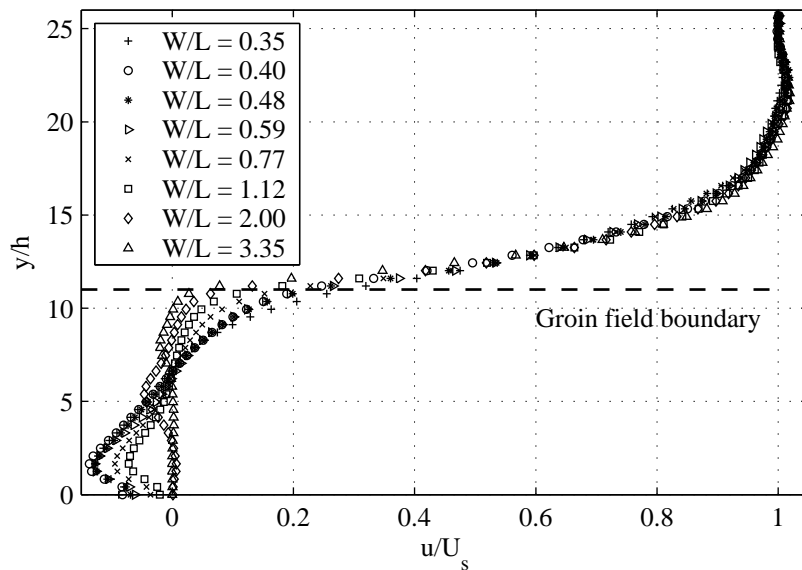


Figure 5.14. Comparison of the mean velocity profiles for the different W/L aspect ratios corresponding to the cases No. 1-8 from table 4.2. Hereby the velocities are averaged in space over the length L of the groin fields, and normalized with the maximum velocity at the water surface U_s .

In figure 5.14 the mean velocities for the different W/L cases are compared. The comparison shows, that the aspect ratio of the groin fields has limited influence on the mean flow properties in the main stream. Above the groin field boundary, no significant differences between the normalized velocity profiles can be observed. With respect to mass transport this result supports the assumption that there are no strong variations of the stretching rate in the main channel as a function of aspect ratio.

The time-averaged u-component of the flow velocity in the dead-water zone, is strongly affected by the geometry. In the very narrow cases $W/L = 3.5$ the velocities are close to zero, whereas in the elongated cases $W/L = 0.35$ velocities up to 15% of the maximum velocity at the water surface occur. The time needed for a particle to return to the mixing layer after its transfer into the dead-water zone can, therefore, be much longer in the narrow case. This means that the retention time in the narrow case is larger than in the elongated case.

In figure 5.15 the transverse component of the turbulence intensities is plotted for the different aspect ratios W/L . The turbulence intensity does not deviate strongly in the elongated cases with $W/L = 0.35, 0.4$ and 0.48 , respectively, and therefore represent quite well the reference case. If the W/L ratio gets larger, the velocity fluctuations in the mixing layer are smaller. One reason for this behavior is the decreasing length of the mixing layer that determines the development of the coherent flow structures. In cases of very narrow dead-water zones these structures cannot fully develop in size, leading to a limited length scale of the fluctuations which can again lead to resolution problems in this area.

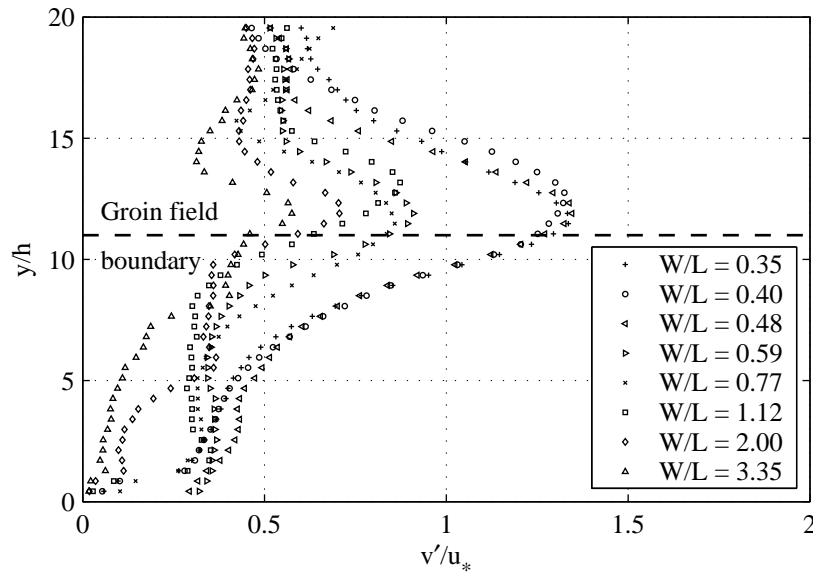


Figure 5.15. Comparison of the normalized RMS-velocities v' for the different W/L aspect ratios corresponding to the cases No. 1-8 (table 4.2).

5.1.3 Influence of the inclination angle

In section 2.2 it has been shown that in natural rivers groins can be built with a certain inclination angle α that differs from 90° (figure 5.16). Groins that are inclined against the flow $\alpha < 90^\circ$ are much more often used than groins with $\alpha > 90^\circ$ (section 2.1). In the

present study inclination angles of 64° and 116° are analyzed for W/L aspect ratios of 0.4 and 1, respectively.

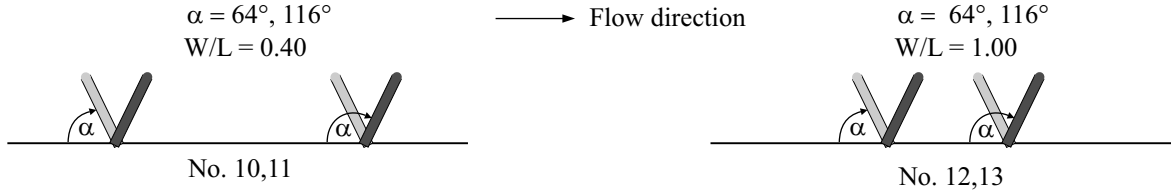


Figure 5.16. Schematic sketch of the series No. 10-13 with forward and backward inclined groins (table 4.2).

In figure 5.17 the mean flow behavior observed in series No. 10 and 11 with varied inclination angle is visualized with the help of streamlines, where W/L is 0.4. Compared to the reference case, the only difference is the proportion of primary and secondary gyres, respectively. If the groins are inclined against the flow, the secondary gyre gets smaller and is almost negligible at $\alpha = 64^\circ$. In contrast, the secondary gyre enlarges, if the groins are inclined with the flow. As the secondary gyre is rotating much slower, mass exchange in this region of the dead-water zone is also much slower. Hence, the retention time in groin fields with an inclination angle larger than 90° is expected to be longer than in the other case.

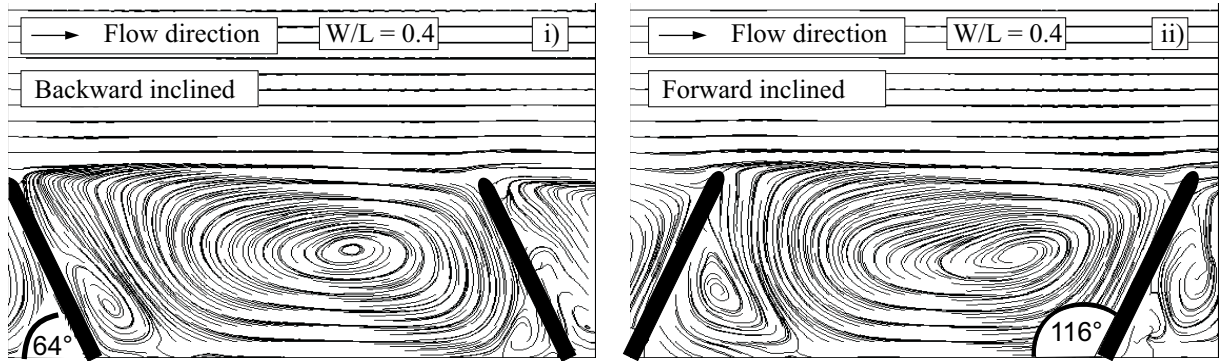


Figure 5.17. Mean flow properties in groin field flows with different inclination angle α ; i) backward inclined groins with $\alpha = 64^\circ$; ii) forward inclined groins where α is 116° .

The same result could be observed in the case with W/L is 1.0 (experiments No. 12 and 13). In the case of backward inclined groins, the one gyre system of the regular case with groins perpendicular to the flow turns into a two gyre system. Therefore, again, the mass exchange is less pronounced when the groins are forward inclined.

In figure 5.18 the transverse components of the RMS-velocities v'/U_* are visualized. Groins which are inclined backward ($\alpha = 64^\circ$) enhance turbulent motion in the mixing layer. Here, maximum values of 1.7 can be found, which are slightly larger than in

the reference case. Maximum values of 1.5 are found, if the groins are inclined forward, which is similar to the reference case. The same tendency could be observed in the cases No. 12 and 13 ($W/L = 1.0$).

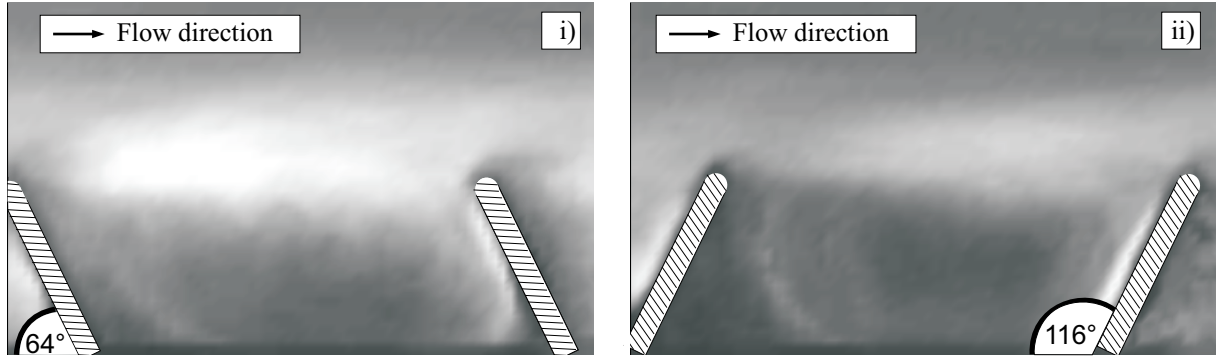


Figure 5.18. Transverse turbulent intensity v'/u_* , where dark regions indicate low values and bright regions indicate the maximum values. In the left figure (i) the maximum value is 1.7 and in the right figure (ii) it is 1.5.

5.1.4 Submerged groins

As has been mentioned in section 2.1, groins are usually submerged if the discharge in a river is larger than the annual mean discharge. In that case the flow pattern changes dramatically, which means that the flow is no longer two-dimensional and therefore it is not possible to describe the complete flow field using surface PIV. If the water depth is much higher than the groin height, the groins can be seen as roughness elements on the channel bottom, which create extra flow resistance and turbulence. If the groins are only slightly submerged, the flow pattern can be similar to the non-submerged case because the flow in the groin field is still dominated by the momentum exchange with the main stream. In figure 5.19 the results of the surface PIV are shown where the water depth is 18% larger than the height of the groins.

The main difference relative to the non-submerged case are size and shape of the primary and secondary gyre, which are now influenced by the flow over the groins. In the presented submerged case the primary gyre covers only 50% of the dead-zone volume, compared to 85% in the non-submerged case. The secondary gyre is not a closed recirculating system any more and it is connected to a region of a vertical recirculation in the upstream part of the dead-zone. In this case the secondary gyre has a direct contact area with the main channel, which bends the flow in this region strongly into downstream direction. The vertical recirculation behind the groins covers about 15% of the dead-water zone.

Because of the water flowing over the groins the gradients of the mean flow profile are smaller, which means that the mixing layer width is larger than in the non-submerged case. This effect also influences the fluctuating part of the velocities. The amplification of

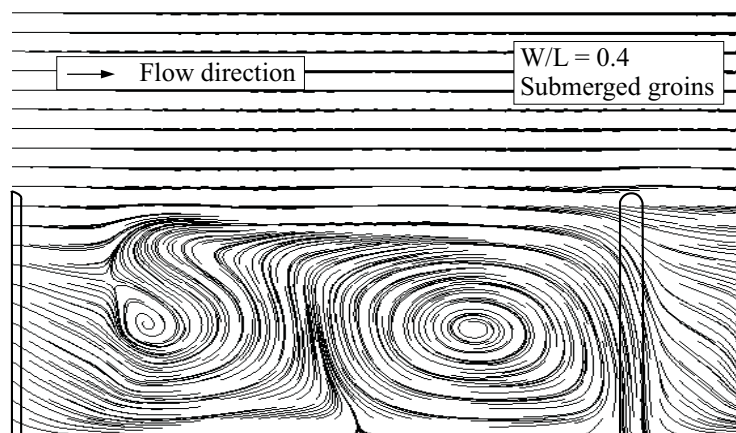


Figure 5.19. Mean flow properties at the water surface in case of submerged groins, series No. 9, where the water depth in the main stream is 18% larger than the height of the groins.

the RMS-velocities in the region of the mixing layer is less pronounced in the submerged case as compared to the reference case.

5.1.5 Influence of groin length

Experiments No. 14-16 have been performed with groins of half the length of the reference case, which leads to dead-zone volumes that are decreased to 25%, if the aspect ratio W/L is kept constant. Using these short groins allows to investigate aspect ratios down to 0.17 (No. 14).

In figure 5.20 the mean flow patterns are shown for the three different series, together with the intensity of the velocity fluctuations. It can be observed that the flow pattern of experiments No. 16 with aspect ratio $W/L = 0.4$ is very similar to the reference case with the same aspect ratio. A small deviation from the reference case can be noted for the size of the secondary gyre that covers about 20% of the dead-zone volume for case No. 16 compared to 15% for the reference case. This can be explained with the influence of the bottom friction. In the case of short groins the area of the bottom that influences the recirculating flow in the dead-zones is much smaller than for longer groins. In regions of low Reynolds numbers the bottom friction influences the rotating flow more strongly, therefore the secondary gyre in the case of short groins is comparably less damped by bottom friction than the secondary gyre in the reference case. The turbulence intensities in the case of small groins are significantly smaller than in the reference case (figure 5.5), which indicates that the groin field length L determines the development of the flow characteristics in the mixing layer as long as the the groin field width is large enough to prevent an influence of the channel wall on the flow in the mixing layer.

In section 5.1.2 it was shown that the maximum length of a gyre in the groin field is 1.5 compared to its width. However, in series No. 14 (figure 5.20, i), this ratio is strongly exceeded. In this case, the mean flow pattern in the groin field is not well represented by the time averaged mean flow. The flow in the dead groin field consists of a system of

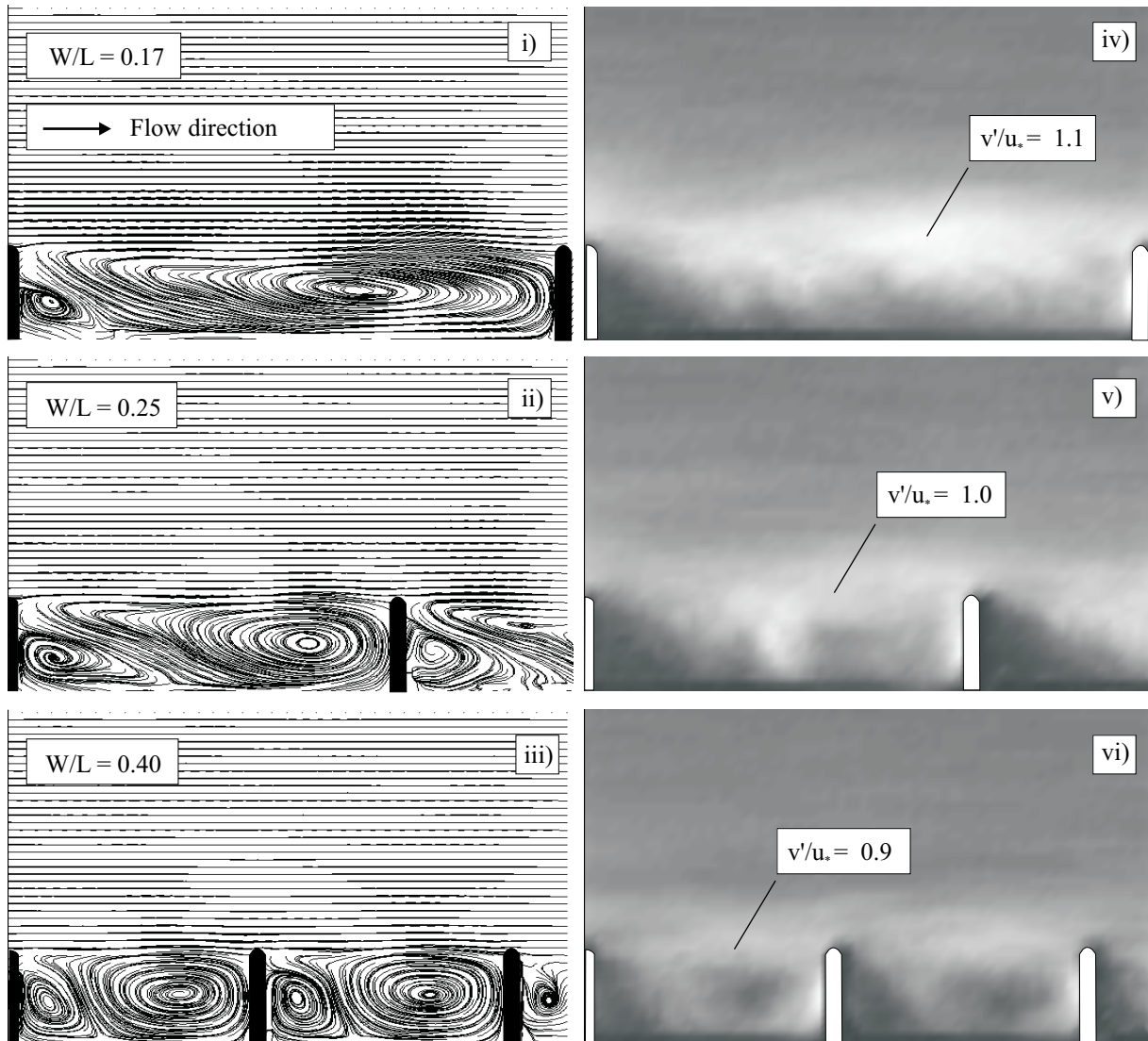


Figure 5.20. i),ii) and iii), show the mean flow pattern at the water surface in case of short groins, series No. 14-16; iv),v) and vi) show the turbulence intensity v'/u_* .

several gyres rotating in the same direction that change their position continuously. The instantaneous flow fields in figure 5.21 show three gyres that travel back and forth in the groin field. This behavior also effects the transverse flow component in the main channel. Regions of high flow velocities in y -direction can change their position. This has long been recognized as a negative influence on navigation and should be avoided by choosing appropriate groin field spacing.

5.1.6 Influence of groin field volume

Experiments No. 17 and 18 have been performed for investigating the influence of the water depth in the groin field. In these setups the flow conditions are the same as in the

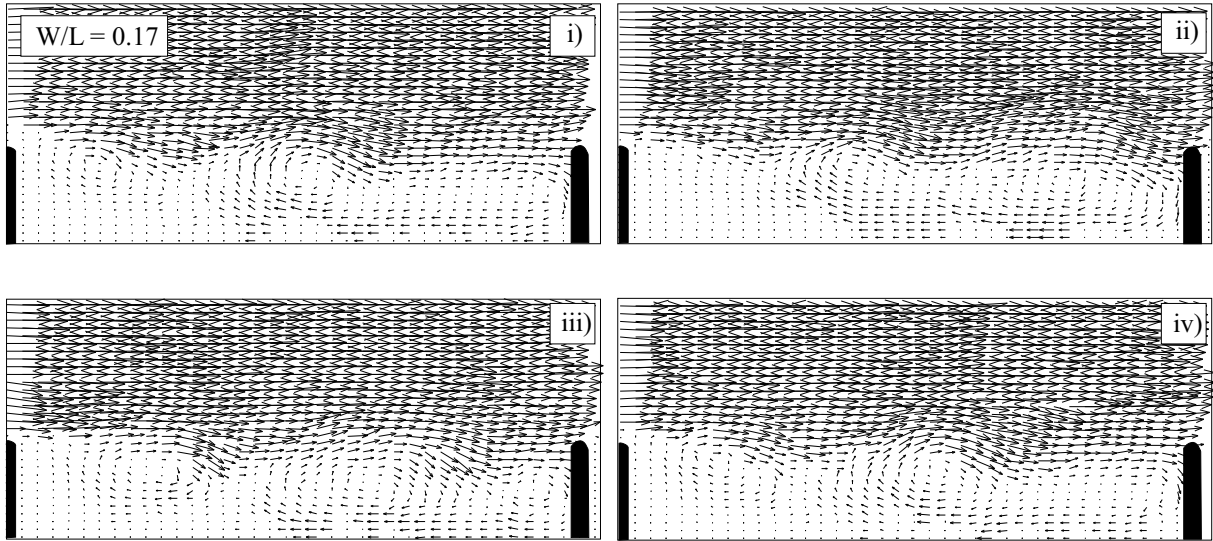


Figure 5.21. Instantaneous velocity fields in the case of short groins with an aspect ratio $W/L = 0.17$. Time interval between two velocity fields is 2 seconds.

reference case and also the aspect ratio W/L has been kept at 0.4. In experiment No. 17 (figure 5.22, i) the bottom in the groin field has a constant slope with a minimal water depth of zero at the channel wall and a maximum water depth equal to the main channel water depth at the interface between groin field and main channel. In experiment No. 18 (figure 5.22, ii) the water depth in the groin field is constant at half of the water depth in the main channel.



Figure 5.22. Schematic side view in streamwise direction of the experiments No. 17 and 18 where the dead-zone volume is reduced by 50% compared to the reference case.

It can be seen that the mean flow pattern in case No. 18 with constant water depth in the groin field is very similar to the reference case. A different behavior of the mean flow is given in case No. 17, where the bottom of the groin field is sloped towards the main channel. The secondary gyre covers much more of the dead-zone volume. Another difference to the reference case is the position of the center of the primary gyre, which is strongly shifted in the direction of the main channel.

As in both cases (No. 17 and 18) the water depth in the groin field is reduced, also the Reynolds number of the flow is significantly smaller than in the reference case. Especially

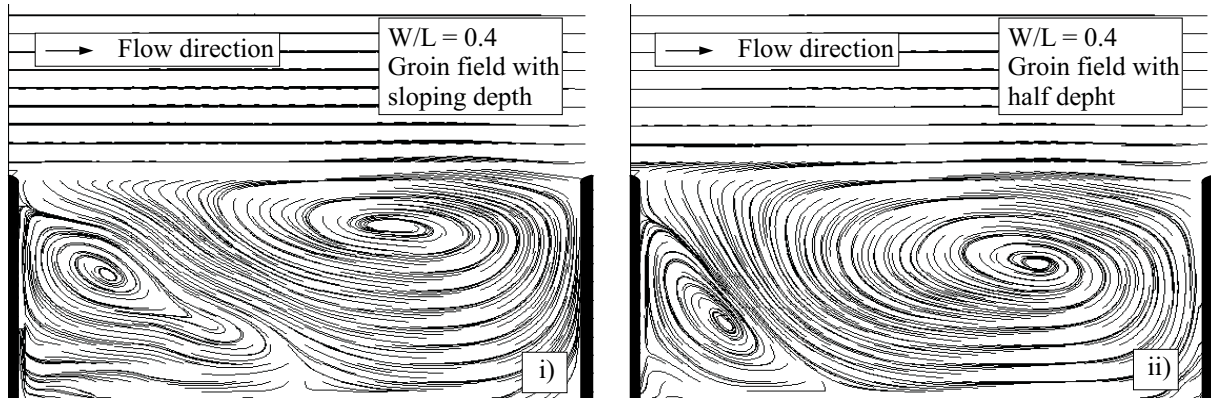


Figure 5.23. Mean flow pattern in the case of reduced groin field volume; i) Series No. 17 with sloping depth in the groin field, such that the water depth at the interface between dead-zone and main channel is the same in the main channel and zero at the channel wall; ii) Series No. 18, where the water depth in the groin field is only half the water depth in the main channel.

for the groin field with sloping depth (No. 17), the flow is partly laminar in the experiment (figure 5.24).

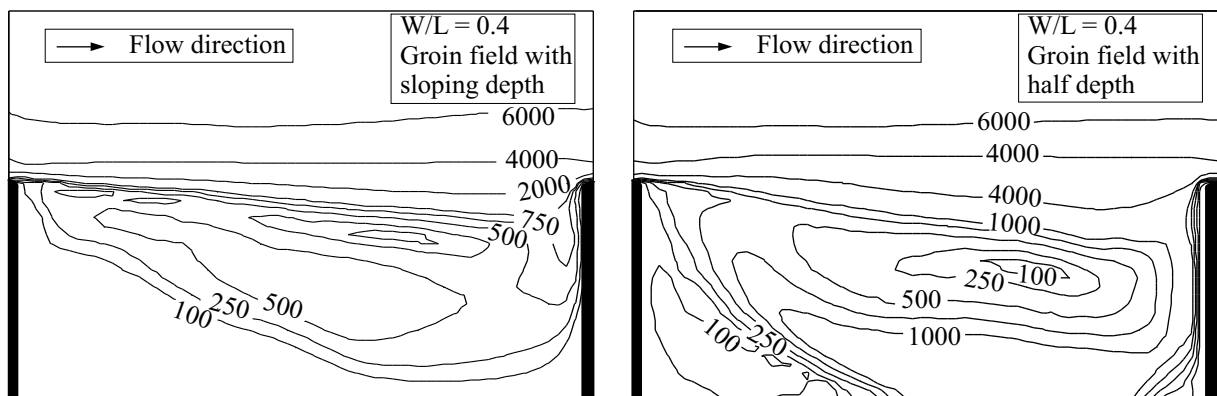


Figure 5.24. Top view on the groin field of experiment No. 17 and 18, showing the Reynolds Number based on the local surface flow velocity and the local water depth; i) Series No. 17 with sloping depth in the groin field; ii) Series No. 18, where the water depth in the groin field is only half the water depth in the main channel.

5.1.7 Exchange rates determined with surface PIV

Two approaches were used to determine the mass exchange rates between main channel and dead-water zone in the present study: An indirect method using the instantaneous velocity fields and a direct method using depth averaged concentration measurements. In this section the results from the indirect method using the surface PIV data are presented. The exchange rates obtained with the direct method are presented in the following section

and the discussion about differences and the possible interpretations can be found in section 5.3.

Basically, turbulent mass transport is defined as the instantaneous velocity u' multiplied with the instantaneous concentration c' . If we assume an almost homogeneous concentration distribution, the mass transport is mainly determined by the instantaneous velocity. Defining the dead-zone region as the volume within the groin field boundary, which is the line between groin head and groin head, the time needed for a complete exchange of the water volume, which is equivalent to the mean residence time T_D is defined as follows

$$T_D = \frac{V_D}{Q_{out}} \quad (5.5)$$

V_D is the volume of the dead-water zone and Q_{out} stands for the mass flux from the dead-water zone into the main stream. Equation 5.5 says that after T_D all volume has been washed out into the main channel. During the time T_D the same amount of fresh water flows from the main stream into the dead-water zone, due to continuity. That means, during T_D two times the volume V_D has to be transported across the interface between dead-water zone and main stream. With $V_D = h_D L W$ and $Q_{out} = E_{out} h_E L$ equation 5.5 leads to

$$T_D = \frac{W}{E_{out}} \frac{h_D}{h_E} \quad (5.6)$$

Normalization with the main stream velocity U and the width of the groin field W leads to the dimensionless exchange coefficient k as has been defined in 3.71

$$k = \frac{E_{out}}{U} \frac{h_E}{h_D} \quad (5.7)$$

With the help of the PIV measurements it is possible to determine the exchange velocity E_{out} directly. By taking the norm of the transverse velocity component (figure 5.25) and integrating these instantaneous values along the groin field boundary, the overall flux crossing the groin field boundary is derived. Assuming that the flux into the dead-zone is equal to the mass flux out of the dead zone the instantaneous exchange velocity is given by one half of the result of this integration. The result divided by the groin field length L is the instantaneous specific volume flux E'_{out} leading to

$$E'_{out} = \frac{1}{2L} \int_0^L |E| dx \quad (5.8)$$

In the present study three time series of 200 velocity fields are taken for every setup. The time averaged exchange velocity E_{out} can therefore be determined by averaging over 600 values of E' corresponding to 600 time steps. The PIV measurements are taken at the water surface which means that in this case, the exchange coefficient k_{PIV} is determined by normalizing the exchange velocity with the main stream velocity at the water surface U_S .

$$k_{PIV} = \frac{E_{out}}{U_S} \frac{h_E}{h_D} \quad (5.9)$$

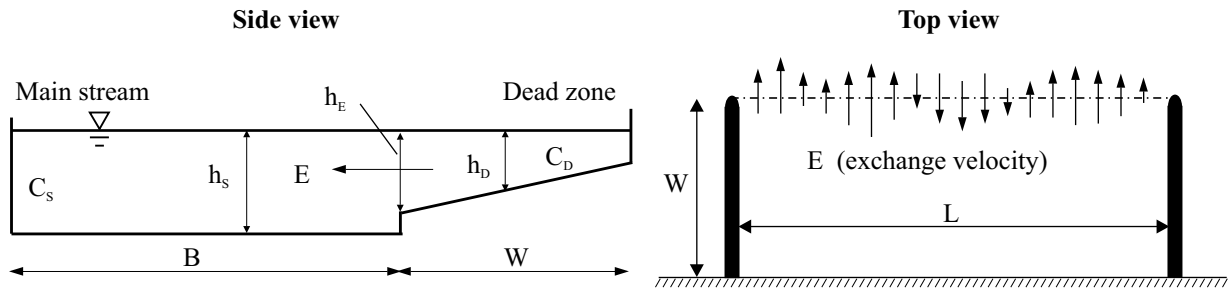


Figure 5.25. Cross-sectional of a river with dead-zone and a top view on a groin field with a schematic visualization of the instantaneous velocities at the groin field boundary.

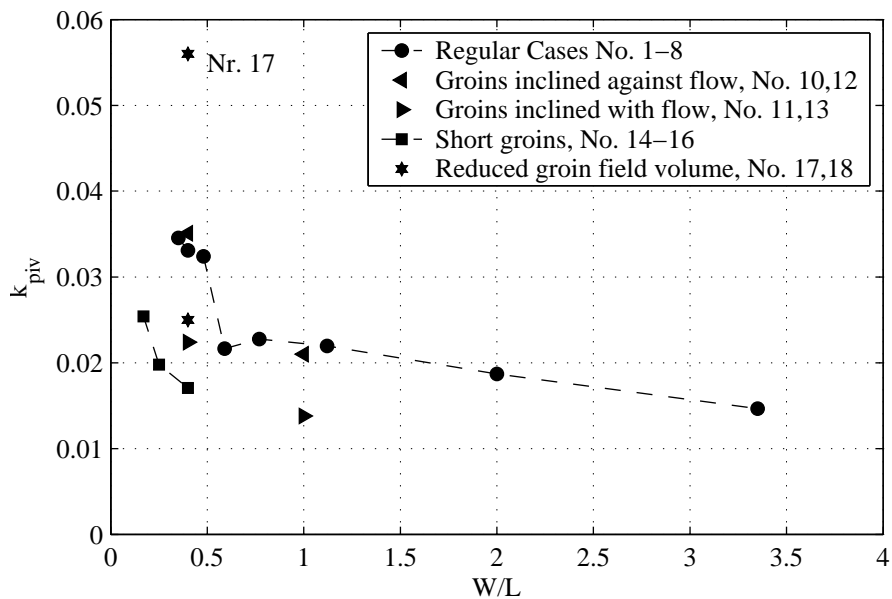


Figure 5.26. Dimensionless exchange coefficient k_{PIV} against the aspect ratio W/L .

In figure 5.26 the dimensionless exchange coefficient k_{PIV} is plotted depending on the aspect ratio W/L for the different experimental setups. The value of k decreases with increasing W/L , which means that the exchange coefficient is larger in the case of elongated dead-water zones. Backward inclined groins have almost no influence on the mass exchange. A different behavior can be observed with forward inclined groins. In this case the exchange coefficient is significantly smaller due to a sheltering effect of the groins. For short groins the same tendency can be seen: increased W/L leads to decreased mass exchange. However, the exchange values for the short groins are about 50% of the regular cases.

In series No. 18 with half water depth in the groin field the exchange is slightly decreased compared to the standard groin field. The resulting exchange coefficient for series No. 17 with sloping depth in the groin field is almost twice as high as in the case of the standard experiment. This result can be explained by the definition of k_{PIV} from equa-

tion 5.9. Series No. 17 represents the only experiment where the term h_E/h_D has to be taken into account, which is in this case a factor of two. Further discussion of the obtained k values can be found in section 5.3.

5.2 Measured concentration fields and exchange values

Concentration fields in the dead-zone after an instantaneous tracer injection have been measured with the help of the PCA technique described in section 4.3. The results are depth- and space-averaged concentration fields for the groin field at every time step.

In figure 5.27 the evolution of the concentration is plotted for the two series, where the time t is normalized with the mean residence time T_D and the concentration C with the initial concentration C_o . The time series for each setup can be approximated with an exponential decay of first order (section 3.4.1).

$$C(t) = C_o e^{-t/T_D} \quad (5.10)$$

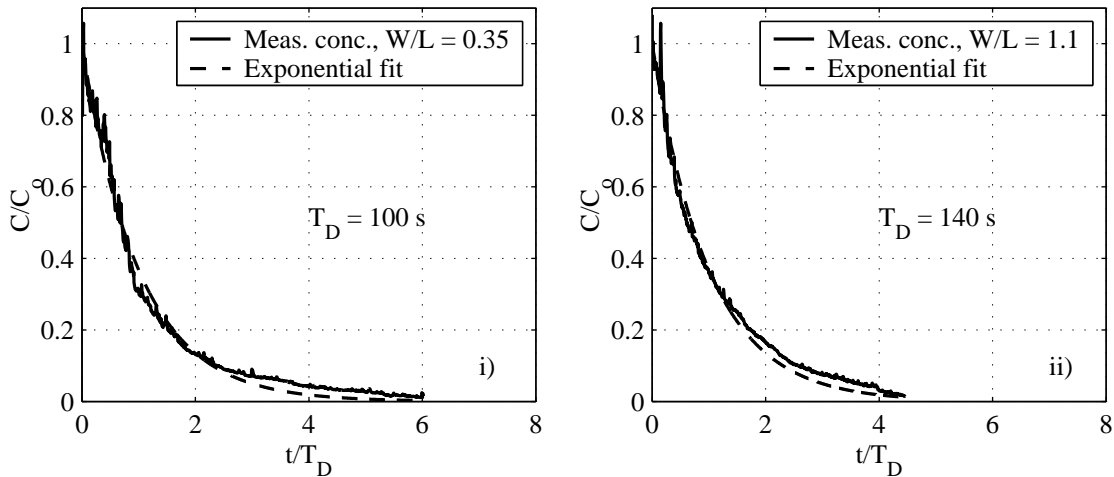


Figure 5.27. Measured concentration averaged over the total volume of the groin field and fitted exponential decay function; i) Experiment No. 1 with an aspect ratio $W/L = 0.35$, with a mean residence time T_D of 100 s; ii) Experiment No. 6 with an aspect ratio $W/L = 1.11$, with a mean residence time T_D of 140 s.

The residence time T_D is used later in chapter 6 to parameterize the influence of dead-water zones on the mass transport in the river. In the present case a non-linear least square method has been applied to find the best approximation of T_D . In section 3.4.1 it has been shown that T_D can be interpreted as the inverse of the exchange coefficient K_D , which can be normalized with the width of the groin field W and the main stream velocity U to give a dimensionless exchange coefficient k_{PCA} :

$$k_{PCA} = \frac{W}{T_D U} \quad (5.11)$$

Table 5.2. Measured exchange values k using the direct PCA method by analyzing the concentration fields. Series 1-3 are the three different time experiments that have been measured for every geometrical condition and the mean value represents the average of run 1-3.

No.	W/L	k_{PCA} run 1	k_{PCA} run 2	k_{PCA} run 3	k_{PCA} mean	k_{PIV}	
1	0.35	0.029	0.031	0.030	0.030	0.035	
2	0.40	0.029	0.028	0.022	0.025	0.033	
3	0.48	0.036	0.029	0.034	0.033	0.032	
4	0.59	0.033	0.028	0.028	0.029	0.022	regular cases
5	0.77	0.031	0.032	0.032	0.032	0.023	
6	1.12	0.022	0.026	0.027	0.026	0.022	
7	2.00	0.018	0.019	0.020	0.019	0.019	
8	3.35	0.012	0.013	0.010	0.012	0.015	
9	0.40	0.054	0.053	0.047	0.051		submerged groins
10	0.40	0.034	0.041	0.036	0.035	0.035	$\alpha = 64^\circ$
11	0.40	0.025	0.018	0.023	0.022	0.022	$\alpha = 116^\circ$
12	1.00	0.036	0.030	0.032	0.032	0.021	$\alpha = 64^\circ$
13	1.00	0.015	0.016	0.015	0.015	0.014	$\alpha = 116^\circ$
14	0.17	0.019	0.019	0.016	0.018	0.025	
15	0.25	0.019	0.023	0.025	0.022	0.020	short groins
16	0.25	0.019	0.020	0.022	0.020	0.017	
17	0.40	0.022	0.026	0.022	0.024	0.056	groin field with sloping depth
18	0.40	0.029	0.029	0.030	0.029	0.025	groin field with half depth

In table 5.2 the k_{PCA} values are listed for each series. It should be noted, that in the case of submerged groins it is not possible to start the measurements with a homogeneous concentration distribution. Three-dimensional flow phenomena close to the groins lead to enhanced advective mass transport at the water surface, so that in the vertical direction the mass is not homogeneously distributed. However, the calibration procedure assumes homogeneous mass distribution in the vertical direction, so that inaccuracies in this case are much larger. Another problem is observed in series No. 17 where the bottom in the groin field is inclined towards the main channel. The Multi-Port-Injection-Device described in section 4.3.1 is not able to inject tracer with a certain concentration distribution. Due to the increasing water depth in the groin field in this experiment the concentration decreases linearly from the channel wall towards the main channel. As initial condition we do not have a homogeneous concentration field, which has certain influence on the concentration evolution.

In figure 5.28 the mean exchange values k_{PCA} are plotted against the aspect ratio W/L including an exchange value for the submerged case. The results are very similar to the results obtained with the surface PIV. The exchange rate decreases with increasing aspect ratio W/L . Groins that are inclined against the flow do not strongly influence the mass exchange. Groins that are inclined with the flow lead to a significantly decreasing exchange value. In the case of short groins the k -value is about 50% of the exchange values in the regular cases. The experiments with reduced volume are leading to a slightly reduced mass exchange. An extra data point is plotted for the submerged groins that could not be measured with the PIV system. In that case the mass exchange is much higher than for the other cases. Further discussion of these results and a comparison with the exchange values determined by the surface PIV measurements (figure 5.26) is given in section 5.3.

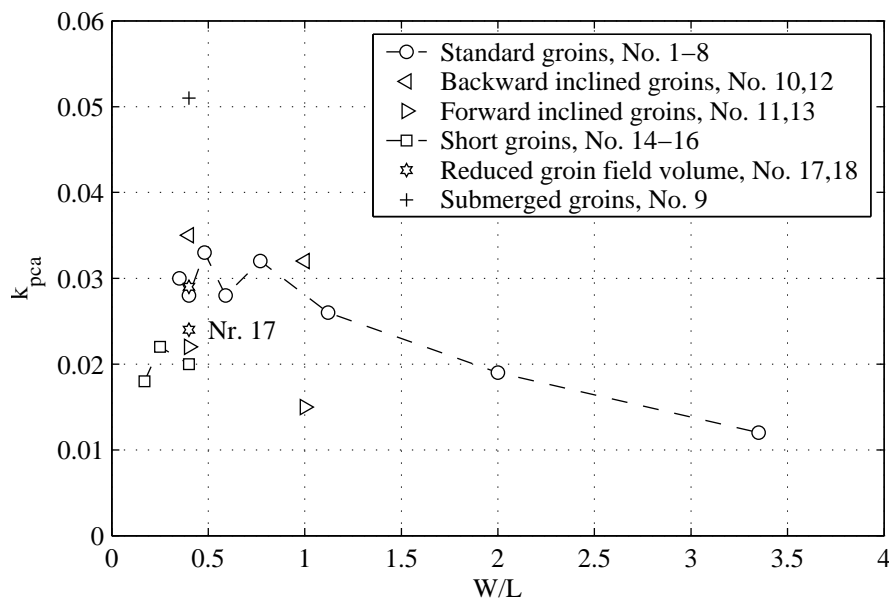


Figure 5.28. Dimensionless exchange coefficient k_{PCA} against the aspect ratio W/L .

5.3 Analysis of exchange coefficients

In this section the determined exchange values are discussed with respect to the different geometrical conditions and regarding the two different measurement techniques, surface PIV and PCA.

5.3.1 Comparison between k_{PIV} and k_{PCA}

In figure 5.29 the k -values determined with the help of two different approaches are compared within the four different groups of experiments. Exchange values can be found in the range of about 0.01 in the case of very narrow or inclined groins to 0.035 in the case of elongated regular groin fields, which is very close to the range already given by Valentine & Wood (1979). It can be seen that in figure 5.29 i-iv) the values obtained with PIV and PCA lie in the same range, except for series No. 17, and the tendency with respect to W/L is always the same.

A difference between the results of the two techniques for the standard groins (figure 5.29, i) can be found for the aspect ratio W/L of 0.59 and 0.77. In these cases problems occurred during the PCA measurements because of too high background concentration, that has led to inaccuracies in the calibration procedure. Therefore, the two calibration parameters d and e from equation 4.4 that have been fixed for every experiment should have been adjusted. However, the number of calibration steps in these two cases does not allow this adjustment.

A large difference between the results from PCA and PIV is also obtained for the groin field with sloping depth (figure 5.29, iv). The resulting exchange coefficient from the PIV measurements is by a factor of two larger than for the comparable PCA result. The

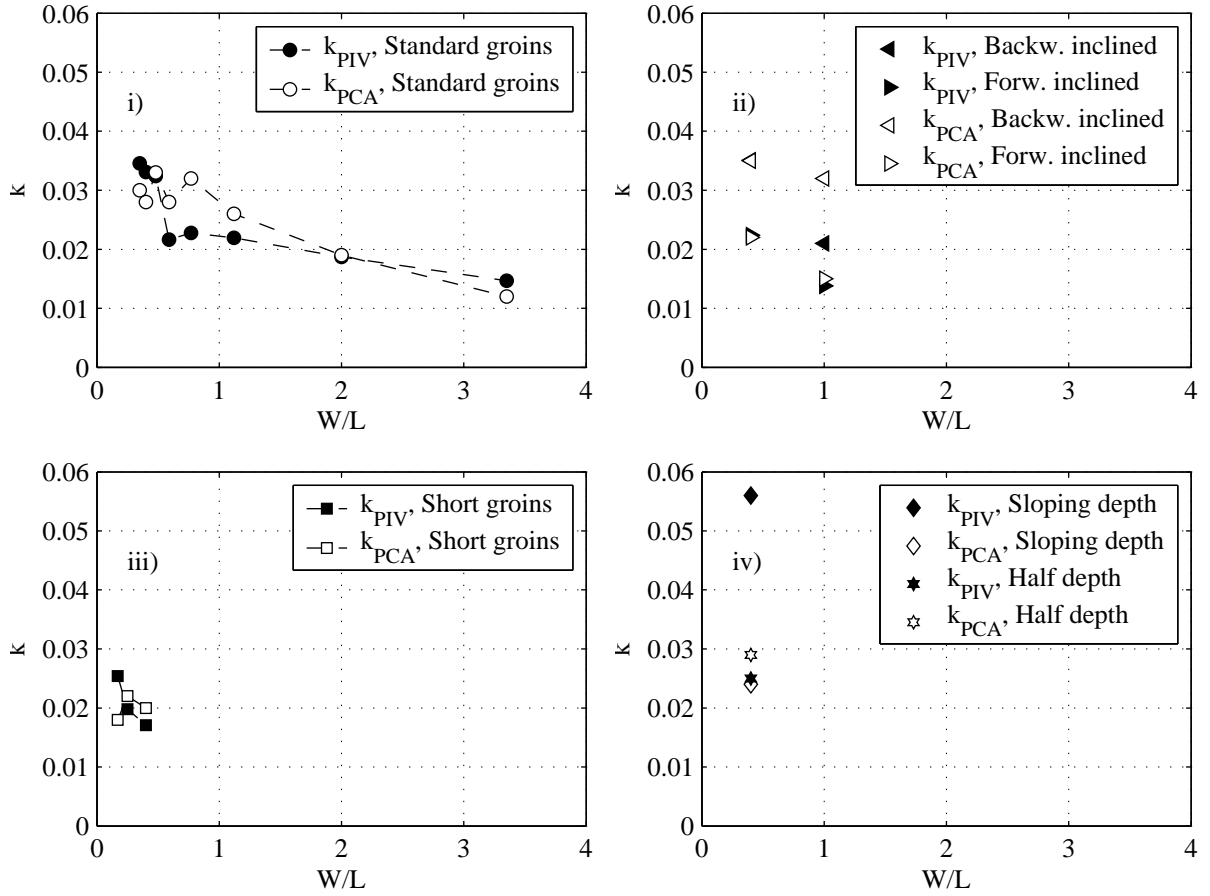


Figure 5.29. Comparison of the k -values determined with surface PIV (filled symbols, \bullet) and the PCA technique (open symbols, \circ); i) Regular cases No. 1-8; ii) Groins that are inclined with and against the flow, No. 10-13; iii) Short groins, No. 14-16; iv) Reduced groove field volume, No. 17,18

k_{PIV} values represent velocity measurements at the groin field boundary. Compared to the standard groin field the velocities do not change strongly at the groin field boundary. The only difference is the water depth that decreases towards the wall, which reduces the groin field volume and leads to a factor of two h_E/h_D for the exchange coefficient. In the case of the PCA measurements the mean residence time T_D is measured directly as an overall measure of the complete groin field, which means that the change of the groin field depth or any other influencing parameter is already included in the result (equation 5.11).

Figure 5.29 shows that both approaches lead to consistent results, which is of major interest for future studies. Experiments with concentration measurements are much more time-consuming than velocity measurements. For experiments with changing water depth in the groin field (series No. 17) the interpretation of the obtained exchange coefficients using PIV is difficult.

5.3.2 Influence of the geometry on the exchange coefficient

Influence of the aspect ratio W/L . Figure 5.29, i shows that the aspect ratio W/L has an influence on the mass exchange coefficient. With increasing length of the groin field

the measured residence time becomes longer, which leads to a smaller exchange coefficient. This statement is also true for the cases of inclined groins (figure 5.29, ii). This behavior leads to increased stretching of a tracer cloud and reduced transport velocity in the case of narrow dead-zone geometries (section 6.4.2). In order to explain this relation between aspect ratio and exchange coefficient it has to be taken into account the process that governs the mass exchange between groin field and main stream. In figure 5.10 it has been shown how the mass transfer is dominated by large coherent eddy structures that emerge at the groin tip, grow during their travel through the mixing layer and finally can travel into the dead-zone or are advected further downstream. In section 5.1.1 it has been shown that the measured rms-velocities represent mainly the fluctuating part of the flow corresponding to the large scale motions, which means that measured rms-velocities are a direct measure of the existence of these motions. The rms-velocities for the series No. 1-8 (figure 5.12) show the same tendency. The turbulence intensity in the mixing layer decreases with decreasing length of the groin field, because in these cases the length of the groin field determines the evolution and growth of the coherent structures.

Influence of the inclination angle. In figure 5.29, ii) it can be observed that an inclination angle of 64° enhances the mass exchange as compared to the reference case, whereas an angle of 116° reduces the mixing. Again, this behavior corresponds to the observed rms-velocities (figure 5.18). Backward inclined groins generate stronger pressure gradients upstream of the groin head that lead to enhanced flow into the groin field and therefore to larger mass exchange. Forward inclined groins lead to much smoother flow conditions and to smaller mass exchange. This behavior corresponds to observations made in nature, where the sedimentation in groin fields with forward inclined groins is much faster, corresponding to lower flow velocities.

Influence of the width of the groin field. The observations made with groins of half the length of the regular groins give a new insight into the complexity of the flow. If the scaling of the exchange parameter with the groin field width W and the main stream velocity U represents the correct physical parameters, we expect that experiments with similar aspect ratio would lead to similar exchange coefficients regardless of the actual size of the groin field. In figure 5.29, iii) it can be seen that in the presented experiments this is not the case. The reference case No. 2 and series No. 16 with short groins have an identical aspect ratio of 0.4. The experiment with short groins, which means that the total volume of the dead-zone is reduced to 25%, leads to an exchange coefficient that is smaller by a factor of 2. The same tendency can be found for the series No. 14 and 15, where the aspect ratio is much smaller. This behavior shows that the intensity of the mixing at the groin field boundary is mainly determined by the length L of the groin field, which is by a factor of 2 smaller in these experiments than in the case of standard groins. In section 5.3.3 a new approach about the scaling of k has been developed in order to take into account these effects.

Influence of reduced volume. In the case of series No. 18, where the water depth in the dead-water zone is half the depth in the main channel, the exchange value is found in the same order (figure 5.33) as for the results from the regular cases. For the series

No. 17 with sloping depth in the groin field, the results obtained with PIV are about a factor of two larger than the other results. The result obtained with PCA for series No. 17 is somewhat smaller than the PCA result for series No. 18, but lies in the same region. As has been mentioned above, in this experiment large areas with very small Reynolds numbers occur in the dead-zone, which can have an influence on the mass exchange. The result from these two experiments tells us that the mass exchange is only slightly influenced by the water depth as long as the flow in the dead-water zone is turbulent.

5.3.3 Normalization of the exchange coefficient k

The dimensional analysis performed in section 4.4 showed that the exchange value should be related to the width W and the length L of the groin field. However, figure 5.26 and 5.28 showed that the normalization with the groin field aspect ratio W/L does not lead to a unique trend of the data, especially for the series with short groins.

Multi-parameter scaling. Another possibility to normalize the resulting exchange coefficients is given by using the combined effects of the three following parameter groups:

- 1) The length of the groin field over the water depth in the main stream L/h_S , which represents the length of the mixing layer and is therefore related to the driving mechanism of the mass exchange. It is expected that the exchange intensity decreases for shorter groin fields.
- 2) The groin field aspect ratio L/W that comprises the effect the groin field width that has a secondary influence on the evolution of the mixing layer width and its penetrating depth into the groin field. It is expected that exchange decreases with increasing width of the groin field.
- 3) The mean water depth in the groin field over the mean water depth in the main stream h_D/h_S to take into account the volume ratio of the groin field. It is expected that the exchange decreases with increasing shallowness.

Assuming a single multiplicative effect of the above mentioned parameter group it can be stated that k should be scaled with the following combination of L, W, h_S, h_D

$$k = f\left(\frac{L}{h_S} \frac{L}{W} \frac{h_D}{h_S}\right) = f\left(\frac{L^2 h_D}{h_S^2 W}\right) \quad (5.12)$$

A further step to take into account the sheltering effect in case of inclined groins can be done by defining an effective length of the mixing layer as follows (figure 5.30)

$$L_{eff} = L - W \sin(\alpha - 90^\circ) \quad (5.13)$$

This definition finally leads to the following relation for a scaling factor of the exchange coefficient

$$k = f\left(\frac{L_{eff}^2 h_D}{h_S^2 W}\right) \quad (5.14)$$

The trend of the exchange coefficient related to the parameter defined in section 5.13 is shown in figure 5.31, where the results from the PCA and the PIV measurements are

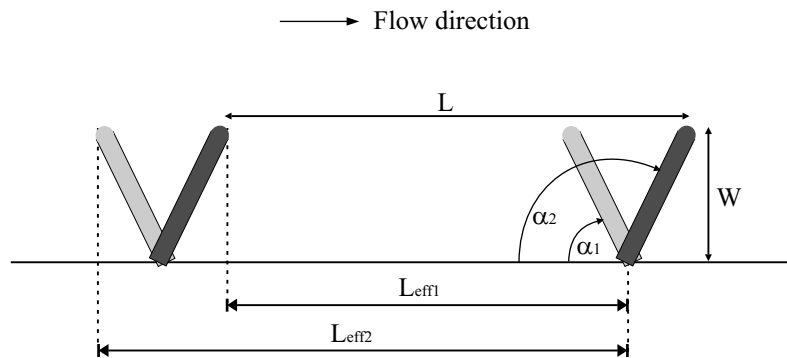


Figure 5.30. Definition of the effective length of the groin field.

averaged. It has to be noted that the data point for the groin field with sloping depth (series No. 17) only represents the PCA result.

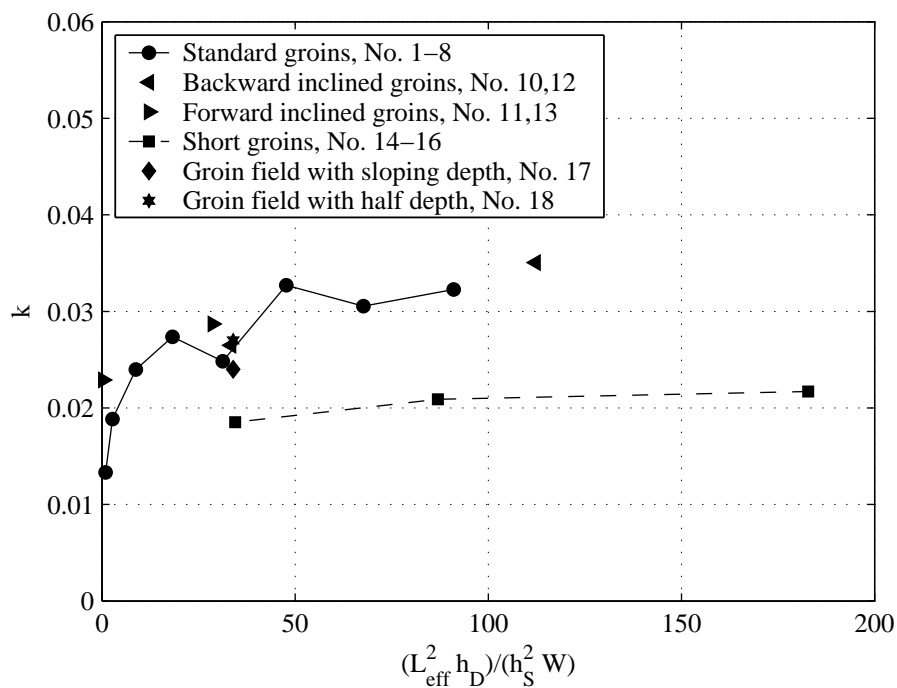


Figure 5.31. Exchange coefficients k averaged from PCA and PIV measurements, in relation to the parameter developed in equation 5.13.

Figure 5.31 shows that the data points for all the experiments performed with regular (50 cm) groins collapse into a narrow region. However, the difference to the results obtained with short groins remains. Also with this multi-parameter scaling the resulting exchange values for short groins lie in a different range below the other results.

Normalizing with the hydraulic radius (shape factor). Another possibility to scale the exchange coefficient is given by means of a shape factor which defined similar to a hydraulic radius R , that can be defined for a groin field as follows

$$R = \frac{W L}{2W + L} \quad (5.15)$$

In open channel hydraulics this parameter expresses the ratio between the cross-sectional area and the wetted perimeter of the flow, which is used to parameterize the influence of the channel shape on the energy losses. In the case of a groin field the hydraulic radius can be interpreted as the ratio between the area of the bottom of the groin field and the perimeter of the contained rotating gyre. The meaning of R becomes obvious if we determine the limit of this value when either W or L go to infinity. If the length L gets very large (figure 5.32, i), which corresponds to small aspect ratios W/L , R from equation 5.15 tends to W . This means, that for very long dead-zones the hydraulic radius R is determined by W only. In figure 5.32, i) such a scenario is visualized. The recirculating flow behind the upstream groin is only determined by the width of the groin field W and is not influenced by the length.

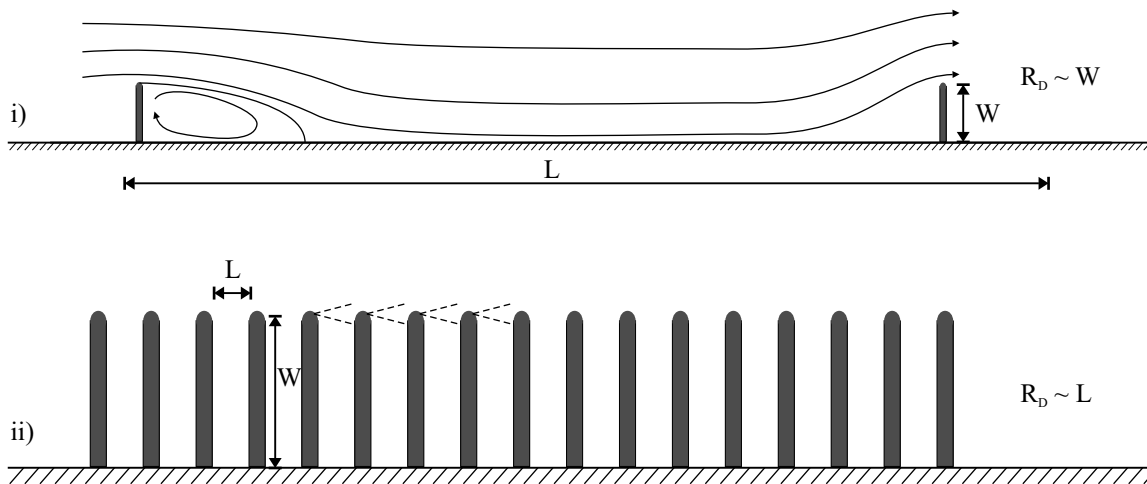


Figure 5.32. Visualization of i) very elongated ($L \gg W$) and ii) very narrow groin fields ($W \gg L$).

A scenario where the width of the groin field is very large compared to the length is visualized in figure 5.32, ii). In this case the development of the mixing layer and, therefore, the mass exchange is only determined by the length of the groin field L . The hydraulic radius as defined in equation 5.15, tends to $L/2$ for very large values of W . Therefore, it seems to be appropriate to omit the factor 2 in equation 5.15 such, that the hydraulic radius of the dead zone R_D finally becomes

$$R_D = \frac{W L}{W + L} \quad (5.16)$$

In figure 5.33 the exchange coefficients k are plotted against the hydraulic radius normalized with the water depth h_S in the main channel. The values of k from the present

study in figure 5.33 are given as averaged from PCA and PIV measurements. In this figure the data point for series No. 17 represents only the result of the PCA measurements.

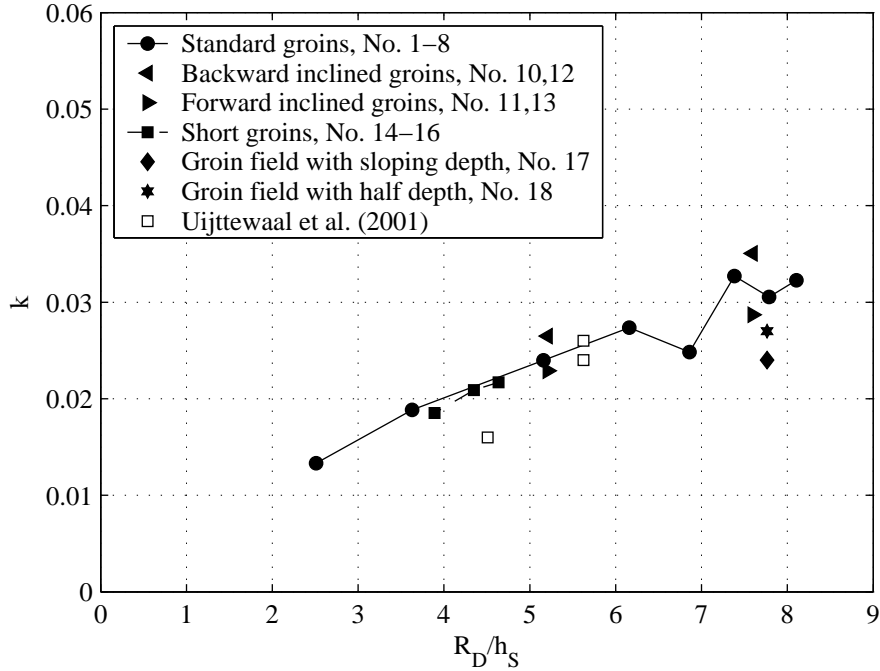


Figure 5.33. Exchange coefficients k averaged from PCA and PIV measurements, in relation to the hydraulic radius R_D/h_S (equation 5.16) of the dead-zone.

Figure 5.33 shows, that the exchange values increase almost linearly with increasing R_D/h_S . The exchange values obtained for short groins (series No. 14-16) do now follow the same trend as the results with the standard groins. The exchange values for inclined groins and for reduced groin field volume do not change their position relative to the standard groins. The concept of an effective length L_{eff} as it has been described in equation 5.13 does not improve the scaling, if it is included into R_D/h_S . A comparison with data from other experiments presented by Uijtewaal et al. (2001) shows that also these data fit very well to the concept of the hydraulic radius.

Compared to the multi-parameter concept (figure 5.31) it seems that the approach using the hydraulic radius R_D (figure 5.33) leads to a more consistent dependance of the exchange value k on the scaling parameter. Therefore, it is proposed to use the concept of the hydraulic radius in order to estimate exchanged values in relation to geometrical condition of the dead-water zones.

6. Lagrangian-Particle-Tracking

6.1 Introduction

In this chapter a transport model is presented, which is used to transfer the local parameters of the laboratory experiments for a single dead-water zone into the global parameters of a 1-dimensional far field model that comprises the action of many dead water zones. As the 1-dimensional transport models described in chapter 3 are not able to take into account explicitly the influence of geometrical changes of the dead-water zone, a 2-dimensional Lagrangian-Particle-Tracking-Method (LPTM) has been developed. The method represents a random walk approach as has been used, for example, by Sullivan (1971) to model turbulent shear flow based on statistical mechanical transport theories presented by Taylor (1921).

As the present transport problem is basically a problem of longitudinal dispersion, we assume that the dominating processes in this case are longitudinal shear and transverse diffusion. Thus, the behavior of discrete particles under the influence of advection in longitudinal direction and of transverse diffusion is determined in a 2-dimensional domain. The idea is to initiate a cloud of particles that is advected within a known mean flow profile. This advective movement is superimposed by a random movement in transverse direction, representing turbulent diffusion.

The characteristic transport parameters, like dispersion coefficient, transport velocity and skewness coefficient, can be determined by analyzing the statistics of such a particle cloud at any position of the simulation. In addition to 1-dimensional information this method yields concentration distributions in transverse direction in order to describe near-field phenomena.

The influences of dead-water zones are included with the help of extra boundary conditions that represent the mean retention time of particles in the area of dead-water zones. Herewith, the influence of different groin field geometries on the mass transport, especially on the mass dispersion, in the far-field of a pollutant spill can be predicted.

In the following section the derivation of the particle model for the present problem is given. Subsequently, the method is verified with the aid of the analytical solution presented for the Advection-Diffusion-Equation for a Couette-Flow problem (Fischer et al. 1979) and turbulent unbounded vertical shear flow given by Elder (1959). Dispersion coefficients obtained from these solutions are compared with the transport characteristics using the LPTM.

In the next step the transport model is used to predict the transport parameters for the flow conditions, taken from the experiments. Mean flow quantities and turbulence

intensities are determined in pure channel flow and are adapted to the LPTM. Finally the influence of dead-zones (groin fields) is implemented. Here the results are compared to a numerical evaluation of Fischer's triple integral originally developed to solve for the longitudinal dispersion coefficient.

6.2 Method

A random walk simulation can be understood as the tracking of discrete particles, under the influence of the governing flow processes. Typically, the particle displacement dX_i is described by a deterministic and a stochastic part, leading to the so called Langevin equation (Gardiner 1985)

$$dX_i = \underbrace{f(X_i, t)dt}_{\text{deterministic}} + \underbrace{Z(t)g(X_i, t)dt}_{\text{stochastic}} \quad (6.1)$$

where X_i is the position x, y and z . $f(X_i, t)$ represents the advective or drift component, which can be interpreted as the mean flow velocity field. The expression $g(x_i, t)$ describes the diffusive or noise component of the particle movement that describes the strength of the turbulent diffusion in space. The stochastic part sits in the Langevin force Z , which is a Gaussian distributed variate with a mean quantity of zero and a variance equal to one.

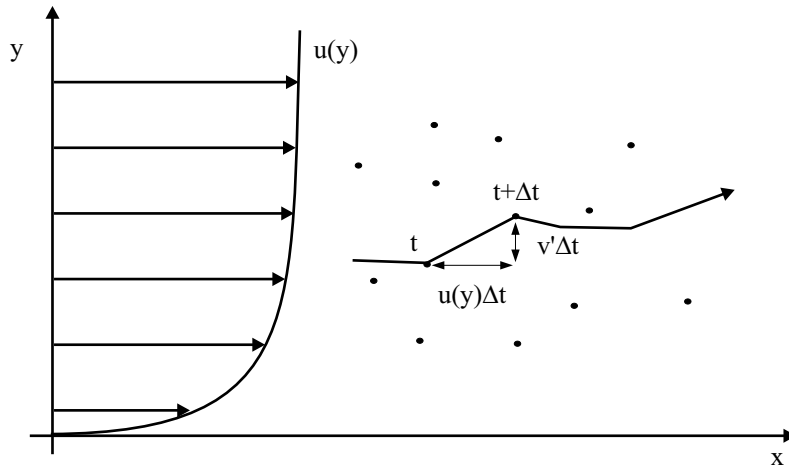


Figure 6.1. Particle velocity in a 2-dimensional flow field with mean velocity in x-direction and turbulent velocities in y-direction

In the present case the governing processes are advection in x-direction and diffusion in transverse direction (figure 6.1), which means that we can neglect the drift component in y-direction and the noise component in x-direction in equation 6.1. An important part of such a model is the link between the diffusive step size and the length of the time step. Here we use the result given by Taylor (1921) who he stated that the spreading of a particle ensemble measured with the standard deviation under the influence of turbulent diffusion can be treated as a Fickian type of diffusion, where $\sigma \sim \sqrt{2Dt}$. The diffusive step size for a single particle at a certain time step in y-direction is therefore given with

$$v' \Delta t = \sqrt{2D_y \Delta t} \quad (6.2)$$

where D_y is the turbulent diffusion coefficient in y-direction. Using these assumptions, the position of the particles in every time step Δt can be described by a simplified 2-dimensional version of equation 6.1.

$$x_{new} = x_{old} + \underbrace{(\Delta t \cdot u(y))}_{deterministic} \quad (6.3)$$

$$y_{new} = y_{old} + \underbrace{Z\sqrt{2D_y \Delta t}}_{stochastic} \quad (6.4)$$

where x_{old} , y_{old} and x_{new}, y_{new} are the spatial locations at times t and $t + \Delta t$ respectively, and D_y is the transverse component of the turbulent diffusion coefficient. The function $u(y)$ denotes the mean flow velocity in relation to the position in transverse direction. Consequently, in every time step, a particle moves *convectively* in x-direction depending on the velocity profile and does a positive or negative *diffusive* step in transverse direction.

The reason why there is no diffusive step in the x-direction needed (equation 6.3) can be explained by the fact that turbulent diffusion in x-direction and longitudinal dispersion are additive processes (Aris 1959), which means that the final dispersion coefficient can be adjusted by adding the turbulent diffusion coefficient. Fischer et al. (1979) showed that in natural rivers the coefficient of longitudinal dispersion D_L lies in the range of $30 < D_L/(u_* h) < 3000$, while the longitudinal turbulent diffusion coefficient D_x is considerably smaller. A typical approximation of the turbulent diffusion coefficient is given by $D_x \approx (0.6u_* h)$, which means that in this approach turbulent diffusion in longitudinal direction can be neglected in compared to longitudinal dispersion. An advantage of this simplification is a shorter computing time.

Flows with inhomogeneous turbulent diffusion coefficients are treated here, which means that D_y is a function of y (section 3.1.1). A problem in performing LPTM-simulations is given by the fact that particles segregate into regions of low diffusivity (Hunter, Craig & Phillips 1993). The reason for that can be seen from the governing equations. In the stochastic model there is no relation between particles moving from regions with high diffusivity into regions with low diffusivity, which should be the case in order to satisfy continuity. That means that the probability of a particle to move from a region of high diffusivity into a region of low diffusivity is higher than vice versa. Thus, an extra advection term in y-direction has to be included to achieve consistency with the governing Advection-Diffusion-Equation. This extra term is called the noise-induced drift component (Dunsbergen 1994), and can be determined as follows. First, it has to be decided if the deterministic step or the stochastic jump is done first during every time step, which is known as the Itô-Stratonovich dilemma van Kampen (1981). In the current work the Itô interpretation has been chosen, which means that the deterministic step is performed before the stochastic jump. Matching the resulting stochastic transport equations with the Advection-Diffusion-Equation Dunsbergen (1994) showed, that in this case, the noise-induced drift component Δy_n can be described as follows

$$\Delta y_n = \frac{\partial D_y}{\partial y} \Delta t \quad (6.5)$$

If equation 6.4 is extended with the given expression for the noise-induced drift component (equation 6.5), the transport problem with varying diffusivity is described consistently with the Advection-Diffusion-Equation.

$$y_{new} = y_{old} + Z\sqrt{2D_y(y)\Delta t} + \frac{\partial D_y}{\partial y} \Delta t \quad (6.6)$$

The influence of the noise-induced drift component is also discussed in section 6.3.2 and visualized in figure 6.8.

Also the boundaries of the calculation domain and how they act on the particles is important. The inflow and outflow boundaries do not affect the particles as in our case the domain has an infinite length. In y -direction there are two possibilities for the boundaries. If we analyze the effect of vertical shear on dispersion, we have the water surface as well as the channel bottom. In case of horizontal shear the boundaries represent the channel banks. For both situations the boundaries act as reflective walls. Particles which would cross the upper or lower boundary at a certain time step are reflected back into the calculation domain (fig. 6.2). That means, a particle with a calculated y -position below the calculation domain $y = 0$ gets a new y -position as follows

$$y_{new} = -y_{calc} \quad (6.7)$$

where y_{calc} is the calculated y -position at a certain time step.

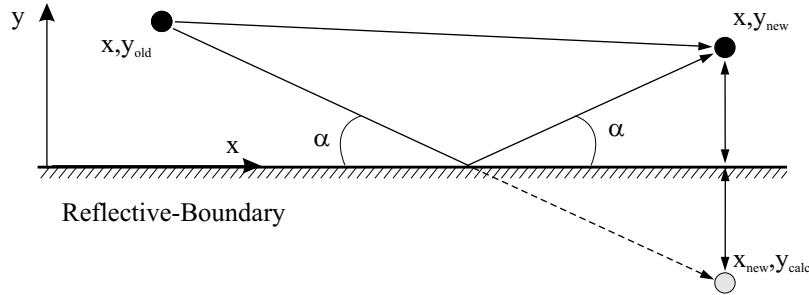


Figure 6.2. Schematic visualization of a particle approach to a reflective boundary within one time step

With the given equations and boundary conditions transport in open channel flow can be simulated with a depth-averaged velocity profile in transverse direction and a certain distribution of the diffusivity. The next step is to include the influence of dead-water zones (figure 6.3) into the LPTM.

As has been shown in section 5.3, the mean residence time of tracer material in the dead-water zone is the most important parameter to describe the behavior of a dead-water zone. Therefore, it should be possible to model the influence of the mass transport by including this parameter into the LPTM. A simple approach to parameterize the trapping of tracer mass in the dead-water zone is to include the residence time into the boundary condition, such that this boundary simulates the behavior of mass trapping and

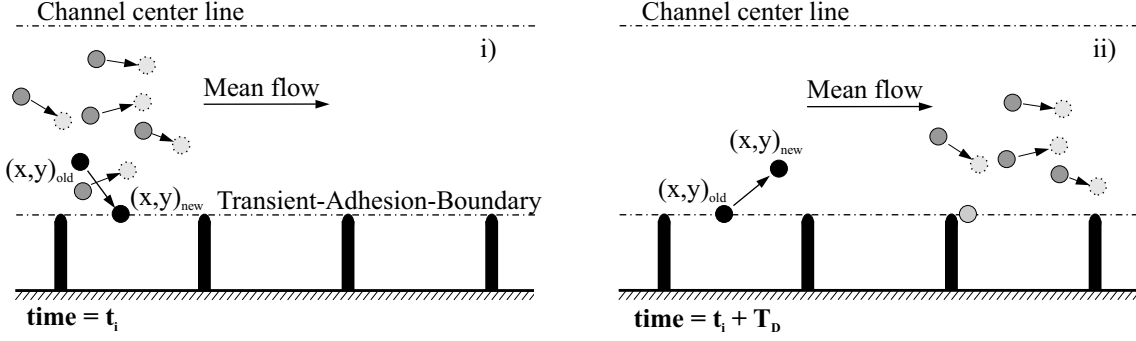


Figure 6.3. Schematic visualization of a particle approach to a transient adhesion boundary at: i) time $= t_i$ and ii) time $= t_i + T_D$, where T_D is the mean residence time.

mass release. Thus, the interface between main channel and dead-water zone has to act as a transient-adhesion boundary, which means that particles that reach such a boundary are fixed to that position until T_D has passed. This is similar to the real dead-zone behavior. A particle that enters a dead-water zone because of turbulent motion in the mixing layer, does not move on average in x-direction, assuming that the longitudinal extension of the dead-water zone is small compared to the length of the modeled river section. On average the particle remains in the dead-water zone for a time period given by the mean residence time T_D , and after that period it gets back into the main stream.

The outcome of a LPTM simulation are x and y -positions of every single particle at every time steps. By analyzing the statistics of the particle positions, information about the transport characteristics can be determined. The 1-dimensional longitudinal dispersion coefficient D_L , as a measure of the spatially averaged spreading rate of a tracer cloud, can be determined by calculating the time change of the longitudinal variance of the particle distribution (Rutherford 1994) as follows

$$D_L = \frac{1}{2} \frac{\sigma_x^2(t_2) - \sigma_x^2(t_1)}{t_2 - t_1} \quad (6.8)$$

A second result will be the skewness G_t of the particle cloud. The skewness is defined as the relation between the quotient of the third moment about and the third power of the standard deviation

$$G_t = \frac{\sum_{i=1}^n (x_i - \bar{x})^3}{(n-1)\sigma_x^3} \quad (6.9)$$

where n is the number of particles at the positions x_i with mean position \bar{x} . The skewness of a certain distribution describes the degree of asymmetry of a distribution. If the distribution has a longer tail less than the maximum, the function has negative skewness. Otherwise, it has positive skewness. The skewness can be used as an indicator for the length of the advective zone, in order to define when it is acceptable to apply the Taylor solution to a pollutant transport problem.

A third parameter that is of interest is the transport velocity c of the tracer cloud, defined as the velocity of the center of mass of a particle ensemble. In the case of regular channel flow with ordinary reflective boundary conditions c is equal to the mean velocity if

the particles are homogeneously distributed over the river cross section. In case of point sources this can be reached after the tracer has passed the advective zone. The transport velocity can be determined as follows

$$c = \frac{\bar{x}(t_2) - \bar{x}(t_1)}{t_2 - t_1} \quad (6.10)$$

where \bar{x} represents the center of mass of a particle cloud.

6.3 Verification of the model formulation

The presented transport model is first compared qualitatively with the behavior of transport problems described in the literature. A quantitative verification of the presented LPTM is given by comparing the results with analytical solutions of the Advection-Diffusion-Equation. The obtained dispersion coefficients from particle simulations are compared to the analytical solutions given by Fischer et al. (1979) for the Couette problem, and by Elder (1959) for unbounded shear flow.

6.3.1 Qualitative comparison of the particle behavior

In this section the overall behavior of a particle cloud in a Lagrangian particle simulation is compared to known results of longitudinal dispersion. An important result of prior analytical and experimental studies (Taylor 1954, Fischer et al. 1979), is an equilibrium between longitudinal stretching and transverse diffusion at a certain distance downstream of the mass release (section 3.2). Downstream of that point the longitudinal variance of the spatial averaged concentration increases linearly with time ($\Delta\sigma \sim \sqrt{\Delta t}$), which means that D_L reaches a certain limit. The skewness which was induced by velocity shear in the advective zone or by the initial distribution, vanishes (Rutherford 1994). If there is no additional disturbance like a change in geometry or discharge, which causes a change in the dispersive character of the flow, the skewness eventually becomes zero, so that the distribution in longitudinal direction becomes Gaussian.

In figure 6.4 a simple case of an advection diffusion system is visualized. A cloud of 8000 particles has been released where initially the particles are distributed homogeneously over the channel width. The velocity distribution is parabolic over the channel width and diffusion coefficient D_y is constant.

Figure 6.4, i) shows a top view of a virtual channel with the particle cloud at three different time steps. In all three positions the effect of the velocity profile is still visible. The relatively sharp front at the first two time steps is a result of the omitted turbulent diffusion in x-direction. Figure 6.4, ii) shows an evaluation of the cross-sectionally averaged particle distribution in longitudinal direction. In the initial stage of the calculation the particle distribution is strongly skewed which is also shown by the evolution of the determined skewness in figure 6.4, iii). When the initial time, known as the advective stage, has passed, the skewness slowly decays, so that finally the distribution tends to be Gaussian. The final value of the longitudinal dispersion coefficient is already obtained

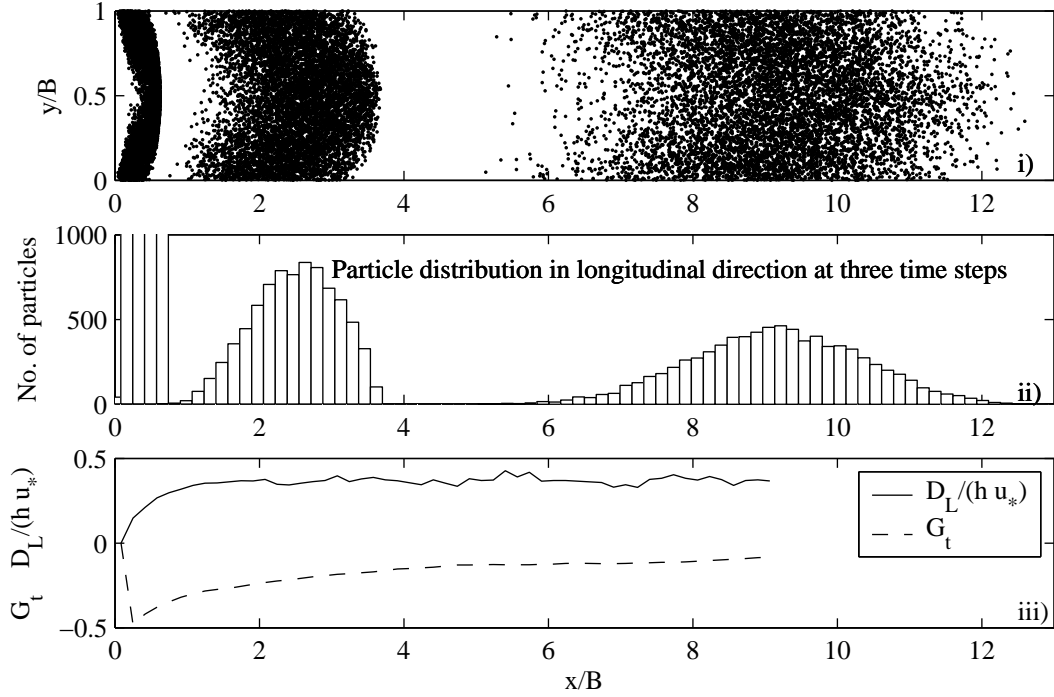


Figure 6.4. LPTM simulation for parabolic velocity profile with constant transverse diffusivity; i) 8000 particles after 5, 40 and 100 time steps, under the influence of a parabolic velocity distribution and constant diffusion in transverse direction. Initially the particles are distributed homogeneously over the channel width; ii) Distribution of the particles in longitudinal direction; iii) Time series of the longitudinal dispersion coefficient and skewness evaluated at each time step.

after the first quarter of the whole simulation where the distribution is still considerably skewed. This tendency is analogous to the behavior of turbulent transport processes as described by Taylor (1954).

6.3.2 Quantitative verification

Fischer et al. (1979) derived an analytical solution for dispersion laminar shear flow between two parallel plates of infinite extent where the top plate moves with velocity U compared to the bottom plate, so that the velocity distribution will be

$$u(y) = U \frac{y}{h} \quad (6.11)$$

where U is the mean flow velocity and h the flow depth. A visualization of the flow conditions is given in figure 3.6. The diffusion coefficient D_y in transverse direction is constant over the whole width of the flow. The derivation of the dispersion coefficient D_L corresponding to these conditions is described in section 3.2.2 and leads to

$$D_L = \frac{U^2 h^2}{120 D_y} \quad (6.12)$$

The analytical solution has been compared with the LPTM computation for three different cases described in table 6.1. The difference in the first two cases is a diffusion

coefficient ten times smaller than in the second case that has a ten times larger Peclet number $Pe = \frac{hU}{D}$. h is the depth of the flow that is the characteristic length of the transport phenomena depth of the flow, U the mean velocity, and D the diffusion coefficient (Kinzelbach, Zimmermann & Koumoutsakos 2001). In Case 2 the number of time steps has been increased by a factor of 10 to compensate for the smaller diffusive step size. In Case 3 the number of particles is increased by a factor of 20.

Table 6.1. Parameter values of a sensitivity study for a LPTM simulation for laminar Couette shear flow

	Case 1	Case 2	Case 3
h [m]	1.0	1.0	1.0
U [m/s]	1.0	1.0	1.0
n particles []	5000	5000	100,000
i time steps []	40,000	400,000	40,000
dt [s]	0.1	0.1	0.1
$D_y/(hU)$	0.001	0.0001	0.001
Pe []	100	1000	100
Analytical solution			
$(h^2U^2)/D_L D_y$ (Eq. 3.49 and 6.12)	120	120	120
LPTM			
$(h^2U^2)/D_L D_y$ (Eq. 6.8)	115.7980	115.9445	119.7636
Averaged over second half of simulation			

The analytical solution is only valid for the far-field where the standard deviation of the tracer cloud is linearly growing with respect to time $\Delta\sigma \sim \sqrt{\Delta t}$. Therefore, only the dispersion coefficient from the final stage of mixing can be compared. In this case the values of the second half of the simulation are averaged, which corresponds to a length of 1000 times the channel width. The results from Case 1 and 2 table 6.1 show that the method leads to results that are close to the analytical solution and are not very sensitive to the Peclet number. The error of the LPTM in the predicted dispersion coefficient compared with the analytical solution is of the order of 5% for the first two cases. These errors can be explained by the limited number of particles and numerical errors that occur in the calculation of the particle position. These errors lead to increased fluctuations of the resulting dispersion coefficients during the simulation (figure 6.6), which can be explained by the increasing standard deviation of the tracer cloud, such that the rounding errors in equation 6.8 become more pronounced. By increasing the number of particles to 100.000 in Case 3 the error in the resulting dispersion coefficient can be reduced to 0.2%. For the purpose of predicting longitudinal dispersion coefficients in rivers it can be stated that this accuracy is sufficient. This is in line with Fischer et al. (1979) who stated that for the prediction of longitudinal dispersion in rivers a variability within a factor of four for the dispersion coefficient appears acceptable.

In figure 6.5 the simulation of a particle cloud under the influence of linear shear and constant transverse diffusion is visualized for certain time steps analogous to figure 6.4. In figure 6.5, a the linear velocity distribution visualized by the particle distribution

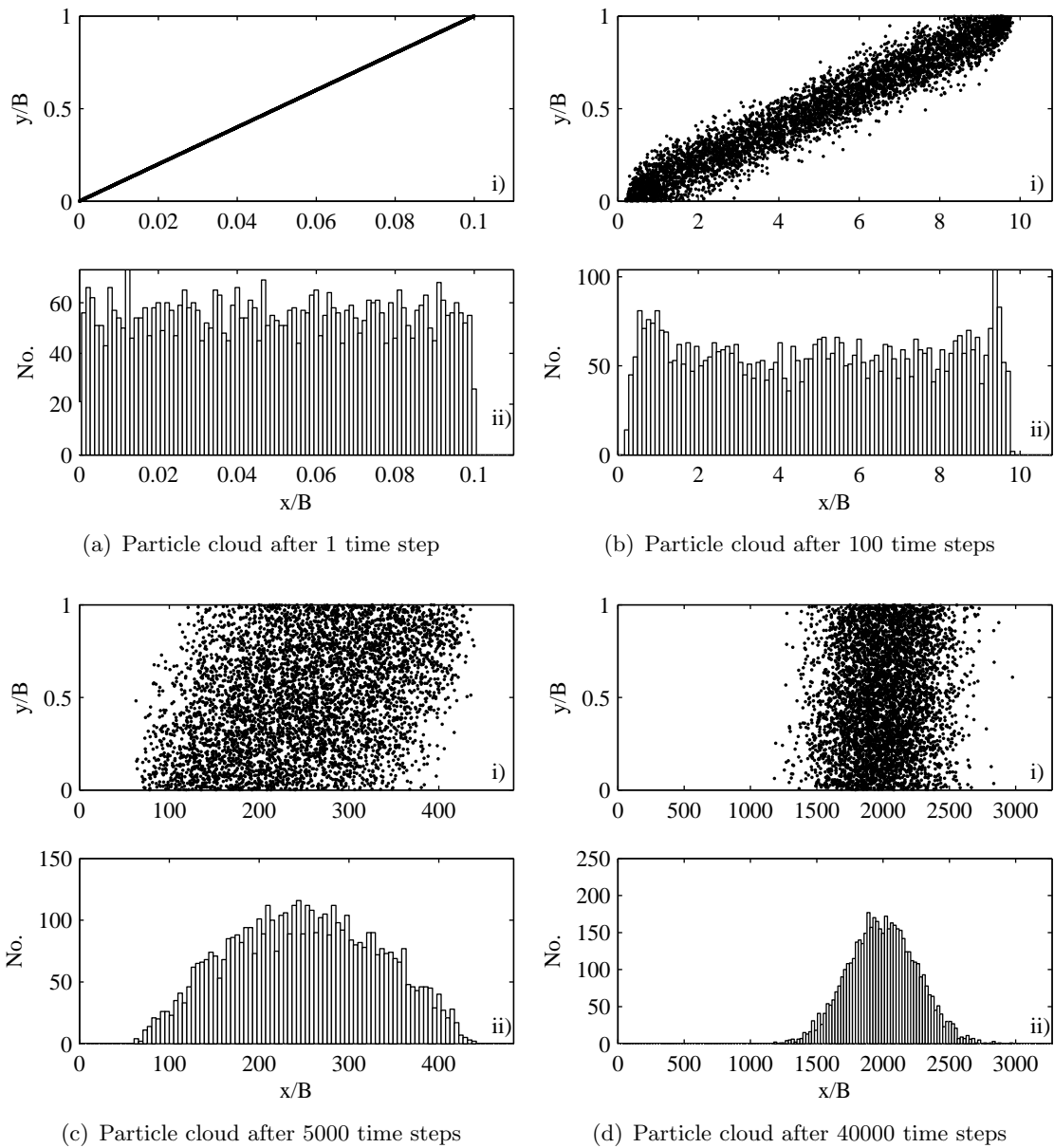


Figure 6.5. LPTM simulation for Case 1 with linear velocity shear and constant transverse diffusion coefficient, showing the particle position and the particle distribution in longitudinal direction.

after one time step is clearly visible. The diffusion in transverse direction is too small to be seen at that stage. The particle distribution at the first time step is close to a homogeneous distribution. The small scatter is the result of the chosen number of bins in the histogram. After 100 time steps (figure 6.5, b) the linear velocity distribution is still visible but also the scatter due to transverse diffusion starts to play a role in the transport process. The distribution of particles in longitudinal direction is still homogeneous with slight deviations at the front and at the end. After 5000 time steps (figure 6.5, c) the simulation is approaching an equilibrium state where the particles are well mixed in

transverse direction. In the longitudinal direction the particles are getting closer to a Gaussian distribution, which can finally be seen in figure 6.5, d.

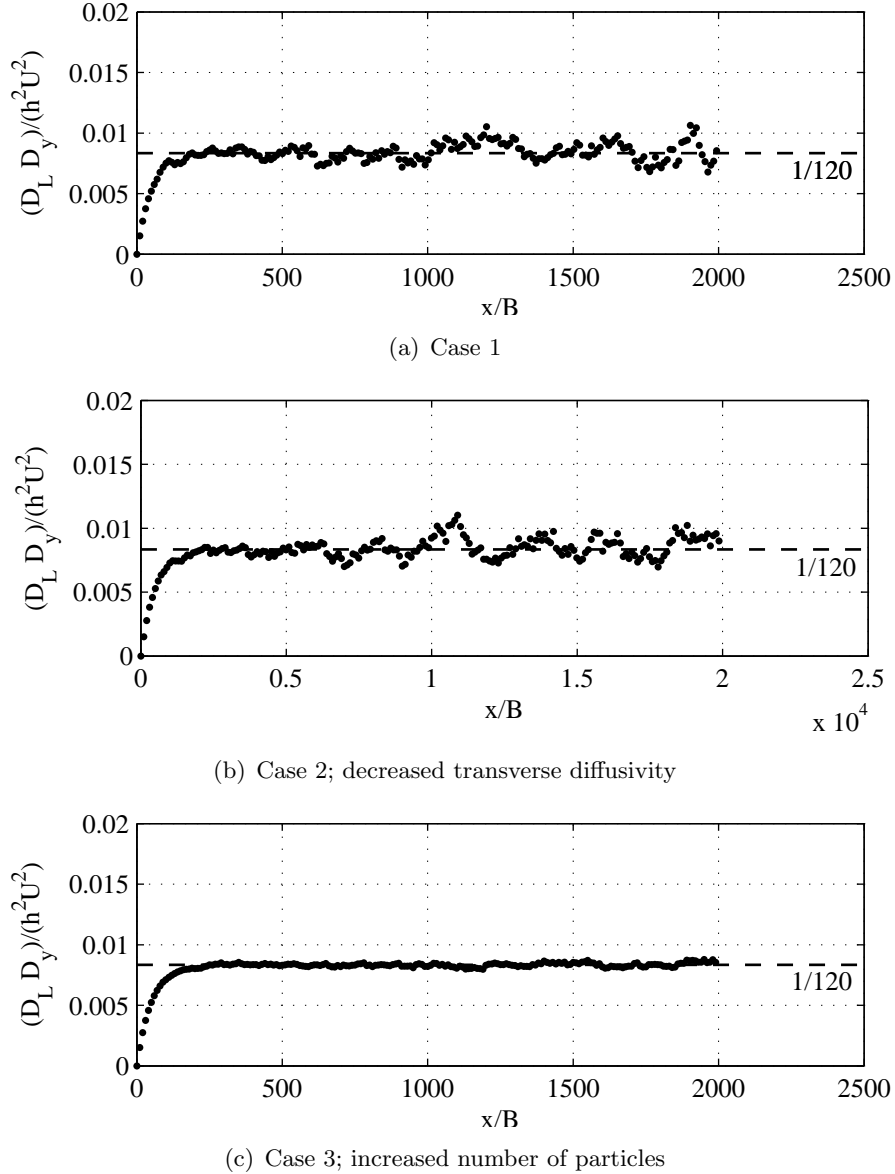


Figure 6.6. Evolution of the dispersion coefficient in the case of laminar flow between plates (Couette problem) for the Cases 1-3 from table 6.1.

In Case 1, the longitudinal dispersion coefficient D_L has reached a certain limit after the tracer cloud has passed 250 times the flow width (figure 6.6, a), which corresponds to length of the advective zone $L_x = \alpha B^2 U / (D_y)$ (equation 3.55) with $\alpha = 0.25$. In order to evaluate E_L for the equilibrium state the calculation could be stopped at this position. The only change of the behavior between time step 5000 and 40000 (figure 6.5, c) is that the scatter of the longitudinal dispersion coefficient starts to increase. This is due to the fact that the rate of change of the variance becomes smaller. In Case 2, where the diffusion

coefficient is decreased by a factor of ten, the equilibrium between longitudinal stretching and transverse diffusion is reached ten times later after 2500 channel widths (figure 6.6, b). A smooth behavior in that part of the simulation is reached in Case 3 where the number of particles has been increased by factor of 20 up to 100,000. In figure 6.6 c the evolution of the dispersion coefficient is plotted for the case of an increased number of particles, which is much smoother in that case. The standard deviation in the second half of the simulation is reduced by one order of magnitude. However, the mean value is not affected by the number of particles.

In case of the Couette problem with linear shear the skewness of the particle distribution does not vary during the simulation. The reason for this behavior is the fact that linear shear does not cause any fronts or a tailing of the particle cloud. Hence, initially symmetric distribution in longitudinal direction remains symmetric during the whole simulation.

Another, more complex situation has been chosen to test the model under the influence of varying diffusion in transverse direction. In the case that has been described by Elder (1959), a homogeneous flow is assumed in an infinitely wide channel. The velocity profile over the vertical is determined by the logarithmic law

$$u(y) = -\frac{u_*}{\kappa} \log(1 - y/h) \quad (6.13)$$

where u_* is the shear velocity, given by $\sqrt{\tau_o/\rho}$, h is the water depth and κ is the von Karman constant 0.41. The distribution of the diffusivity is determined by the velocity gradient leading to

$$D_y(y) = \kappa u_* y(1 - y/h) \quad (6.14)$$

By inserting equations 6.13 and 6.14 into the analytical expression found by Taylor(1954) for the determination of D_L given in equation 3.42 the following expression for D_L can be found by evaluating the triple integral

$$D_L = 5.86 u_* h \quad (6.15)$$

To adjust diffusive-noise drift component from equation 6.5, for the varying diffusivity in space, it has to be derived by the differentiation of equation 6.14, leading to

$$\frac{\partial D_y}{\partial y} = \kappa u_* (1 - 2y/h) \quad (6.16)$$

In order to compare the results of the analytical solution with the output of the LPTM a simulation has been performed, where 10,000 particles were released homogeneously distributed over the river cross-section at $x = 0$. The boundary conditions for this simulation are summarized in table 6.2.

In figure 6.7 the particle cloud and the distribution of the particles in longitudinal direction are visualized after the first and the last time step of the simulation. In figure 6.7a, i) the velocity profile is clearly visible after the first time step because the diffusive step in transverse direction is small compared to the advective step in x-direction. It can be seen that the initial distribution of the particles in longitudinal direction is strongly negatively

Table 6.2. Parameter values for the Elder simulation

Property	Value
water depth h [m]	1.0
$u(y)$ velocity profile	Eq. 6.13
No. of particles	10,000
No. of time steps	100,000
Δt length of time step [s]	0.0005
D_y diffusivity [m^2/s]	Eq. 6.14

skewed, with a strong rising limb and the typical tailing. In figure 6.7b, i) the particles are homogeneously distributed over the water depth. The velocity distribution has been smeared out. The particle distribution in longitudinal direction is close to a Gaussian distribution (figure 6.7b, ii).

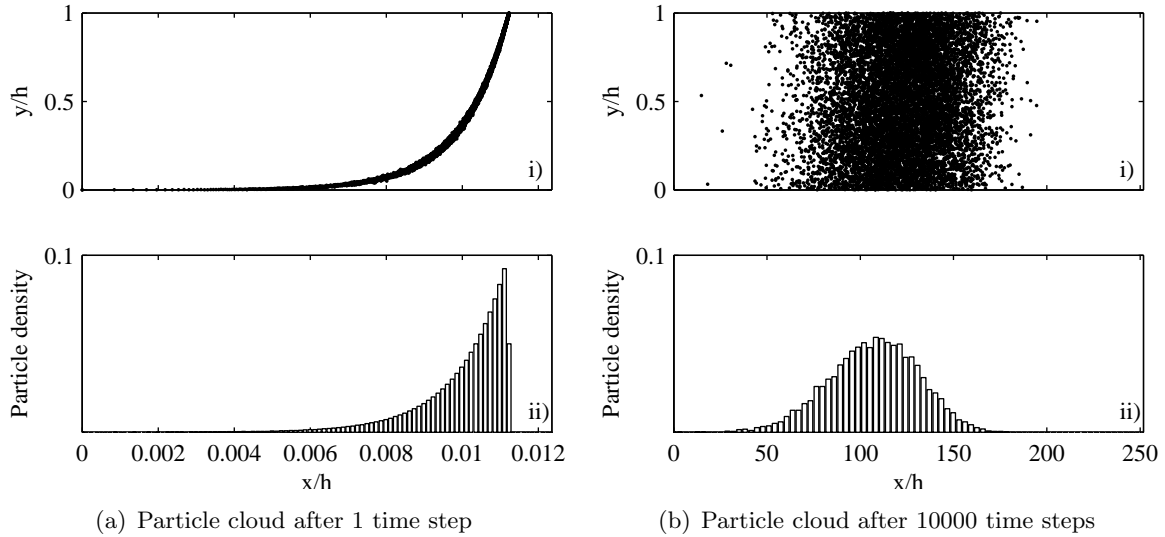


Figure 6.7. Lagrangian particle tracking simulation of the Elder's case with unbounded shear flow and a parabolic distribution of the diffusivity over the water depth; i) showing the particle positions at a certain time step; ii) showing the particle density cross-sectionally averaged in longitudinal direction.

An important result of this simulation is the distribution of the particles in transverse direction. Simulations with neglected adjustment for the varying diffusivity showed a clear tendency of the particles to segregate at the water surface or at the channel bottom, respectively (figure 6.8, i). Due to the parabolic distribution of the diffusivity in these regions the diffusivity is much lower than in the center of the water depth. Figure 6.8, i) shows the results of a LPTM simulation with the Elder conditions, where the noise drift correction has been neglected. The particles accumulate at the water surface and at the channel bottom, hence, in regions with low diffusivity. This inhomogeneous particle distribution, due to changing diffusivity, leads to additional stretching and therefore to increased longitudinal dispersion. After the implementation of the term 6.16 derived from equation 6.5

the simulation leads to homogeneous particle distribution in transverse direction during the simulation (figure 6.8, ii).

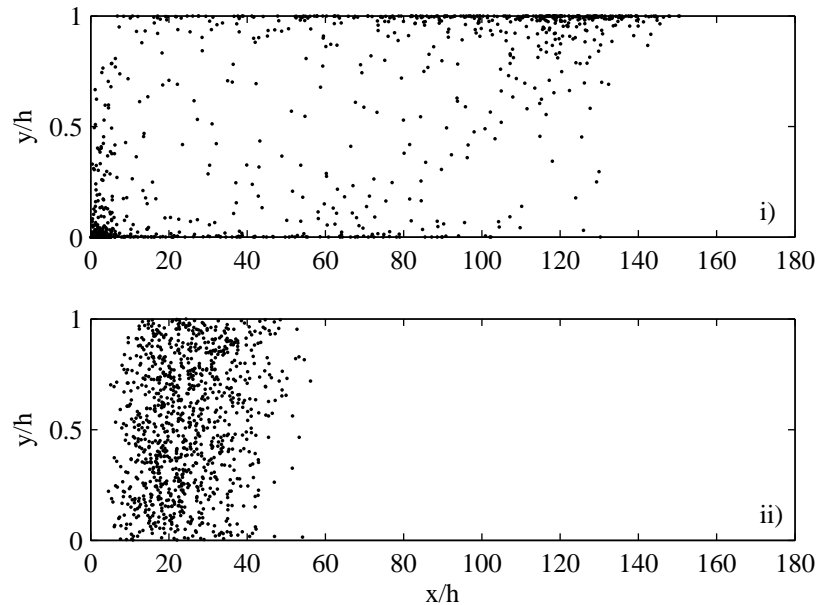


Figure 6.8. Visualization of the influence of the noise drift component in the Elder's case; i) LPTM simulation where the noise drift correction is neglected, leading to high particle concentrations close the water surface and the channel bottom; ii) LPTM simulation including the noise drift correction, leading to a homogeneous particle distribution.

In figure 6.9 the evolution of the longitudinal dispersion coefficient and of the skewness G_t is plotted. The value for D_L shows that the equilibrium between longitudinal stretching and transverse diffusion, which corresponds to a linear growth of the tracer cloud, is reached after approximately 12 water depths. At this distance, D_L has attained its final value of $5.86u_*h$ in agreement with the analytical prediction by Elder (equation 6.15). The D_L curve has been smoothed, in order to show the mean behavior of the tracer cloud. Without filtering an increased scatter could be observed, due to the increasing error that is produced by determining the standard deviation σ_x (equation 6.8) that gets larger with increasing width of the tracer cloud.

6.4 Application

In this section the LPTM is applied to different flow fields, that have been investigated in the laboratory in order to determine the influence of river heterogeneities on the mass transport properties of a river. Three, different cases will be analyzed in detail. First, the behavior of the dispersive character of pure channel flow without the influence of groin fields is investigated. In a second step groin fields are implemented, and the influence of different residence times, due to changes in the geometry of the groin field, on the transport

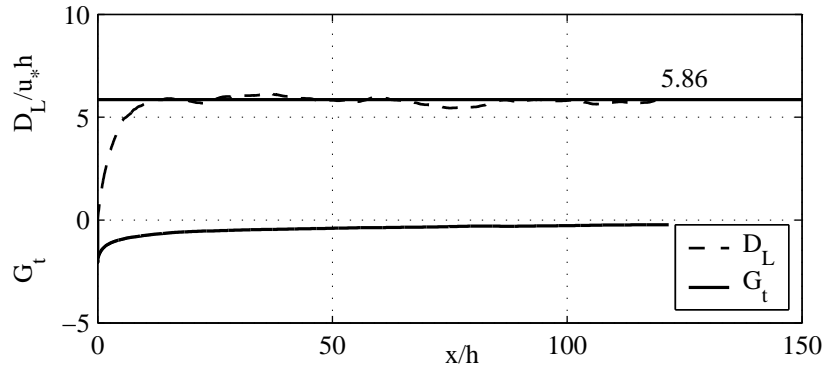


Figure 6.9. Evolution of the longitudinal dispersion coefficient D_L and the skewness G_t during the LPTM simulation. D_L is smoothed with a sliding average filter of increasing window size.

characteristics is determined. Finally, longitudinal dispersion under the influence of groin fields and changing width of the river is analyzed.

6.4.1 Open channel flow without groin fields

A LPTM simulation has been performed, in order to analyze transport phenomena in regular channel flow with smooth vertical boundaries and without the influence of groin fields. The measured velocity field (section 5.1.1) is determined hereby with the approximation given in equation 5.2, which is visible after the first time step in figure 6.10, a). The transverse diffusion coefficient in this case has been chosen to be constant over the whole river cross-section, with a value according to Fischer et al. (1979) for straight rectangular channels in laboratory flumes

$$D_y = 0.15u_*h \quad (6.17)$$

In table 6.3 the properties of the flow and the settings of the LPTM simulation for the case of pure channel flow are listed.

Table 6.3. Parameter values for the pure channel flow simulation, taken from the measurements

Property	Value
Channel half width $B/2$ [m]	1
Mean velocity [m/s]	0.19
Velocity distribution	Eq. 5.2, figure 6.10, a)
No. of particles	5000
No. of time steps	40,000
Length of time step Δt [s]	1
Diffusivity D_y [m^2/s]	Eq. 6.17

In figure 6.10, a) the results of the LPTM simulation for undisturbed channel flow is visualized after the first time step and after the last time step when the particle cloud has passed 3700 times the channel width. The same behavior as in the verification tests can be seen. The initially strong skewed particle distribution tends towards a Gaussian

distribution. At this stage the particle cloud has reached a length of about 200 times the channel width.

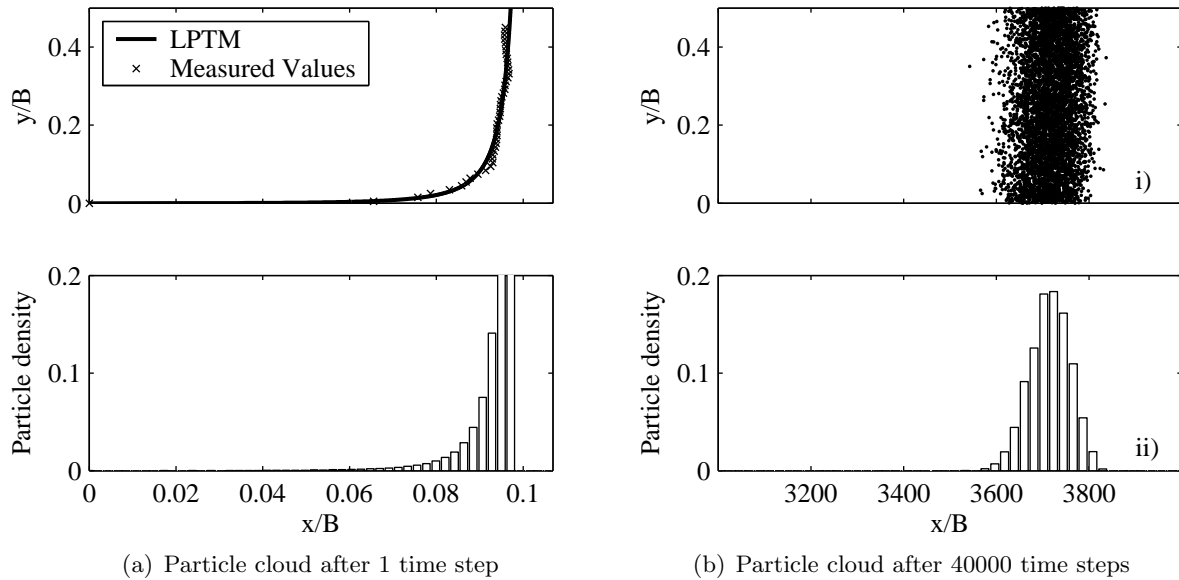


Figure 6.10. Lagrangian particle tracking simulation of pure open channel flow with constant diffusivity over the channel width; i) showing the particle positions at a certain time step; ii) showing the particle density cross-sectionally averaged in longitudinal direction.

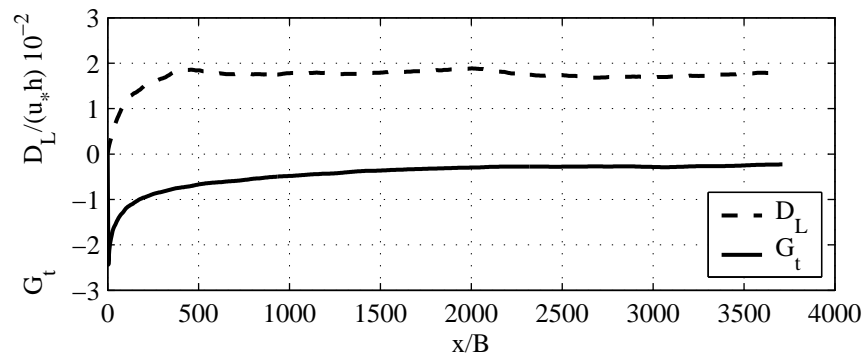


Figure 6.11. Evolution of the longitudinal dispersion coefficient $D_L/(u_*h)10^{-2}$ and the skewness G_t during the LPTM simulation.

The evolution of skewness and dispersion coefficient is in principle very similar to Elder's case (figure 6.9). The equilibrium between longitudinal stretching and transverse diffusion, where the dispersion coefficient does not change any more, is reached after 400 times the channel width. The final value of $D_L/(u_*h)$ is 175, and is therefore 30 times larger than in Elder's case. The skewness coefficient G_t decreases from -2 to a final value of -0.1. This final value is approximately reached after the particle cloud has travelled 1500 times the channel width.

6.4.2 Channel flow with groin fields

The influence of groin fields is parameterized with the transient-adhesion boundary condition that has been described in section 6.2. This boundary condition simulates the affect of the mean residence time of a particle in the groin field. These mean residence times have been measured in this study using PCA and surface PIV (section 5.1.7).

An LPTM simulation has been performed with the same flow conditions as in the described case above (table 6.3). The difference is the transient-adhesion-boundary condition at the channel wall. This simulation represents the groin fields in the reference experiment No. 2 (table 4.2), where the ratio between the width W of a groin field divided by the length L is 0.4. These conditions correspond to laboratory measurements with a groin field length 1.25 m and a width of 0.5 m. As the water depth in the groin field and the main stream is the same, the ratio between the cross-sectional area of the dead-water zone and the main stream is 0.5. The mean residence time T_D of a tracer particle has been set to 90 s, which corresponds to the measured dimensionless exchange coefficient

$$k = \frac{W}{T_D U} = 0.030 \quad (6.18)$$

where W is the width of the groin field and U represents the mean flow velocity in the main channel.

In the case of channel flow with groin fields, the velocity profile is slightly changed compared to the pure channel flow because in the presence of groin fields the velocity profile has to represent the mixing layer between groin field and main stream and can be approximated with equation 5.1, where the velocity is greater than 0 at $y = 0$ (figure 5.3). The distribution of the diffusivity in that case is not constant over the channel cross-section. In the present case the transverse distribution of D_y has been approximated with (equation 5.4), such, that the diffusivity in the mixing layer is about two times larger than in the main channel.

In figure 6.12, a) the LPTM simulation with groin fields is visualized after 200 time steps. The main difference with respect to pure channel flow are secondary particle clouds that travel far behind the main tracer cloud, which is an phenomenon that can also be observed in the laboratory flume. These small particle clouds arise by the effect of the dead-water zones. Particles that have crossed the lower boundary layer during the simulation, remain at the same x-position for the mean residence time T_D . After T_D has elapsed the particles get back to the flow. The mean distance between the secondary clouds corresponds to the mean residence time.

The final stage of mixing in the case with groins shows again that after a long period the tracer cloud gets close to Gaussian distribution in longitudinal direction, which can be seen in figure 6.12, b).

Interesting properties of this simulation are also the evolution of the dispersion coefficient and of the skewness that are visualized in figure 6.13. The final value of $D_L/(u_* h)$ is approximately 24,800 which is of a factor 140 higher than the prior case of pure channel flow, and about four times higher than the expected values for natural rivers without groin fields. This can be explained by the ratio between the cross-sectional area of the

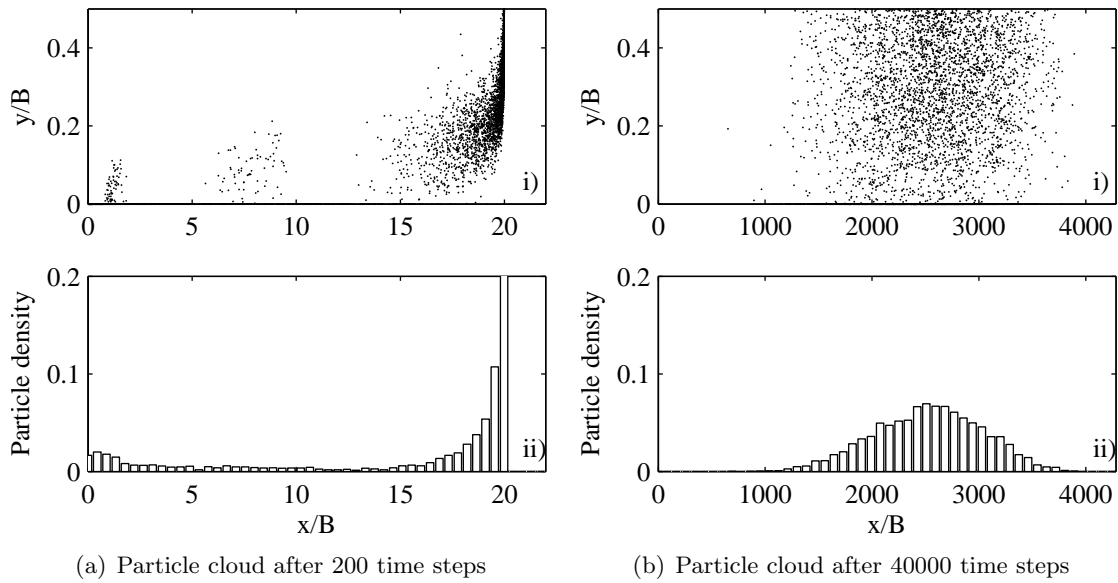


Figure 6.12. Lagrangian particle tracking simulation of the channel flow under the influence of groin fields; i) showing the particle positions at a certain time step; ii) showing the particle density cross-sectionally averaged in longitudinal direction.

dead-water zone and the cross-sectional area of the main channel, which is 0.5 for the experiment and rather high compared to natural rivers. This strong increase of the stretching rate compared to pure channel flow, which is caused by the mass exchange, shows that diffusion in longitudinal direction does not play an important role. An additional simulation has been performed, where the diffusivity has been set as a constant, determined by equation 6.17. The resulting value of $D_L/(u_*h)$ noticeably increases to 31,400, which can be explained by the reduced homogenization in the region of the mixing layer. However, the influence of varying diffusivity would be less important with increasing channel width because the width of the mixing layer between dead-water zone and main channel usually is not determined by the channel width. However, the region of the mixing layer is the region where the diffusivity is strongly increased.

A possibility to prove these results is given by the analytical solution given by Fischer et al. (1979), which is discussed in section 3.3.2. In the present case the resulting triple integral (equation 3.57) has been evaluated numerically, directly using the measured flow velocities. In table 6.4 the results obtained with the LPTM and the evaluation of Fischer's triple integral are compared.

Table 6.4. Results of LPTM simulations compared with the evaluation of Fischer's triple integral given in equation 3.57.

	$D_L/(u_*h)$		$D_L/(u_*h)$
	LPTM	triple Int., equation 3.57	1-D approx., equation 3.58
Pure channel flow	177	166	6860
Flow with groins	24370	35900	6860

For pure channel flow the values given in table 6.4 show a good agreement between the two approaches, where the value determined with Fischer's triple integral is 7% smaller. In the case of groin fields, the value determined with Fischer's triple integral is 32% larger than the LPTM result. This can be explained by the fact that the triple integral has been evaluated with a constant diffusivity in transverse direction, whereas the LPTM simulation was performed with varying diffusivity. The LPTM simulation where the diffusivity is also a constant, the $D_L/(u_*h)$ value increases to 31,400, which is still 12% smaller than the result of the triple integral. However, this comparison shows that the increase of the dispersion coefficient of more than two orders of magnitude, due to exchange processes with groin fields, is reasonable.

The equilibrium between longitudinal stretching and transverse diffusion is achieved after approximately 400 times the channel width (figure 6.13), which means that the advective zone has the same length compared to the case of pure channel flow. Therefore, it can be stated that the residence time T_D appears not to be the determining time scale for this equilibrium to reach. Compared to the time needed for a particle to cross the entire river cross section due to turbulent diffusion, the mean residence time T_D is very small for the given situation. In the present problem the transverse mixing time can be approximated by $B^2/(2D_y)$, which is of the order of 3000 s compared to 90 s of T_D . The final value of the skewness of about -0.1 is achieved after approximately 1500 times the channel width.

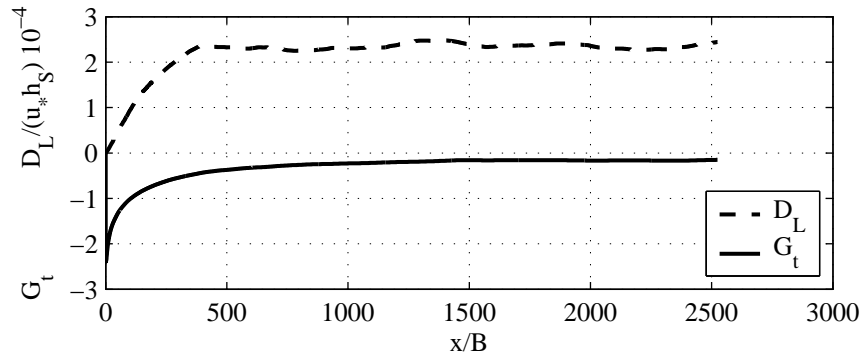


Figure 6.13. Evolution of Dispersion coefficient $D_L 10^{-4}$ normalized with u_* and the water depth h and the evolution of the skewness. D_L is smoothed with a sliding average filter of increasing window size. ($W/B = 0.5$)

In the verification cases of section 6.3 and in the case of pure channel flow, the transport velocity c , which is defined as the translation velocity of the center of mass of the tracer cloud, is always equal to the mean flow velocity in the channel, as long as the particle distribution is homogeneous over the river cross-section. In case of the groin field flow the transport velocity decreases during the travel of the tracer cloud until an equilibrium between the particles in the dead-water zones and in the main channel is established as seen in figure 6.14. In this simulation the transport velocity does not change further, after the tracer cloud has travelled approximately 400 times the channel width, which

corresponds to the length of the advective zone. The final transport velocity is 64% of the mean flow velocity in the main channel.

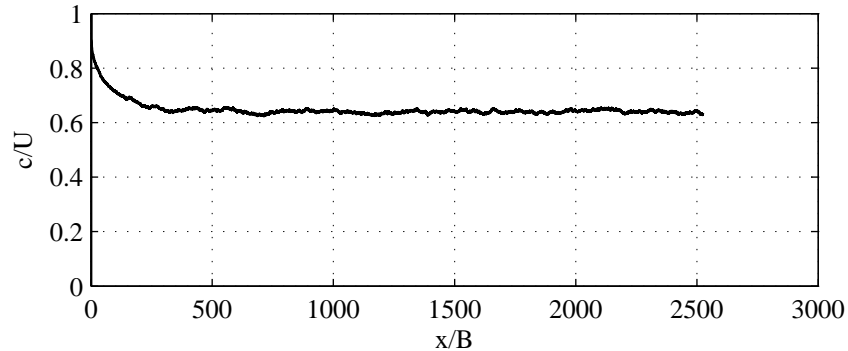


Figure 6.14. Evolution of transport velocity c of a tracer cloud normalized with mean velocity of the main channel.

In the case of pure channel flow the particle distribution in transverse direction of the river cross-section is initially and at the end of the simulation homogeneous (figure 6.15, i) and does not shift to any direction. This behavior changes under the influence of groin fields (figure 6.15, ii, iii, iv). The particle distribution during the LPTM simulation shifts towards the dead-water zones. In the final stage of mixing (figure 6.15, iv) almost 40% of the tracer material is distributed in the region of the dead-water zones. The remaining 60% of the material is travelling in the main stream.

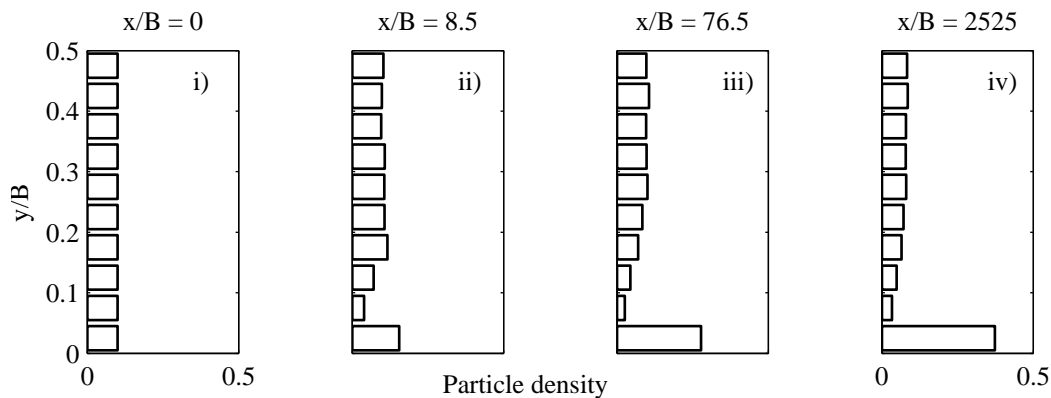


Figure 6.15. Particle density distribution in river cross-section as a function of the distance x/B .

6.4.3 Influence of groin fields of different exchange behavior

The dimensionless exchange coefficient k (equation 6.18), can be found in the literature to be of the order 0.02 ± 0.01 (Valentine & Wood 1979, Uijttewaal et al. 2001), with no clear dependency on the shape of the dead-water zone. With our laboratory experiments, it could be shown that k varies with the hydraulic radius R_D of the groin fields within

the range of 0.015 – 0.035. Hereby, the largest value of the hydraulic radius leads to the highest exchange coefficient and the smallest R_D correspond to the lowest (section 5.33). In the case of experiments No. 1-8 the groin field width W was constant. According to equation 3.70 the transport velocity should always be the same in that case. In order to demonstrate the influence of the changing k -values three more LPTM simulations have been performed, where k has been set to 0.015, 0.020, 0.030 and 0.035 respectively.

Table 6.5. Results of LPTM simulations with different exchange coefficients corresponding to varying R_D/h from figure 5.33 corresponding to a channel width $B/h = 43$, compared with the case of pure channel flow ($k = \infty$).

k	∞	0.035	0.030	0.020	0.015
R_D/h	pure channel flow	≈ 8.1	≈ 7.0	≈ 4.4	≈ 2.7
$D_L/(u_* h_S)$	177	21540	24370	33850	39050
c/U	1	0.68	0.64	0.55	0.48

In table 6.5 the results of the simulations with variable exchange coefficients are summarized. It can be seen that the dimensionless dispersion coefficient $D_L/(u_* h)$ is directly proportional to the residence time T_D . The longer the residence time, the higher the stretching rate of the tracer cloud.

In figure 6.16 the relation between the transport velocity and the mean residence time that corresponds to the normalized hydraulic radius R_D/h_S is plotted. The transport velocity increases linearly with increasing hydraulic radius.

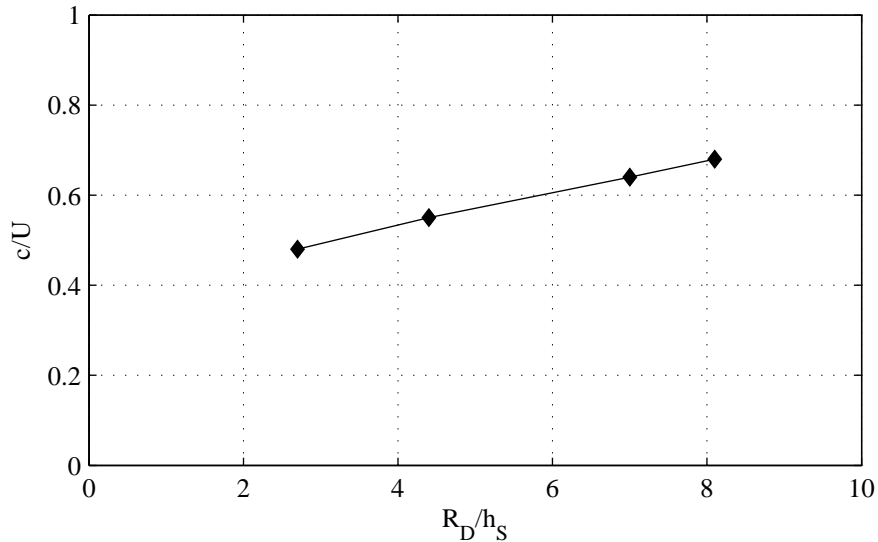


Figure 6.16. Normalized transport velocity c/U as a function of the shape factor R_D/h_S .

An equilibrium between longitudinal stretching and transverse diffusion is reached in all cases after approximately 400 times the channel width B . That indicates that the dominant time scale is not T_a , but the transverse mixing time $B^2/(2D_y)$ that describes

the time needed for a particle to cross B . If we determine the length x/B , with the help of the mean transport velocity c and the transverse mixing time, we get

$$\frac{x}{B} = \frac{cB}{2D_y} = 1550 \quad (6.19)$$

which means that the length of the advective zone $L_x = \alpha B^2 U / (D_y)$ fits to the observation with $\alpha = 0.25$.

6.4.4 Combined effect of dead-water zones and channel width

Up to now the analysis was focused on the effect of the dead-water zones on the longitudinal dispersion. In section 3.3.2 it has been shown that in rivers longitudinal dispersion is directly related to the river width B . In the approximation of Fischer et al. (1979) given in equation 3.58 the longitudinal dispersion coefficient D_L is proportional to B^2 . Thus, in order to predict the stretching rate of a tracer cloud in a real river system B has to be included into the prediction. A dimensionless parameter that combines the driving mechanisms of longitudinal dispersion in the main channel, can be derived by the combination of the channel width B , the transverse diffusivity D_y and the main stream velocity U leading to BU/D_y .

In figure 6.17 the influence of the channel width BU/D_y is visualized with the help of additional simulations where the channel width B has been changed. The data points with $BU/D_y = 4583$ represent the results presented in the previous section in table 6.5 for LPTM simulations with changing exchange coefficients, corresponding to different values of the normalized hydraulic radius R_D/h_S . Again, larger hydraulic radius corresponds to higher exchange value k , which means that the mean residence time T_D is smaller and therefore the longitudinal dispersion coefficient decreases. The data points in figure 6.17 for $BU/D_y = 9166$ represent four LPTM simulations with the same input parameter as the simulations presented in section 6.4.3 except the width of the channel that has been doubled. The lowest line in figure 6.17 represent the results of LPTM simulations where the channel width is only half of the original value.

Figure 6.17 shows that the influence of BU/D_y is not a constant. This can be explained by the amount of tracer mass in the main channel compared the amount of mass in the dead-zones, which is affected by the mean residence time T_D and the ratio of the cross sectional area of the main channel and the dead-zone.

In table 6.6 the flow situation of a real river is summarized, which represent the data point 'Natural condition' in figure 6.17.

Table 6.6. Flow situation, similar to the flow in the river Rhine close to Karlsruhe at km 390 with groins only on one side of the river, representing the the data point 'Natural conditions' in figure 6.17.

B	U	h	Channel slope	u_*	W	L	R_D/h_S	BU/D_y
180 m	2 m/s	3 m	0.02 %	0.077 m/s	40 m	60 m	8	2600

According to figure 6.17 this flow situation leads to a normalized longitudinal dispersion of about 15.000. In the work of van Mazijk (1996) the results of tracer experiments

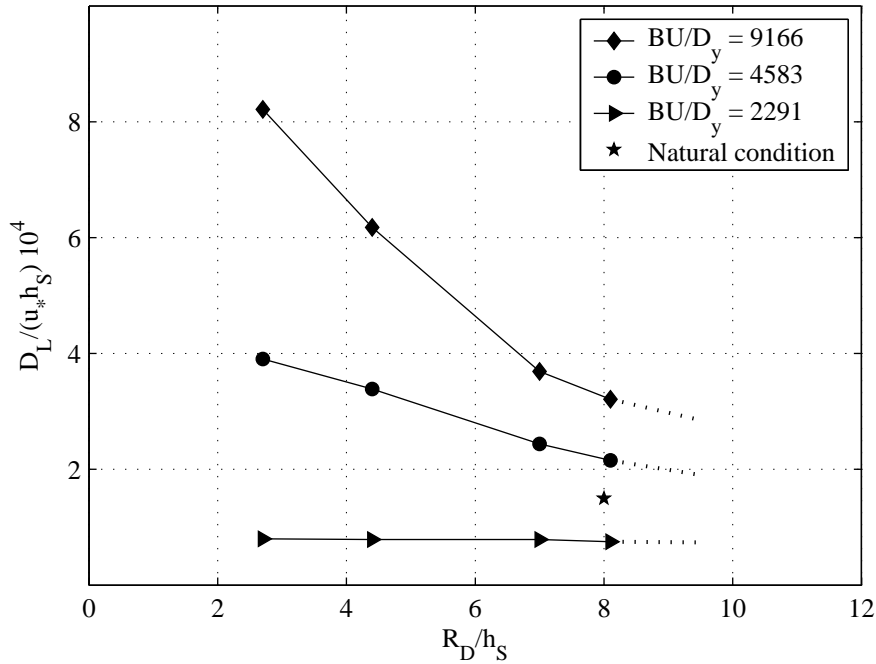


Figure 6.17. Influence on channel width on the longitudinal Dispersion coefficient, in comparison with a real river situation.

are presented that have been performed in the river Rhine. At km 400 the normalized longitudinal dispersion coefficient has been determined to be of order 7.200, which is by a factor of two smaller than the predicted value. One reason for this difference is the difference in the coefficient of transverse diffusion that has been determined with $D_y = 0.15u_*h$, which is usually much larger in real rivers. Stronger transverse mixing leads to a stronger homogenization in transverse direction and, therefore, to less dispersion in longitudinal direction. In the present case the simulations have been performed with the values taken from the laboratory experiment. A difference to a real river situation is also the chosen transverse velocity profile, which could be adapted to a more realistic velocity profile.

Another uncertainty are the tracer experiments themselves. In many cases the tailing of such tracer clouds is insufficiently represented within the measurements. As has been shown in figure 6.15 a large amount of tracer sits in the dead-zones and is therefore, travelling close to the groin heads or close to the banks. Especially, in periods where the tracer cloud is not fully mixed, which is the case in large sections of these tracer experiments, the difference between the tracer travelling in the mid section of the channel compared to mass close to the banks can be large. Therefore, measurements taken from a bridge in the center of the channel can lead to very limited results.

6.5 Summary

In this chapter it could be shown that Lagrangian-Particle-Tracking is applicable for simulating longitudinal dispersion under the influence of transverse velocity shear and

turbulent diffusion. Comparisons with analytical solutions (section 6.3) lead to the same results, if the influence of the noise-drift component (equation 6.5) is included in the case of changing transverse diffusion. The influence of groin fields has been parameterized with the mean residence time that has been included into the boundary conditions as a transient adhesion boundary (figure 6.3). LPTM simulations have been performed to transfer the results obtained with the experimental results at single dead-water zone into the 1-dimensional transport parameters of a system with many dead-water zones.

In section 6.4.3 it could be shown, that groin fields can increase the stretching rate of a tracer cloud strongly. In the case of pure channel flow the longitudinal dispersion coefficient is about two orders of magnitude smaller than in the case with groins for the given conditions.

The transport velocity in the far-field of a transport process, according to the 1-dimensional dead-zone-model (Valentine & Wood 1979, van Mazijk 2002), can be determined with the ratio between the cross-sectional area of the dead-water zone A_D and the cross-sectional area of the main stream A_S assuming a fully mixed situation, as it has been described in section 3.4.1. In the present simulations from table 6.5 this relation would lead to a value of 67% of the mean flow velocity, which is close to the result of the LPTM simulation for the case where k is set to 0.035. According to these simulations, the results of the 1-dimensional dead-zone-model mentioned above predicts the transport velocity correctly, for an exchange value k of about 0.035. This value corresponds to groin fields where the normalized hydraulic radius of the groin fields is about 8.1 which corresponds to the experiment No. 1 from table 4.2 with an aspect ratio of $W/L = 0.33$. The influence of the different k -values on the transport velocities for this configuration is at maximum $\pm 15\%$.

The skewness of the particle cloud in longitudinal direction tends to zero and reaches a final value of approximately -0.1 in flow situations with and without groins. The final value is reached after a travel distance of about 1500 times the channel width. The same result holds for the cases with varying exchange coefficients. Herewith it can be stated, that the mass exchange does only influence the stretching rate and the transport velocity of the particle cloud, but not the skewness.

In section 6.4.4 it has been shown that the dimensionless parameter BU/D_y has to be included into the simulations, in order to take into account the stretching mechanisms in the main stream. A comparison with field data showed that an agreement of the obtained dispersion coefficients could be found within a factor of two.

7. Conclusions and Recommendations

The goal of this study was the improvement of the predictive abilities of existing 1-dimensional alarm models for accidental pollutant spills. Currently, extensive tracer experiments are needed to calibrate the existing models, because of the influence of morphologic heterogeneities in rivers on the transport characteristics, which is not fully understood. In the present study, laboratory and numerical experiments have been performed to determine the influence of dead-water zones, especially groin fields, on the transport characteristics in rivers.

First a literature review of detailed map information material has been performed which showed that in most cases the groin fields in nature belong to Class 1 and 6 (section 2.2), which means that even under the influence of sedimentation processes the groin field area is approximately a rectangle with a varying aspect ratio (width/length) ranging from 0.15 - 0.7. In most cases, the groins are built perpendicular to the channel wall as for example in the river Waal. The first groins that were built in the river Elbe are forward inclined. Such an inclination angle has a negative impact on the bank protection. Therefore, groins, which are not perpendicular to the flow are inclined backward. Based on this knowledge, experiments in the laboratory have been performed with different aspect ratios varying from 0.17 to 3.5. Additional experiments were carried out to determine the influence of varying inclination angle, varying water depth in the groin field and reduced width of the groin field.

A surface Particle-Image-Velocimetry (PIV) system has been developed (section 4.2.1) to measure mean and turbulent characteristics of the flow in large areas with high spatial and time resolution at the water surface. The shallowness of the flow and the corresponding 2-dimensional behavior of the flow allows to use this surface information to characterize the depth-averaged flow field. An important part of the surface PIV system is the particle seeding on the water surface. To provide a homogeneous particle distribution a particle dispenser has been developed that makes it possible to regulate the particle density for different flow velocities (section 4.2.2). It could be shown that black Polypropylene particles with additional matt black lacquer finish give the best results with respect to the problem of clustering. The surface PIV system works well in flow regions where the corresponding length and time scales fit the size of the used seeding particles and time resolution. For the purpose of comparison Laser-Doppler-Velocimetry (LDV) measurements were performed, which showed that the turbulent characteristics (rms-velocities) in the mixing layer, where the flow is dominated by large coherent structures, is very well represented with the surface PIV. In the region of undisturbed channel flow, the rms-velocities are underestimated in the current setup because of resolution problems.

The velocity measurements showed the typical one- and two-gyre systems in the dead-water zone in dependency on the aspect ratio. The mean velocity distribution in the main channel differs slightly from the case of pure channel flow, such that the velocity distribution is much smoother. The distance between two groins has almost no influence on this velocity distribution. Flow visualizations and the evaluation of vorticity fields (section 5.1.1) showed that the flow in the mixing layer is dominated by large coherent motions that are responsible for the mass transfer between the main channel and the mixing layer. As a further result from the PIV measurements the mass exchange coefficient has been determined by evaluating the transverse component of the instantaneous flow velocities at the interface between main channel and dead-zone.

The mass transfer has been also measured with a second approach called Planar-Concentration-Analysis (PCA). With the help of Multi-Port-Injection-Device (section 4.3.1) a homogeneous concentration field is produced instantaneously in one groin field, which is then observed from above with a digital camera. It could be shown that the calibration procedure can be optimized, by using a reverse dependency between brightness and concentration (section 4.3.2). The resulting first order decay leads finally to a mean residence time that can be normalized to the dimensionless exchange coefficient. It was found, that the coefficients agreed well with the ones obtained from the surface PIV measurements.

The exchange coefficients obtained from both, PIV and PCA measurements showed that this value is not a constant, but depends on the groin field geometry. In the case of groin fields with constant width, the exchange coefficient is decreasing with increasing aspect ratio W/L . Experiments with short groins showed that the volume of the groin field is also playing a role in the mass exchange process. By scaling the mass exchange coefficient with the normalized hydraulic radius of the groin field, the data coincide to a single trend. Furthermore, the inclination angle of the groins has a certain influence on the mass exchange. Groins inclined against the flow enhance the mass exchange, whereas groins inclined with the flow damps the mass exchange.

A Lagrangian-Particle-Tracking-Method (LPTM) has been developed to transfer the experimental results obtained at a single dead-water zone into transport characteristics in the far-field. Hereby, the influence of dead-water zones has been parameterized with a Transient-Adhesion-Boundary-Condition (section 6.2) based on the mean residence time of tracer mass in the dead-water zone. In the present case, the LPTM simulations showed that in the case of a flow where the cross-sectional area of the dead-zone is half the main channel cross-section the longitudinal dispersion is increased by two orders of magnitude compared to pure channel flow. The skewness of the particle distribution is almost not affected by the introduction of the dead-zones. The varying residence times that correspond to different exchange coefficients can have a strong influence on the resulting dispersion coefficient up to $\pm 25\%$. The influence of the different exchange coefficients on the transport velocities is at maximum $\pm 15\%$ for the present configuration (table 6.5) for a fixed value of BU/D_y . A comparison with field data showed that an agreement of the obtained dispersion coefficients could be found within a factor of two. Further improvement of the LPTM simulations could be obtained by adapting the transverse diffusivity and the horizontal velocity distribution to more natural conditions.

Future work should aim at adopting the present measurement and simulation techniques to varying morphologic conditions, like changing channel width and depth as well as changing groin field conditions. With these implementations it should be possible to use the presented method for the prediction of pollutant spills in natural cases. A further task would be to implement these program elements into an expert system that allows simple and fast development of 1-dimensional alarm models for different river systems.

References

- Abbott, M. B. & Basco, D. R. (1989), *Computational Fluid Dynamics*, Harlow, Longman.
- Adrian, J. R., Meinhart, C. D. & Tomkins, C. D. (2000), 'Vortex organization in the outer region of the turbulent boundary layer', *Journal of Fluid Mechanics* **422**, 1–54.
- Adrian, R. J. (1991), 'Particle-imaging techniques for experimental fluid mechanics', *Annual review of Fluid Mechanics* **23**, 261–304.
- Altai, W. & Chu, V. H. (1997), Retention time in recirculating flow, in '27th IAHR Congress', IAHR, Delft, Holland.
- Aris, R. (1959), 'The longitudinal diffusion coefficient in flow through a tube with stagnant pockets', *Chemical Engineering Science* **11**, 194–198.
- Booij, R. (1989), Exchange of mass in harbors, in '23rd IAHR Congress', IAHR, Ottawa, pp. 69–74.
- Chatwin, P. C. (1980), 'Presentation of longitudinal dispersion', *Proc. ASCE, J. Hydraulics Division* **106**(HY1), 71–83.
- Chen, F. Y. & Ikeda, S. (1997), 'Horizontal separation flows in shallow open channels with spur dikes', *Journal of Hydroscience and Hydraulic Engineering* **15**(2), 15–30.
- Deng, Z. Q., Bengtsson, L., Singh, V. P. & Adrian, D. D. (2002), 'Longitudinal dispersion coefficient in single-channel streams', *Journal of Hydraulic Engineering* **128**(10), 901–916.
- Deng, Z. Q., Singh, V. P. & Bengtsson, L. (2001), 'Longitudinal dispersion coefficient in straight rivers', *Journal of Hydraulic Engineering* **127**(11), 919–927.
- Denton, R. A. (1990), 'Analytical asymptotic solutions for longitudinal dispersion with dead zones', *Journal of Hydraulic Research* **28**, 309–329.
- Dunsbergen, D. W. (1994), Particle Models for Transport in Three-Dimensional Shallow Water Flow, PhD thesis, TU-DELFT, Faculty of Civil Engineering.
- Durst, F., Melling, A. & Whitelaw, J. H. (1981), *Principles and practice of Laser-Doppler anemometry*, Academic Press, New York, USA.
- Elder, J. W. (1959), 'The dispersion of marked fluid in turbulent shear flow', *Journal of Fluid Mechanics* **5**, 544–560.
- Fischer, H. B. (1966), Longitudinal dispersion in laboratory and natural streams, Technical Report KH-R-18, California Institute of Technology, Pasadena, California.
- Fischer, H. B. (1967), 'The mechanics of dispersion in natural streams', *J. Hydraul. Div. Proc. Am. Soc. Civ. Eng.* **93**, 187–216.
- Fischer, H. B., List, E. G., Koh, R. C. Y., Imberger, J. & Brooks, N. H. (1979), *Mixing in Inland and Coastal Waters*, Academic Press, New York, NY.
- Gardiner, C. W. (1985), *Handbook of Stochastic Methods*, Springer-Verlag.
- Giger, M., Jirka, G. H. & Dracos, T. (1991), 'Entrainment and mixing in plane turbulent jets in shallow water', *Journal of Hydraulic Research* **29**(5), 615–642.
- Grant, I. (1997), 'Particle image velocimetry: A review', *Journal of mechanical engineering science* **211**(C), 55–76.
- Guhr, H. (2002), Stoffdynamik in Bühnenfeldern der Elbe - Erste Ergebnisse, in A. van Mazijk & V. Weitbrecht, eds, 'New Insights in the physical and ecological processes in groyne fields (in german)', TU-Delft, Holland.
- Gui, L. C. & Merzkirch, W. (1996), 'A method of tracking ensembles of particle images', *Exp. Fluids* **21**, 465–065.
- Hannappel, S. & Pierho, B. (1996), 'Cluster analysis of environmental data which is not interval scaled but categorical, evaluation of aerial photographs of groyne fields for the determination of representative sampling sites', *Chemosphere* **33**(2), 335–342.
- Hays, J. R., Krenkel, P. A. & Schnelle, K. B. (1966), Mass transport mechanisms in open-channel flow, Technical Report 8, Vanderbilt University, Nashville Tennessee.
- Hentschel, B. & Anlauf, A. (2002), Ökologische Optimierung von Bühnen in der Elbe, in A. van Mazijk & V. Weitbrecht, eds, 'New insights in the physical and ecological processes in groyne fields', TU-Delft, Holland.
- Hinkel, J. (1999), Die Ermittlung von vegetationsfreier Flächen entlang der Elbeufer aus Luftbildern und ihre Korrelation mit der Flussgeometrie und dem Uferverbau, Master's thesis, University of Karlsruhe, Karlsruhe.
- Holley, E. R. & Jirka, G. (1986), Mixing in rivers, Technical report, US Army Engineer Waterways Experiment Station, Vicksburg, Miss.

- Hunter, J., Craig, P. & Phillips, H. (1993), 'On the use of random walk models with spatially variable diffusivity', *Computational Physics* **106**, 366–376.
- Kühn, G. (2000), 'PIV und PTV im Strömungslabor: Erfassung von Oberflächengeschwindigkeiten mit Ganzfeldmessverfahren', Diploma thesis at the Institute for Hydromechanics, University of Karlsruhe.
- Kimura, I. & Hosoda, T. (1997), 'Fundamental properties of flows in open channels with dead zone', *Journal of Hydraulic Engineering* **123**(2), 322–347.
- Kinzelbach, W., Zimmermann, S. & Koumoutsakos, P. (2001), 'Simulation of pollutant transport using a particle method', *Journal of Computational Physics* **173**, 322–347.
- Kurzke, M., Weitbrecht, V. & Jirka, G. H. (2002), Laboratory concentration measurements for determination of mass exchange between groin fields and main stream, in 'River Flow 2002', IAHR, Louvain la Neuve, Belgium.
- Lange, G. & Lecher, K. (1989), *Gewässerregulierung Gewässerpflege, Naturnaher Ausbau und Unterhaltung von Fließgewässern*, second edn, Paul Parey, Hamburg.
- Lehmann, D. (1999), 'Auswirkung von Bühnenfeldern auf den Transport gelöster Stoffe in Flüssen', Diploma thesis at the Institute for Hydromechanics, University of Karlsruhe and TU-Delft, Hydromechanics Section.
- Linden, P. F., Boubnov, B. M. & Dalziel, S. B. (1995), 'Source-sink turbulence in a rotating stratified fluid', *Journal of Fluid Mechanics* **298**, 81–112.
- Nübel, K. & Weitbrecht, V. (2002), 'Visualization of localization in grain skeletons with particle image velocimetry', *Journal of Testing and Evaluation* **30**(4), 322–328.
- Neger, R. (1932), *Die Entwicklung des Bühnenbaues in den deutschen Stromgebieten*, Wilhelm Ernst und Sohn, Berlin.
- Nezu, I. & Nakagawa, H. (1993), *Turbulence in Open-Channel Flows*, Balkema, Rotterdam.
- Nordin, C. F. & Sabol, B. V. (1974), 'Empirical data on longitudinal dispersion in rivers', *U.S. Geological Survey of Water Resources Investigations 20-74* pp. 372–374.
- Nordin, C. F. & Troutman, B. M. (1980), 'Longitudinal dispersion in rivers: The persistence of skewness in observed data', *Water Resources Research* **16**(1), 123–128.
- Petersen, M. S. (1986), *River Engineering*, Prentice-Hall, Englewood Cliffs, New Jersey.
- Raffel, M., Willert, C. & Kompenhans, J. (1998), *Particle Image Velocimetry*, Springer Verlag, Berlin.
- Rehbock, T. (1926), *Das Flussbaulaboratorium der Technischen Hochschule in Karlsruhe*, VDI-Verlag, Berlin, Germany.
- Riepe, E. (1930), Versuche über die Wirkung inklinanter Bühnen in einer konkaven Flusskrümmung, PhD thesis, Technische Hochschule Braunschweig, Braunschweig.
- Ruck, B. (1987), *Laser-Doppler-Anemometrie*, AT-Verlag, Stuttgart, Germany.
- Rummel, A. C., von Carmer, C. F. & Jirka, G. H. (2002), 'Combined planar measurements of flow velocity and mass concentration in shallow turbulent flow. part i: Development of a planar concentration analysis (pca) system', *Proc. Int. Conf. on Hydr. Meas. and Exp. Meth.*
- Rutherford, J. C. (1994), *River Mixing*, Wiley, Sussex, England.
- Scarano, F. & Riethmüller, M. L. (1999), 'Iterative multigrid approach in piv image processing with discrete window offset', *Experiments in Fluids* **26**, 513–523.
- Schlichting, H. (1979), *Boundary-Layer Theory*, McGraw Hill, New York.
- Schmid, B. H. (1995), 'On the transient storage equations for longitudinal solute transport in open channels: temporal moments accounting for the effects of first-order decay', *Journal of Hydraulic Research* **33**(5), 595–610.
- Seo, W. & Cheong, T. S. (1998), 'Predicting longitudinal dispersion coefficient in natural streams', *Journal of Hydraulic Engineering* **124**(1), 25–32.
- Seo, W. & Cheong, T. S. (2001), 'Moment-based calculation of parameters for the storage zone model for river dispersion', *Journal of Hydraulic Engineering* **127**(6), 453–465.
- Sheridan, J., Lin, J. C. & Rockwell, D. (1997), 'Flow past a cylinder close to a free surface', *Journal of Fluid Mechanics* **330**, 1–30.
- Socolofsky, S. A. & Jirka, G. H. (2002), 'Environmental fluid mechanics, 1st edition', Lecture Notes, Institute for Hydromechanics, University of Karlsruhe.
- Spreafico, M. & van Mazijk, A. (1993), Alarmmodell Rhein. Ein Modell für die operationelle Vorhersage des Transportes von Schadstoffen im Rhein, Technical Report I-12, Internationale Kommission zur Hydrologie des Rheingebiets, Lelystad.
- Sukhodolov, A. N. (1998), 'On longitudinal dispersion in river flows', *Water Resources* **25**(2), 186–192.
- Sukhodolov, A. N., Uijtewaal, W. S. J. & Engelhardt, C. (2002), 'On the correspondence between morphological and hydrodynamical patterns of groyne fields', *Earth Surface Processes and Landforms* **27**, 289–305.
- Sullivan, P. J. (1971), 'Longitudinal dispersion within a two-dimensional turbulent shear flow', *Journal of Fluid Mechanics* **49**, 551–576.
- Tarbouriech, L., Didelle, H. & Renouard, D. (1997), 'Time-series PIV measurements in a very large rotating tank', *Experiments in Fluids* **23**, 438–440.
- Taylor, G. I. (1921), 'Diffusion by continuous movements', *Proc. London Math. Soc.* **20**, 196–211.

- Taylor, G. I. (1953), 'Dispersion of soluble matter in solvent flowing slowly through a tube', *Proc. R. Soc. London Ser. A* **219**, 486–233.
- Taylor, G. I. (1954), 'The dispersion of matter in turbulent flow through a pipe', *Proc. R. Soc. London Ser. A* **223**, 446–468.
- Thackston, E. L. & Schnelle, K. B. (1970), 'Predicting effects of dead zones on stream mixing', *Proceedings of the American Society of Civil Engineers, Sanitary Engineering Division* **96**(SA 2), 319–331.
- TSI (1996), *Instruction Manual. Model 9800 Series Fiberoptic probes*, St. Paul.
- Uijttewaal, W. S. J. (1999), Groyne field velocity patterns determined with particle tracking velocimetry, in '28th IAHR Congress', Graz, Austria.
- Uijttewaal, W. S. J. & Jirka, G. H. (2003), 'Grid turbulence in shallow flows', *Journal of Fluid Mechanics* **489**, 325–344.
- Uijttewaal, W. S. J., Lehmann, D. & van Mazijk, A. (2001), 'Exchange processes between a river and its groyne fields: Model experiments', *Journal of Hydraulic Engineering* **127**(11), 928–936.
- Valentine, E. M. & Wood, I. R. (1979), 'Experiments in longitudinal dispersion with dead zones', *Journal of the Hydraulics Division* **105**(HY8), 999–1016.
- van Kampen, G. W. (1981), 'Itô versus stratanovich', *Journal of Statistical Physics* **24**(1), 175–187.
- van Mazijk, A. (1996), One-dimensional approach of transport phenomena of dissolved matter in rivers, PhD thesis, TU-DELFT, Faculty of Civil Engineering.
- van Mazijk, A. (2002), 'Modelling the effects of groyne fields on the transport of dissolved matter within the rhine alarm-model', *Journal of Hydrology* **264**, 213–229.
- von Carmer, C. F. (2000), LDA-LIF System zur Untersuchung großräumiger kohärenter Strukturen in flacher turbulenter Strömung, in A. e. Delgado, ed., 'Lasermethoden in der Strömungsmesstechnik, 8. GALA-Fachtagung', Shaker Verlag, Aachen, pp. 18.1–18.9.
- von Carmer, C. F., Koch, T. & Jirka, G. H. (2000), Großräumige wirbelstrukturen in turbulenter flachwasserströmung, Technical Report 766, Institut für Hydromechanik, Universität Karlsruhe.
- von Carmer, C. F., Rummel, A. C. & Jirka, G. H. (2003), 'Influence of secondary motion in large-scale coherent structures on the mass transport in a shallow turbulent wake', *Proc. Int. Symp. Shallow Flows, Delft, NL*.
- von Carmer, C. F., Weitbrecht, V. & Jirka, G. H. (2001), 'On the genesis and fate of large coherent vortical structures in turbulent shallow wake flows', *Proc. 3rd Int. Symp. Env. Hydr. Tempe, USA*.
- Weitbrecht, V., Kühn, G. & Jirka, G. H. (2002), 'Large scale piv-measurements at the surface of shallow water flows', *Flow Measurements and Instrumentation* **13**, 237–245.
- Westerweel, J. (2000), 'Theoretical analysis of the measurement precision in particle image velocimetry', *Experiments in Fluids* **29**(7), 3–12.
- Westrich, B. (1978), Massenaustausch in Strömungen mit Totwasserzonen unter stationären Fließbedingungen, Technical Report SFB 80/ET80, Institut für Hydromechanik, Universität Karlsruhe.
- Willert, C. E. & Gharib, M. (1997), 'The interaction of spatially modulated vortex pairs with free surfaces', *Journal of Fluid Mechanics* **345**, 227–250.